SOFT X-RAYS FROM THE CYGNUS LOOP

Thesis by

John Charles Stevens

In Partial Fulfillment of the Requirements

for the Degree of

Doctor of Philosophy

California Institute of Technology

Pasadena, California

1973

(Submitted September 12, 1972)

ACKNOWLEDGMENT

Several people assisted in the construction of this experiment. Belal Baaquie, Paul Gloger and Craig Sarazin helped with the collimator assembly and with the stretching of the polypropylene windows. Fred Yates was responsible for the electronics involved in this experiment except for the detector electronics which were designed by Bill Blodgett. Steve Speer was responsible for the detector gas regulation and supply system. He also located the fiducial lights in the aspect camera and later developed the flight film. This experiment was a modification of the payload used in a previous experiment. Dr. Guenter Riegler in collaboration with Dr. Gordon Garmire was responsible for that prior experiment.

The calibration of the collimators used in this experiment required many man-hours, some of which occurred when more rational folk are long asleep. Bill Moore and Craig Sarazin deserve my thanks for support during that hectic period.

The reduction of the data at times proved to be difficult and exasperating. Paul Gloger provided many valuable programs written with inspiration and ingenuity. He is to be especially commended for his encoding of the Cygnus Loop inversion-mapping problem.

The Attitude Control System which oriented the rocket payload during the actual experiment was programmed by Ball Brothers Research Corp. in conjunction with the Sounding Rocket Division of Goddard Space Flight Center. The rocket vehicle was provided, prepared and launched by the Navy personnel of the White Sands Missle Range.

My thanks also go to my advisor, Dr. Gordon Garmire, for allowing me the sole responsibility for this experiment. With a few valuable exceptions, he allowed me to make the decisions, the mistakes and the corrections which made this experiment a unique learning experience. He was also a wellspring of suggestions and critical ideas during the spectral analysis of the Cygnus Loop data.

My financial support has been from the National Science Foundation and from Research Assistantships from the California Institute of Technology. Without this support I could not have been a graduate student. The experimental work was supported by NASA contracts NGL-05002-007, NGL-05002-207, and NGR-05002-219.

ABSTRACT

A detailed soft x-ray survey of the Cygnus Loop, obtained from a rocket-borne experiment, provides evidence that the x-ray emission from this supernova remnant is produced by the interaction of a shock wave and the interstellar medium. A spatial map, having 0.5^{o} by 0.5^{o} resolution, of the structure of the Cygnus Loop in 0.2 to 1.5 kev x-rays is presented. The map shows regions of x-ray emission which correlate well with features at radio and optical wavelengths. It also shows regions for which the antithesis holds. A detailed spectral examination of the total emission from the Loop by a proportional counter equipped with a two-element filter system, shows evidence for line emission between 530 and 690 ev. The overall spectrum is found to be well represented by a thermal bremsstrahlung spectrum with line emission. The intensity of x-ray emission between 0.2 and 1.5 kev from the Cygnus Loop is found to be $1.2 \pm 0.3 \times 10^{-8}$ ergs/cm^2-sec at the earth. Assuming a distance of 770 pc to the Loop and a columnar density of interstellar hydrogen of $.48 \pm .02 \times 10^{21}$ atoms/cm^2 the total energy radiated in 0.2 to 1.5 kev x-rays by the Loop is found to be 2.1×10^{36} ergs/sec. An inhomogeneous anisotropic shock wave model of the Cygnus Loop is found to be

required by the data. Such a model is developed and is shown to explain the spatial and spectral appearances of the Cygnus Loop in soft x-rays. The model requires a shock front expansion velocity only as large as that implied by the optical radial velocity measurements.

TABLE OF CONTENTS

I. INTRODUCTION

A. Overview

At optical frequencies the Cygnus Loop is a group of sharp filaments and diffuse wisps having the rough appearance of a broken shell (figure 1). The approximate center of the Loop is $\alpha(1950) = 20^h\ 49\overset{m}{.}5$, $\delta(1950) = 30^\circ\ 48.5'$(Minkowski, 1958). The optical emission has been extensively studied by a number of authors. It consists entirely of line emission (Minkowski,1968). The radio emission has also been investigated, including a survey of the polarization of the Loop at 11 cm by Kundu (1969). The radio spectra are found to be non-thermal. Recently the Cygnus Loop was found to be an intense emitter of soft x-rays (Grader et al, 1970). Further studies by Gorenstein et al (1971) indicated the possible existence of x-ray line emission from the Loop. On October 23, 1971 a rocket-borne experiment examined the soft x-rays from the Loop in some detail. This paper describes that experiment and its results.

B. Optical Observational Data

The sharp filamentary structure and the apparent lack of an exciting star (Oort, 1946) suggests that the Cygnus Loop is not an emission nebula shining through reradiation. Zwicky (1940) was perhaps the first to

Figure 1. The Cygnus Loop in Hα emission, courtesy of the Hale Observatories. The bright filaments to the right in the picture are NGC 6960. Those to the left, slightly above center, are NGC 6992 and NGC 6995.

Figure 1

suggest that the Cygnus Loop was emission resulting from collisions between the ejecta of a supernova and the interstellar material. Studies of the visual line emission from the Loop (Minkowski, 1958 & Parker, 1964) indicate that this emission is consistent with a collisional excitation mechanism. In addition, radial velocity measurements (Minkowski, 1958 & Doroshenko, 1971) have shown that the velocities of both the sharp filaments and of the diffuse wisps are consistent with those expected of a radially expanding shell of matter.

C. Radio Observational Data

A great number of radio observations have been made of the Cygnus Loop. In general these observations show that the radio emission originates in the bright filaments to the northeast (NGC 6992-5) and in a broad maxima in the western half of the Loop including NGC 6960. Kundu's (1969) measurements are typical in their contours of all the radio measurements. Kundu also has mapped the polarization observed at 11 cm wavelength. He sees (figure 2) a region in the southern part of the Loop which is strongly polarized (on the order of 15 to 20%). The rest of the Cygnus Loop although fully as bright as this southern portion displays no polarization down to the 6% sensitivity limit of Kundu's measurements. Van

Figure 2. Contour map and polarization observations of the Cygnus Loop at 11 cm wavelength (Kundu, 1969) superimposed on the Hα picture. The contour unit is 0.108° K in brightness temperature. Bars in the southern portion of the Loop denote polarizations, the length of the bar giving the amount of polarization and the orientation giving the electric vector. The length of bar corresponding to 20% polarization is shown in the lower right corner of the figure.

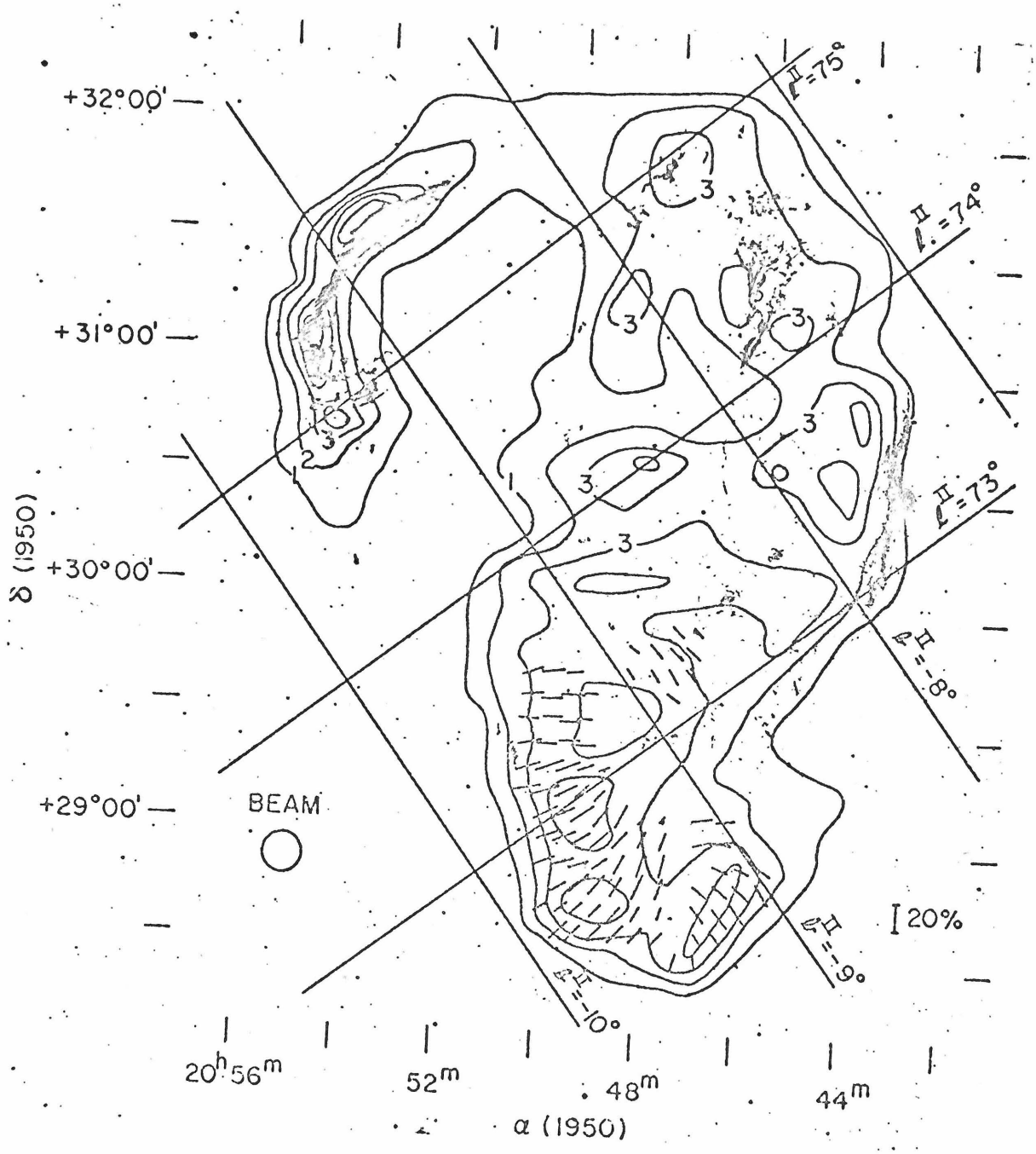
+32°00'
+31°00'
+30°00'
+29°00'
δ (1950)
BEAM
20%
l^{II}=75°
l^{II}=74°
l^{II}=73°
b^{II}=-8°
b^{II}=-9°
b^{II}=-10°
20h56m
52m
48m
44m
α (1950)

Figure 2.

der Laan (1962) proposed that the radio emission from the Loop was synchrotron emission from relativistic charged particles interacting with the interstellar magnetic field compressed by the shock wave from the supernova explosion. Kundu's measurements confirm this for that portion of the Loop showing polarization. In addition calculations based on the observed Hα emission have indicated that only a few percent of the radio emission can be of thermal origin (Parker, 1964). Hence the bulk of the radio emission is probably synchrotron emission. In this case the absence of detectable polarization indicates the existence of a jumbled magnetic field.

D. X-ray Observations

The presence of synchrotron emission at radio wavelengths and the apparently collisionally excited line emission at visual wavelengths leads to two mechanisms which could produce x-ray emission. The synchrotron emission responsible for the radio emission could, if sufficiently energetic electrons were available, lead to x-rays also. Alternately the collisional excitation mechanism producing the visual line emission could also produce x-rays. This latter production process requires that the shock front whose passage through the inter-

stellar medium creates the high temperature plasma necessary to give the optical emission, also produces the much higher temperature plasmas necessary to produce x-rays. That this process is possible will be explicitly shown below in section V.

The first x-ray measurements of the Cygnus Loop were done at moderate energies ($E \gtrsim 2$ kev) and indicated no detectable emission. The most recent measurements by Bleach et al (1972) have confirmed that the Cygnus Loop radiates less than 10^{-2} kev/cm^2-sec at energies above 2 kev. In 1968 Grader and collaborators (Grader et al, 1970) found that the Cygnus Loop is an intense emitter of soft x-rays ($0.2 \geq E \geq 1.5$ kev). Their data was not of sufficient quality to determine whether the spectrum of these x-rays was of thermal or of synchrotron origin. In 1970 Gorenstein and co-workers examined the Cygnus Loop in the soft x-ray range of energies using a one-dimensional focusing telescope system (Gorenstein et al, 1971). They succeeded in obtaining a one-dimensional 'strip' map of the Cygnus Loop. This showed that, in the direction scanned, the x-ray and visual emitting regions were coincident within the accuracy of the data. They also obtained a spectrum of the entire Loop which was best characterized as thermal bremsstrahlung with line emission at 650 ev. The temperature of the plasma giving rise to

the x-rays they found to be 4.2 million degrees. These spectral results are compared with those obtained by this experiment below in section V.

E. The Current Experiment

The line emission at approximately 650 ev could be from a plasma containing collisionally-excited multiply-ionized oxygen atoms. These radiate strongly at temperatures between 2 and 4 million degrees (Shklovskii, 1968 & Tucker et al, 1971) and give rise to several lines clustered around 575 and 650 ev. The presence or absence of these lines furnishes a test of the thermal nature of the emission. Lack of these lines would not necessarily imply that the emission is of non-thermal origin, but their presence would effectively rule out non-thermal origins. The question of whether the line emission reported by Gorenstein et al is in fact present in the Cygnus Loop spectra therefore becomes crucial in deciding between a thermal or a synchrotron origin of these x-rays.

These lines fall in a range of the x-ray spectra where the standard detectors (thin-windowed proportional counters) have poor resolution, typically > 300 ev at 600 ev photon energy. Hence it is difficult to detect the presence or absence of line emission at approximately 600 ev with any assurance using the detector alone. To

overcome this difficulty a filter system employing the absorption discontinuities at the K edges of Oxygen (532 ev) and Fluorine (692 ev) was employed. This system is described in more detail in section II. This filter system was used in the rocket-borne experiment and provided evidence for the presence of oxygen line emission at a level somewhat below that reported by Gorenstein et al. This line emission supports the shock-wave theory of the Cygnus Loop. The experiment is described in greater detail in section II. The observed spectral results are reported in section IV and are discussed with regard to the proposed model in section VI.

To provide more information about the physics involved in the Cygnus Loop a spatial mapping of the soft x-rays from the Cygnus Loop with $0.^{\circ}5 \times 0.^{\circ}5$ resolution was performed in the same rocket-borne experiment that examined the spectra of the Loop's x-rays. The mapping showed that the x-rays come from a region which is largely coincident with the radio and optical regions (figure 3). There are detailed correlations between the x-ray map and similar visual and radio maps and broad regions of dissimilitude. These results are discussed in sections III and VI. Section III gives the spatial structure obtained in this experiment and section VI references these results to a proposed inhomogeneous

Figure 3. Intensity map of x-rays from the Cygnus Loop. Map is of observed x-rays between 0.2 and 1.5 kev. The number of lines in a 0.5^{o} x 0.5^{o} resolution element gives the intensity of x-rays received from that element. Vertical lines are positive intensities, horizontal lines are negative intensities. The observational background has been subtracted from the map. Each line represents 10^{-10} ergs/cm^{2}/sec/resolution element observed at the earth. The error in the measurements is approximately 2×10^{-10} ergs/cm^{2}/sec/resolution element, or $1\sigma \sim \pm 2$ lines. The intensity per line value was obtained by normalizing to the results of the spectral examination described in section IV.

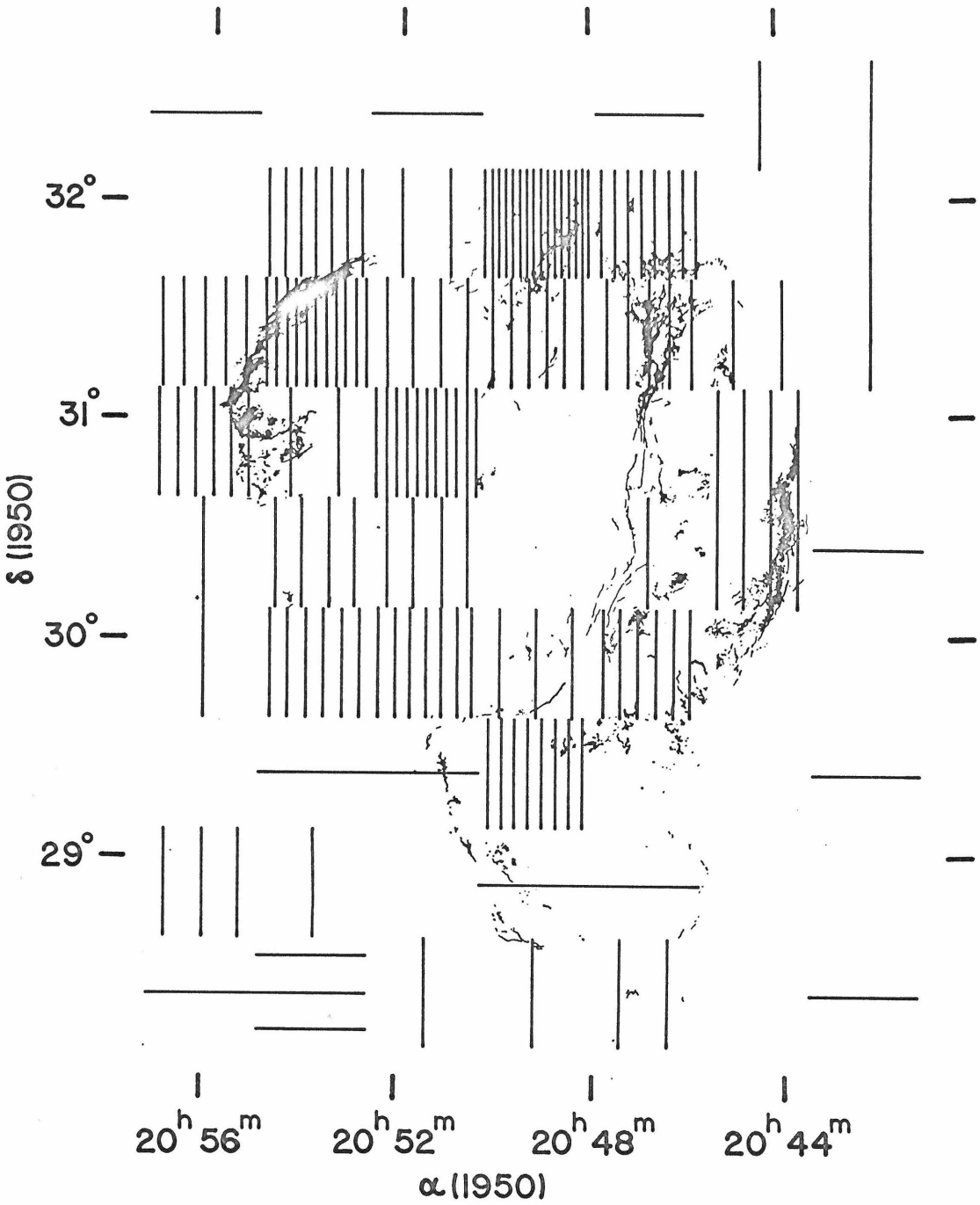

Figure 3

anisotropic shock-wave model of the Cygnus Loop.

This experiment represents an intermediate step between the poor spatial resolution available using collimators of slat-type construction and the high spatial resolution that focusing x-ray detectors will display in the future. It also represents an intermediate step between the poor spectral resolution available from proportional counters alone and the high spectral resolution that will be available using dispersion spectroscopic techniques in the future.

II. DESCRIPTION OF EXPERIMENT

A. Detectors

The experiment consisted of four detectors each of whose field of view was defined by a mechanical collimator. Each detector was a multi-anode thin-windowed gas-filled proportional counter. The salient differences among these detectors are given in Table 1. All four detectors

TABLE 1

DETECTOR CHARACTERISTICS

Detector	Window Thickness	Window Material	Effective Area (cm^2)	Field of View(FWHM)*
A	270 ($\mu gm/cm^2$)	Kimfol	193	0.4 x 9.8
B	270	Kimfol	213	0.4 x 9.8
C	140	Polypropylene	395	12.0 x 12.3
D	271	Polypropylene	425	9.3 x 10.0

*FWHM: Full Width at Half Maximum of collimator response

were filled with methane gas at 150 torr. As noted in Table 1 detectors A and B had fields of view narrow in one direction. The 'fan beams' of these two detectors were used to obtain the spatial mapping of the Cygnus Loop. Detectors C and D had wider fields of view and viewed the entire Loop rather than a portion of it. These two detectors performed the spectral measurements.

Detector D was equipped with two mobile filters and performed the filtered measurements of the Loop.

Each detector had 12 anode wires separated by wire grids. These grids were grounded and arranged in such a fashion as to form planes which divided the detector's volume into 12 proportional counters each having 1/12 of the original volume. These 12 anode wires were wired together in four groups as shown in figure 4 for data processing efficiency. Each group of anode wires was operated in anticoincidence with the other three groups of wires. This aids in rejection of events arising through the interaction of charged particles and γ-rays with the detector. X-rays predominantly deposit their energy in one anode's volume while minimum ionizing particles will deposit energy in all the anode volumes through which they pass.

Other than the anticoincidence the groups of anode wires functioned essentially as independent detectors. Hence each detector volume was composed of four separate proportional counters. Regarding each of these as independent detectors raises the number of detectors from 4 to 16. However the back group of anode wires has the highest noise level and the smallest signal level so that the data from this level was not employed in the spectral or the spatial determination. Also, the three

Figure 4. Schematic cross sectional view of one of the detectors used in this experiment. The figure shows how the anode wires are wired together into four groups for ease of data processing. The front group of wires will be referred to as the "window" group in the text.

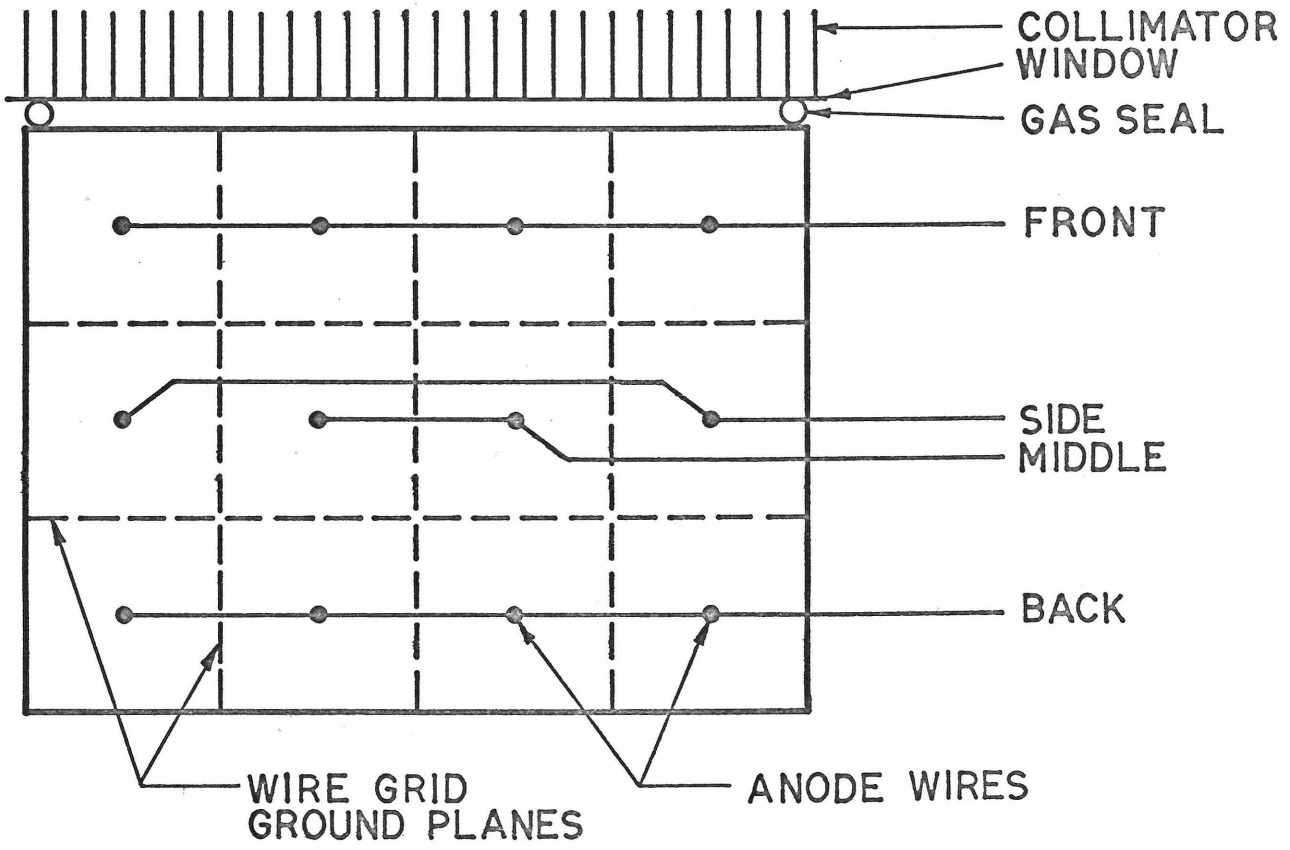
COLLIMATOR
WINDOW
GAS SEAL
FRONT
SIDE
MIDDLE
BACK
WIRE GRID
GROUND PLANES
ANODE WIRES

Figure 4.

remaining groups were combined in the data reduction for detectors A and B since the separation served no purpose in obtaining the spatial structure. Only for detectors C and D was explicit use made of the remaining three groups of anode wires. For these detectors spectra were obtained for each group separately. For identification purposes each group was given a name according to its position in the detector (figure 4). The nomenclature adopted is to refer to, for example, the window group of anode wires of detector C as 'detector C window'.

The linearity of the detectors' energy response was calibrated in the laboratory prior to flight. They were measured at six energies between 0.28 and 2.8 kev. The maximum deviation from a linear response at any of these six energies was less than 2%.

Calibration sources which were visible when the payload door was closed provided an in-flight check of each detector's gain. The calibration sources were Po^{210} alpha sources covered with 0.003 cm aluminum foil. These give a line at the Al Kα transition (1.49 kev). There was 15 sec of useful calibration data before the payload door opened at 80 seconds and another 15 sec after the door closed for reentry at 370 sec. All detectors showed less than 5% gain variation during the flight.

B. Flight Parameters

The experiment was launched on a Nike-Aerobee rocket from White Sands New Mexico on October 23, 1971 at 3:45:00.5 UT. The rocket performed as anticipated and gave approximately 390 seconds of useful flight. The Cygnus Loop was observed for 130 sec during the middle of the flight from 140 sec to 270 sec. There were no major difficulties with the functioning of the detectors. The only difficulties were minor ones; the detectors showed a lower gain than expected so that a larger fraction of the low energy data fell below the discriminator cutoff of the amplifiers, and the oxygen gas cell's bleed rate was slower than expected. The latter difficulty is expounded below in the discussion of the filters.

The altitude during the Cygnus Loop observation varied from 149 km at 140 sec to 181 km at 222 sec and back down to 168 km at 275 sec. The altitude as a function of time from launch for the time period of the Cygnus Loop measurement is shown in figure 5. The atmosphere strongly attenuates the soft x-rays measured in this experiment. To reduce this attenuation to less than 5% at all energies between 0.1 and 1.0 kev it is necessary to get an altitude such that less than 2.1 $\mu gm/cm^2$ of integrated atmosphere remains between the detector and

Figure 5. The altitude of the experiment as a function of time after launch for the time period of the Cygnus Loop measurement.

Figure 6. The atmospheric transmission as a function of energy for three altitudes; curve A - 160 km, curve B - 150 km, curve C - 140 km.

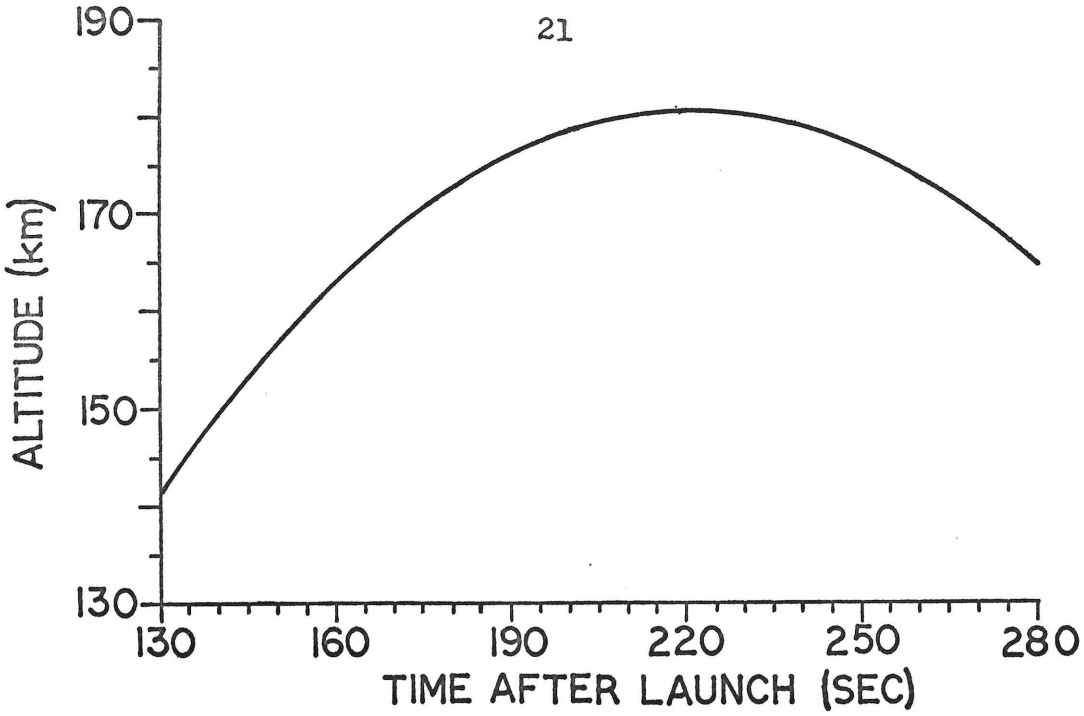

Figure 5.

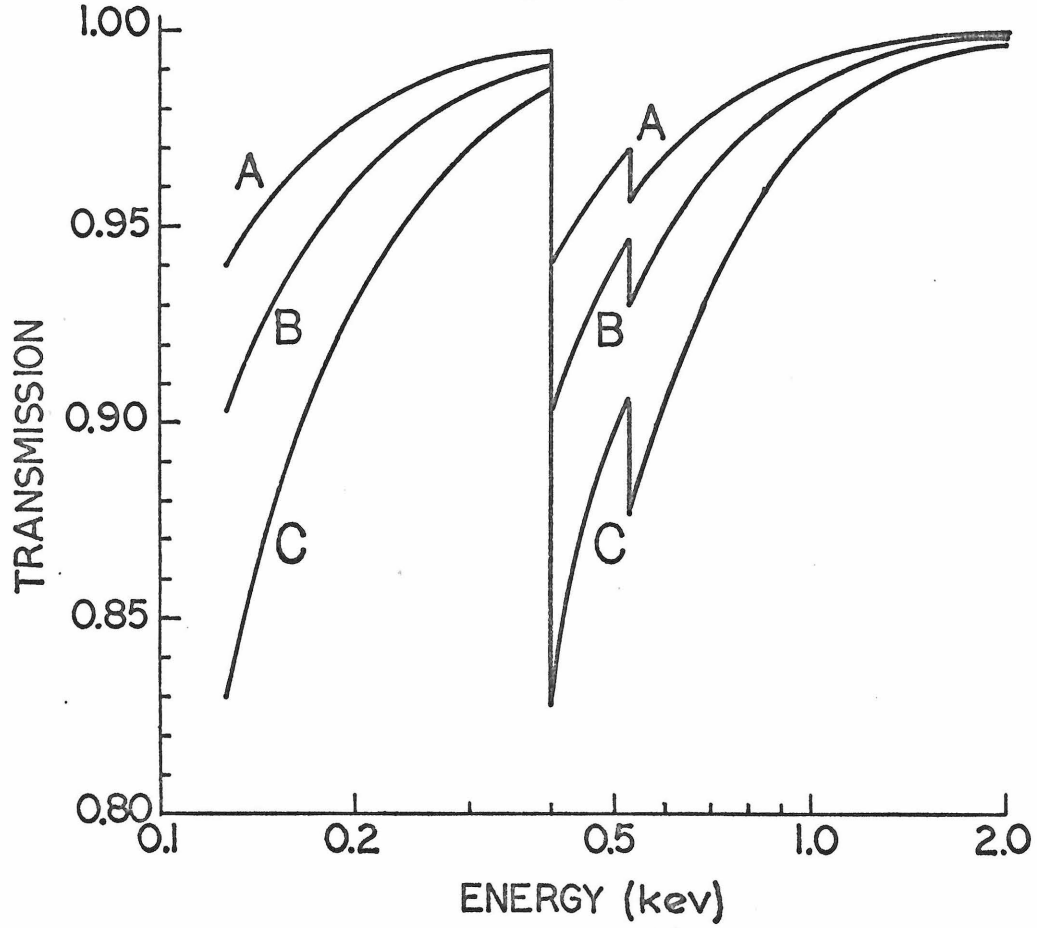

Figure 6.

the source along the line of sight. Unfortunately the atmosphere at high altitudes varies on both a diurnal and on an annual basis in a strongly unpredictable manner. This makes it difficult to ascertain with any certainty how much residual atmosphere is between the detector and the source. The integrated line-of-sight density also depends on the zenith angle of the observation. For the Cygnus Loop measurement the zenith angle was approximately 22°. The transmission as a function of energy of the residual atmosphere at this zenith angle for various altitudes using the U.S. Standard Atmosphere summer model 1 is given in figure 6. Note that the attenuation is greater than 5% at the nitrogen edge at 0.4 kev for altitudes less than 160 km. This effect is observable in the spectra obtained by detector C. To limit the inaccuracies caused by this uncertain amount of atmospheric attenuation, only the data obtained by detector C between 197 and 271 seconds was used for spectral analysis. Detector D performed filtered measurements of the Loop from 145 to 215 sec. Because of the low statistical accuracy of these filtered measurements the inclusion of atmospheric attenuation is not crucial.

C. Filters

As indicated above, detector D was equipped with a two-element filter system. The filters used were oxygen (O_2) gas and a thin teflon (CF_2) sheet. Both filters were normally removed from the detector's field of view and were independently inserted during the observation of the Cygnus Loop.

The teflon filter consisted of commercially available 675 $\mu gm/cm^2$ teflon sheet mounted on a frame which was hinged so as to lay flat in front of the detector during the measurement (figure 7). This teflon flap was motor driven and followed a sequence of positions during the flight. At launch the flap was in its 'closed' position in front of the detector. The flap was opened at approximately 93 sec and remained open until it was closed for the Cygnus Loop measurement at 173 sec. It remained closed until 213 sec, at which time it was opened. It was open until 362 sec when it was closed for reentry. The flap required approximately 1.5 sec to open or close. Because of the slow bleeding rate of the oxygen gas cell (see below) and also because of the programmed scanning pattern of the rocket, the maximum signal during the teflon filter measurement was seen during the interval 202 to 212 sec.

Figure 7. Photographs of the lower end of the rocket payload showing the teflon filter flap opened (figure 7a) and closed (figure 7b). The gas cell is also visible, being just behind the filter flap in its closed position. The wire with black and white beads on it is not part of the experiment but was included in the pictures to indicate angles more accurately. The camera used to take the star pictures which gave the rocket's aspect is visible above detector D.

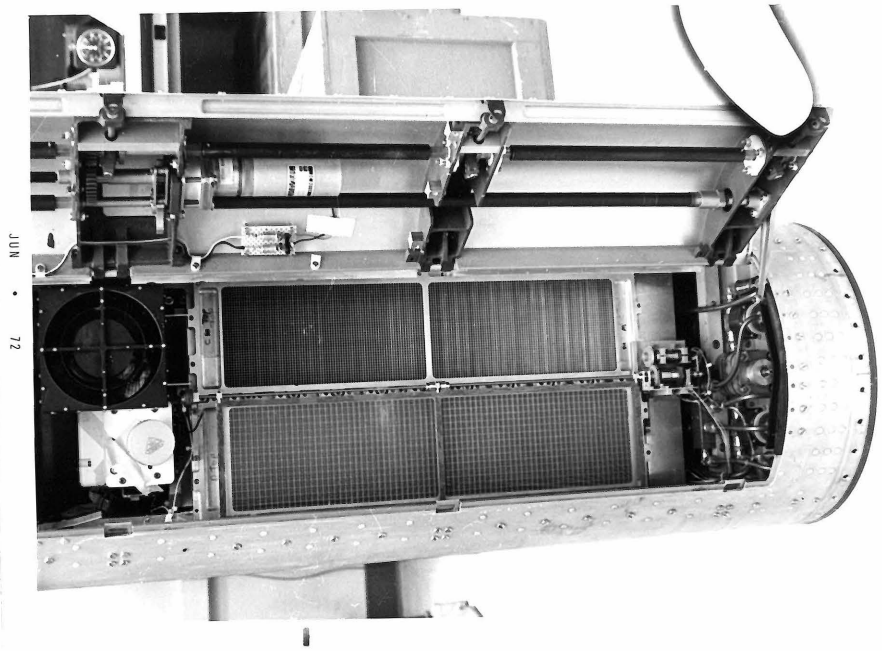

Figure 7b

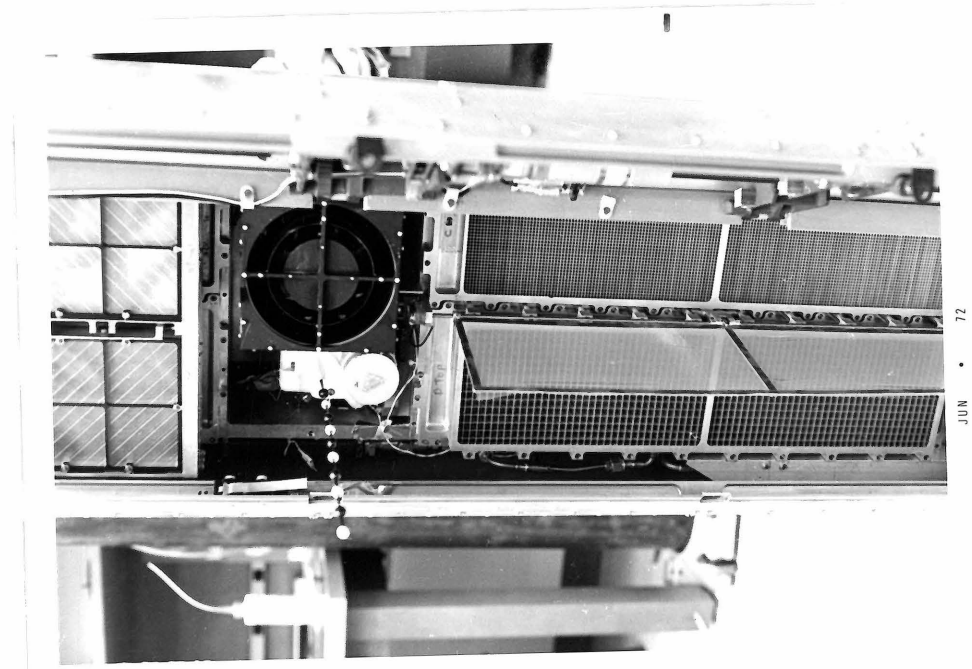

Figure 7a

The surface density of the teflon sheet was measured in two ways and was found to be 673 ± 34 $\mu gm/cm^2$. One way consisted of simply weighting a carefully measured area. The other way was to measure the x-ray transmission of samples of the filter sheet after flight. The transmission was measured at seven different energies between 0.28 and 1.49 kev. The technique was the same as that used to measure the surface density of the plastic used as window material and is described more fully in Appendix A. The two methods of measuring the surface density gave results consistent within the quoted accuracy.

The oxygen filter consisted of a gas cell located in front of detector D into which oxygen gas (O_2) could be admitted by means of a solenoid valve. This gas cell was normally vented to the ambient pressure. The pressure in the cell was monitored by a transducer and was recorded during the experiment. The pressure in the gas cell observed during the experiment is shown in figure 8. The gas cell was filled at 143 sec and began to empty at 173 sec. It emptied somewhat slower than expected. Examination of the pressure data shows step variations in the rate of escape of the oxygen. The slow bleed rate and the existance of step variations

Figure 8. Pressure of oxygen in the gas cell as a function of time. The gas cell was filled at approximately 143 sec and began to empty at approximately 173 sec. A change in the rate of empty occurs at ≈178 sec and another more abrupt at ≈198 sec.

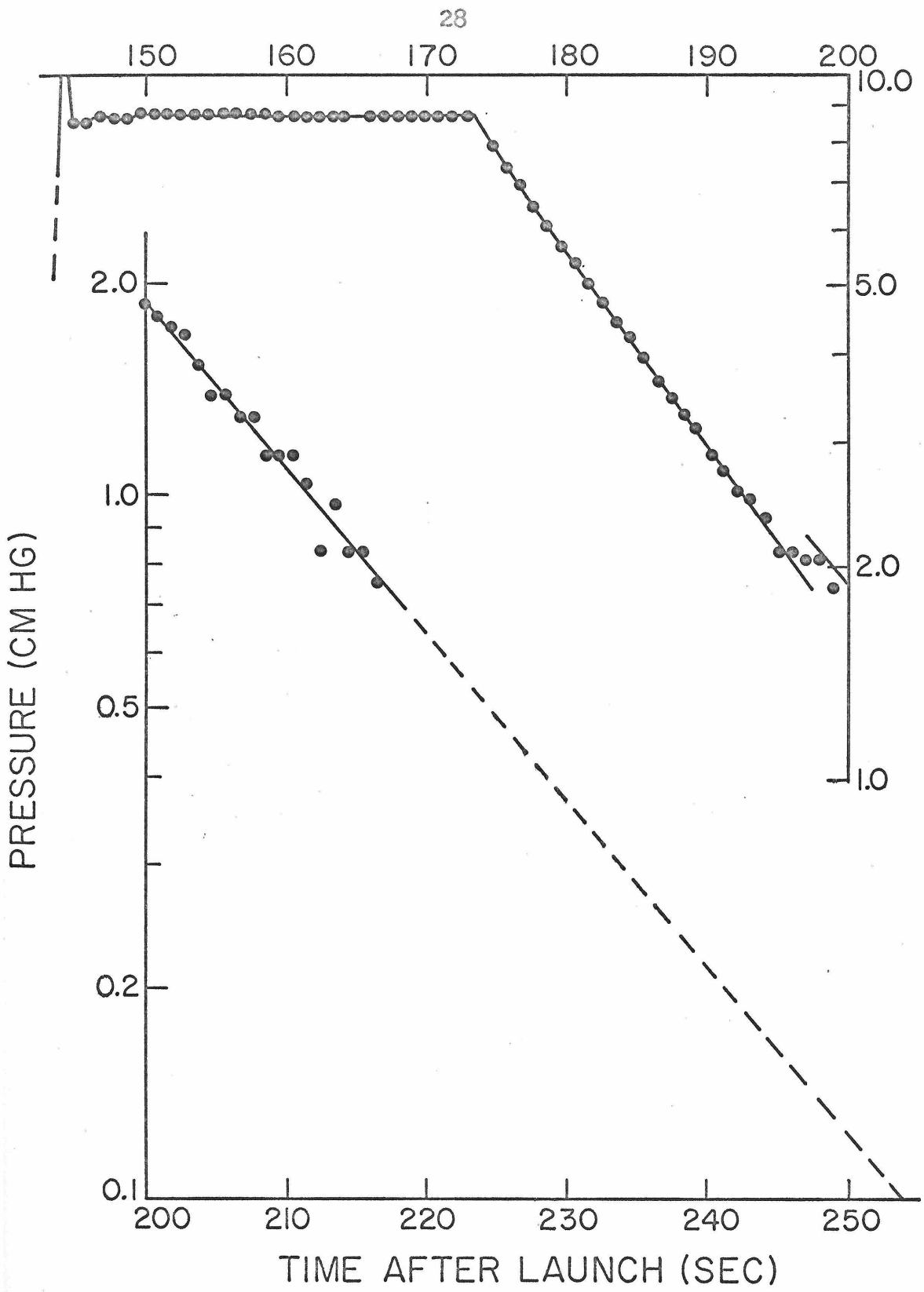
150
160
170
180
190
200
10.0
5.0
2.0
1.0
2.0
1.0
0.5
0.2
0.1
PRESSURE (CM HG)
200
210
220
230
240
250
TIME AFTER LAUNCH (SEC)

Figure 8.

in the bleed rate imply that the bleed orifice was too small and varying in size during the monitored time interval. Because of the slow bleed rate there was a substantial amount of oxygen in the cell during the teflon filtered measurement from 175 to 215 sec, and during the unfiltered measurement of the Loop from 215 to 270 sec.

The surface density of the oxygen filter during the time period 143 to 173 sec was 387 $\mu gm/cm^2$. The density of oxygen remaining in the gas cell during the period of maximum signal using the teflon filter (202 to 212 sec) ranged from 74 to 45 $\mu gm/cm^2$. The average surface density (taking into account the programmed motion of the rocket during this time period) was 57.4 $\mu gm/cm^2$. This amount of oxygen was included in the analysis of the teflon filtered measurements of the Loop. In addition the oxygen remaining in the gas cell was non-negligible until 250 sec so the data from the nominally unfiltered detector D before 250 sec was not included in the spectral analysis.

The oxygen used was research grade O_2 obtained from J. T. Baker Chemical Co. The minimum purity of the gas is given by J. T. Baker as 99.995%. Prior to its use in flight the oxygen was stored in a small gas tank which was part of the rocket payload. This gas tank was

tested for leakage over a 3 month period and did not leak to within the 1 mm Hg pressure sensitivity of the test. The pressure during the leakage test was 130 cm, the same as the pressure used in-flight.

The pressure transducer used to monitor the gas cell pressure was calibrated after the flight. The pressure was found to be determined to within ±0.1 cm above 1.0 cm Hg pressure, and with decreasing accuracy below this pressure. The region of relatively high accuracy includes both the oxygen and teflon filtered measurements.

D. Windows

The oxygen gas cell required two thin plastic windows to contain the oxygen. The innermost of these two windows also served as the window of the gas-filled proportional counter D. Both windows remained in front of the detector at all times during the experiment. This is why the window on detector D was approximately twice as thick as that on detector C.

The necessity of having two windows and the desirability of having a large transmission between 0.530 and 0.690 kev indicated that the windows should be made of a plastic containing a minimum of oxygen and nitrogen and as thin as possible consistent with

supporting the required pressures. Polypropylene plastic was used because it contains no oxygen and no nitrogen and can be stretched to micron thicknesses.

Some difficulty was encountered in obtaining large useable areas of polypropylene in sufficiently thin sheets. These sheets were finally obtained by cold stretching 0.0025 cm thick plastic until it was approximately 1 micron thick. It was possible to obtain sheets which were approximately 1.4 microns thick in circles of approximately 40 cm diameter. These sheets were uniform to about ±10% in the thickness. The details of the stretching procedure and of the mounting arrangement used in the experiment are given in Appendix C.

A total of ≈1500 cm^2 of ≈1.4 micron thick polypropylene plastic was used as window material on detectors C and D. This was the largest area of ≈1.4 micron thick polypropylene ever utilized in a rocket-borne experiment. Because windows of this type of plastic in this large area had not been previously flight-tested it was decided that the two spatial detectors (A and B) would use Kimfol plastic for their windows. Kimfol windows had been successfully used in several similar experiments before this experiment. The Kimfol plastic used was commercially available 270 $\mu gm/cm^2$ sheet.

The windows used in flight were recovered intact after the flight except for part of the window covering the gas cell which tore during reentry because of the slow leakage rate of the gas cell. The windows were calibrated by measuring their x-ray transmission properties. The details of this calibration are given in Appendix A.

E. Collimators

The field of view of the detectors was determined by mechanical collimators. For all of the detectors these collimators also provided support for the thin plastic windows. The collimators used have a rectangular field of view with a triangular, angular response function in each major direction. Detector C had only the window-supporting collimator. Detector D had two window-supporting collimators to support the two windows comprising the gas cell volume. These collimators and the window-supporting collimators on detectors A and B were of slat or egg-crate construction. They were built of 0.025 cm thick Al (alloy - 7075) sheet and were calibrated in the laboratory before the flight. The calibration procedure is discussed in Appendix B. The sheets were sanded prior to assembly and the assembled collimators were sandblasted with micron size glass shot to form a surface compatible with the thin plastic window material used. The sand blasting

and sanding produces a rough (to x-rays) surface on the slats and prevents grazing angle reflections which might increase the full width at half maximum (FWHM) of the collimators' angular response for the low energies of x-rays measured.

In addition to the window-supporting collimators, detectors A and B had additional mechanical collimators of a different design. The window-supporting collimators defined the long direction of the field of view and the additional collimators provided a narrow field of view ($0\overset{\circ}{.}4$ FWHM) in the other direction. These additional collimators were used to obtain the spatial mapping of the x-ray emission from the Cygnus Loop. The field of view of each of detectors A and B was a fan beam $0\overset{\circ}{.}4$ x $9\overset{\circ}{.}8$ FWHM. These fan beams were oriented at 90° with respect to each other and at 45° to the roll and yaw motions of the rocket. They formed an 'X' response pattern which was used to scan the Cygnus Loop as shown in figure 9.

The construction and calibration details of these narrow field of view collimators are given in Appendix B. These collimators are basically a stack of etched stainless steel grids whose shadowing properties are exploited to produce the single-maxima angular response function desired.

Figure 9. Scan path of experiment while viewing Cygnus Loop and counting rate of detectors A and B during the same period. The open circles give the view direction at intervals of 1 second. Not all of the positions are shown at the sharp corners at ≈190 sec and ≈230 sec. The 'X's marked with A's and B's denote the orientation of detector A's and detector B's fan beam collimator respectively. A sketch of the Cygnus Loop is shown for reference purposes. The counting rate data represent observed x-rays between 0.2 and 1.5 kev.

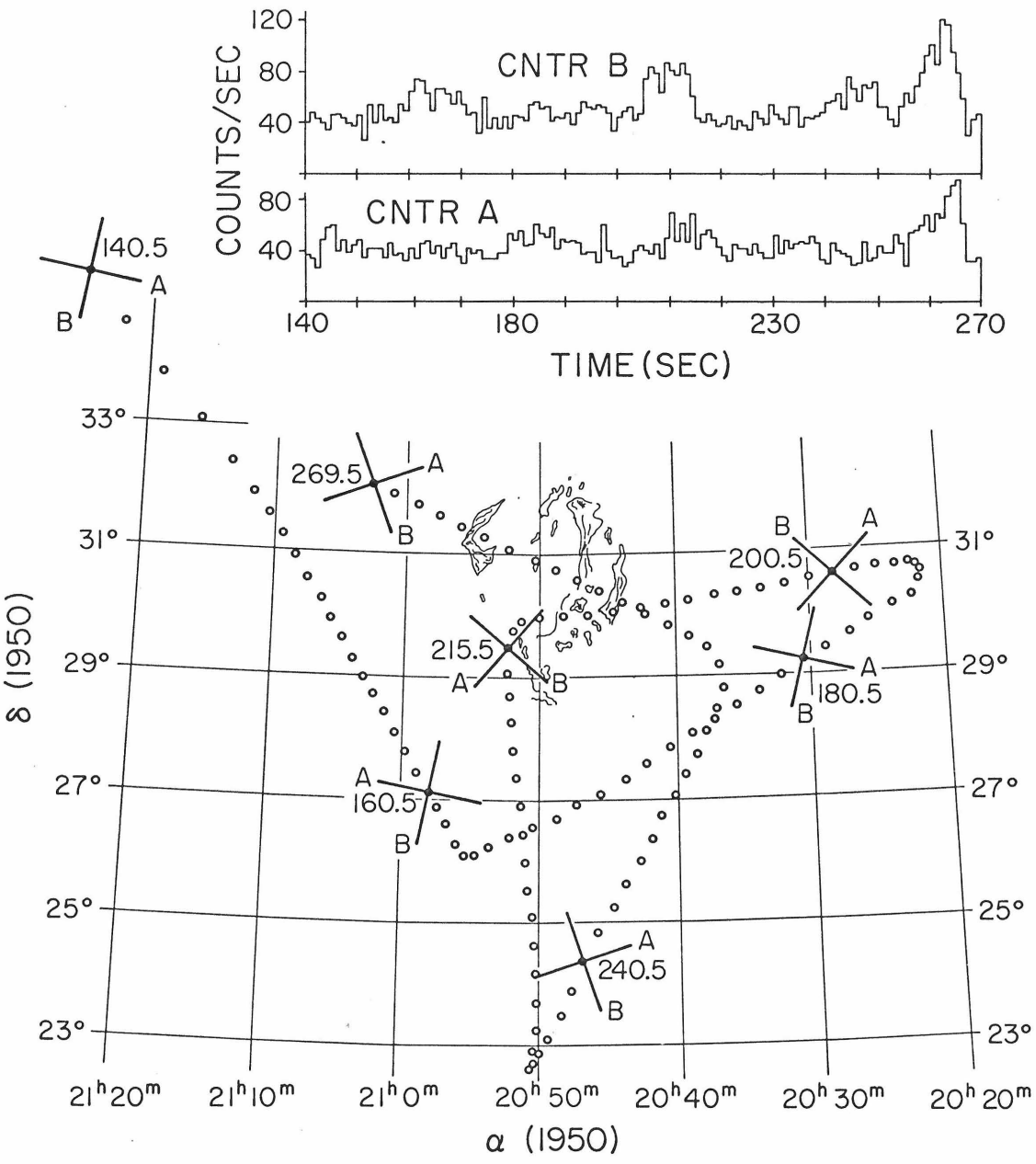
CNTR B
CNTR A
COUNTS/SEC
120
80
40
140
180
230
270
TIME (SEC)
140.5
A
B
269.5
215.5
200.5
180.5
160.5
240.5
33°
31°
29°
27°
25°
23°
δ (1950)
21h20m
21h10m
21h0m
20h50m
20h40m
20h30m
20h20m
α (1950)

Figure 9

F. Aspect Determination

This experiment determined its aspect with respect to the earth-based α, δ coordinate system by means of star pictures taken with a 16 mm camera. Each exposure lasted .954 sec. The time between frames was .036 sec. The exposures show streaks which are stars blurred by the rocket's motion. Which stars are detectable depends on the rocket's motion, on the magnitude and color of the star, on what camera is used, and on the type of film and the development techniques. The F1.5 lens on the 16 mm camera used in this experiment gives a field of view of $\approx 8^{\circ} \times 12^{\circ}$. This allowed positioning to $\approx \pm 5$ arc minutes while still permitting a large area of the sky to be photographed. The large area is essential for recording positions accurately during the fast ($2.^{\circ}0$/sec) scans used in maneuvering the rocket before and after the Cygnus Loop scans. Table 2 gives the limiting magnitudes of the stars which are visible at various scan rates using the camera described.

By cross referencing the collimators' angular responses to the camera (see Appendix B) and using the star pictures taken in-flight it is possible to determine where the x-ray detectors are pointing. The accuracy with which this determination can be made depends on

TABLE 2

STELLAR DETECTION LIMITS VS ROCKET ROTATION RATE

Rocket Rotation Rate (°/sec)	Magnitude of Stars Easily Detected	Limit of Detection
2.0	2.0	3.0
0.4	4.0	5.0
0.01	5.5	6.5

how well the calibration has been made and on how many stars are visible in the camera exposure of interest. Because the star tracks are streaks rather than points, it is necessary to estimate the same relative position along the streak for each streak. For each exposure (representing .954 sec) with sufficient star tracks a position and an angle can be obtained. The position is that of the normal to the rocket axis as determined by the main framework of the experiment. The angle represents the amount of tilt of the rocket axis relative to some fixed direction in space projected onto the sky in the direction of the rocket normal. The position can be determined by a single star track. The position and the angle can be determined if there are at least two star tracks on the frame. To a limited extent it is possible to extrapolate between frames containing sufficient stars by knowing what the attitude control

system (ACS) is doing during the same period. The ACS is a gyroscopically stabilized platform which controls the orientation of the rocket payload by means of a system of small gas jets. The ACS is monitored during the flight and gives information about the firing of the gas jets and about the relative angular displacement of the rocket payload and the stabilized platform. If the ACS indicates that no gas jets have been fired then it is possible to obtain the payload motion by interpolation between well determined positions. At all times while the Cygnus Loop was being viewed at least 3 stars were visible in each camera exposure. This enabled the position to be obtained to an accuracy of ±5 arc minutes. This figure includes the inaccuracies of the calibration procedure.

The ACS was supplied by the rocket personnel. For this experiment a STRAP-III system was used and it was programmed by Ball Brothers Research Corporation in collaboration with the Sounding Rocket Division of Goddard Space Flight Center. The scanning program is determined by the experimenter according to the celestial targets he wishes to examine. There are a number of external constraints which restrict the choice of scan program. There are only a limited number of segments in the program. Each segment is a rotation about one of

the three principle axis at a constant rate for a specified length of time. The rotation rates are limited to the range $5^{\circ}.0$/sec to $0^{\circ}.2$/sec. Only 5 independent rates are allowed; for this, rotations in opposite directions count as separate rates. In addition, there is of course only a limited time available for observations during any single rocket flight and, of considerable importance, the ACS has only a ±3 degree pointing accuracy in controlling the positioning of the rocket. For the spatial mapping of the Cygnus Loop it was found that deconvolution of the data requires at least 3 scans across the source in different directions and in general the more scans in different directions the less the inaccuracy involved in inverting the observations to arrive at the original source function. This is discussed at greater length in Appendix D. The combination of all these constraints coupled with a desire to spend as much time on the source as possible lead to the scan path shown in figure 9. The actual path followed in the flight is shown, not the path as programmed. The path as programmed called for the Cygnus Loop to be centered in the pattern of six scans. The actual path is approximately $2^{\circ}.5$ removed from the programmed path, a discrepancy which is commensurate with the quoted accuracy of the ACS.

III. THE SPATIAL STRUCTURE OF THE CYGNUS LOOP IN X-RAYS

A. Structure Obtained

The x-ray structure of the Cygnus Loop is presented in the form of an intensity map in figure 3. This structure was derived from the strip scans of the Loop performed by the fan beams of detectors A and B.

Figure 9 presents the data from which the intensity map was obtained. The data shown in figure 9 is the counting rate obtained from detectors A and B in the approximate energy range 0.2 to 1.50 kev. The upper energy cutoff was chosen so as to maximize the signal to noise ratio. The spectrum of x-rays from the Loop falls rapidly above 1.0 kev (see section IV). Hence the 1.5 kev cutoff contains at least 95% of the x-rays from the Loop. The lower energy cutoff was dictated by the threshold level of the electronics for signal acceptance. This discriminator level was not the same for both detector A and detector B. Detector A's discriminator level was ≈250 ev and detector B's ≈150 ev. This discrepancy in the acceptance threshold and a slight difference in the effective area of detectors A and B results in the difference in counting rates observed in the transit of the Loop at 260-270 sec (see figure 9).

The Loop was scanned 4 times by each detector (A and B). Examination of figure 9 reveals counting rates in excess of the background rate from 143 to 147, 179 to 192, 209 to 219 and 256 to 266 seconds for detector A and from 160 to 170, 205 to 214, 240 to 249, and 257 to 266 seconds for detector B. These are the times when each detector's field of view included some portion of the Cygnus Loop. The single-second wide peak in detector A's counting rate at 197 seconds is due to Cygnus X-1.

The entire time span shown in figure 9, from 140 to 270 sec, was inverted to obtain a map of that region of the sky in 0.2 to 1.5 kev x-rays. The inversion routine was an iterative process developed for this experiment. It is described in more detail in Appendix D. The routine treated an area of sky approximately 120 times the area of the Loop and was able to obtain a $0.^{\circ}5 \times 0.^{\circ}5$ mapping over ≈60% of this area (including the Loop itself). The Loop was approximately centered in this area. The Loop and Cygnus X-1 were the only two sources observed in this area. This result came from the x-ray map and was not used as an input condition. The inversion routine required no inputs other than the data observed. It therefore produces results which are free of experimenter bias. The map of the Cygnus Loop

obtained by this process is shown in figure 3. Table 3 gives the percentage of the total x-ray emission seen from each resolution element of the Loop. The relation between figure 3 and Table 3 is that a line in figure 3 represents ≈0.8% of the total x-ray emission from the Cygnus Loop.

The intensity map given in figure 3 represents some 1800 counts total received from the Cygnus Loop by both detectors A and B. The accuracy given in figure 3 is the noise level of the non-source regions of the obtained sky map. The non-source regions are those regions of the map obtained by excluding the Cygnus Loop and the response due to Cygnus X-1. This accuracy therefore represents both the inaccuracies resulting from number statistics and the inaccuracies involved in the inverting process.

An attempt was made to ascertain whether spectral differences existed between various regions of the Cygnus Loop by examining the spectrum of each $0.^{\circ}5 \times 0.^{\circ}5$ resolution element. However the low number of observed counts precluded the possibility of more than a two energy bin spectrum of each resolution element. Therefore the data was split into two energy bins, 0.2 to 0.56 and 0.56 to 1.5 kev and maps were obtained for each of these energy bins in the same way as for the whole energy interval.

TABLE 3

PERCENTAGE OF CYGNUS LOOP X-RAY EMISSION / RESOLUTION ELEMENT

(FRACTION OF RESOLUTION ELEMENT'S EMISSION > 0.56 kev)

$(\delta-\delta_o)$ \ $(\alpha-\alpha_o)$	$1^\circ.5$	$1^\circ.0$	$0^\circ.5$	$0^\circ.0$	$-0^\circ.5$	$-1^\circ.0$
$1^\circ.5$	0.0	5.2 (.79 ± .22)	1.4	12.1 (.44±.08)	5.8 (.65 ± .14)	0.0
$1^\circ.0$	3.7 (.30 ± .21)	8.6 (.48 ± .10)	2.9 (.65 ± .30)	4.6 (.76 ± .20)	3.7 (.42 ± .29)	1.8
$0^\circ.5$	4.3 (.58 ± .23)	1.5	8.3 (.73 ± .11)	0.3	-0.3	3.0 (.86 ± .66)
$0^\circ.0$	0.7	3.4 (.42 ± .39)	3.2 (1.0 ± .28)	-0.1	1.1	3.3 (.36 ± .25)
$-0^\circ.5$	0.0	4.3 (.51 ± .20)	5.2 (.53 ± .19)	2.0	4.4 (.93 ± .23)	0.0
$-1^\circ.0$	0.0	0.0	0.0	5.8 (.69 ± .14)	0.0	0.0

α_o is $20^h\ 50^m$ and δ_o is $30^\circ.5$ in 1971.8 coordinates.

The energy of the split (0.56 kev) was chosen so as to provide approximately equal counting rates in both energy intervals. The results obtained from these two mappings are also given in Table 3 for those resolution elements having more than 2.5% of the total emission from the Loop. For these elements the fraction of the observed x-rays having energies greater than 0.56 is given.

Except for the difference in discriminator levels the two detectors A and B are equally efficient in their detection of x-rays. Figure 10 shows the detection efficiency of detectors A and B to x-rays between 0.1 and 4.0 kev. In section IV it is found that a significant fraction of the observed x-rays from the Cygnus Loop is in line emission between 530 and 690 ev. Figure 10 shows that detectors A and B are relatively insensitive to this radiation. The intensity map given in figure 3 is only for x-rays observed according to the detection efficiency shown in figure 10. Extension of this map to other x-rays, such as possible line emission between 530 and 690 ev, should be done warily, bearing the spectral variations indicated by Table 3 in mind.

B. Structure Discussed

The x-ray structure of the Cygnus Loop (figure 3) shows correlations with the visual and radio structures.

Figure 10. Detector efficiency of detectors A and B as a function of photon energy. Efficiency is for 5.1 cm thick detector filled with methane gas at 150 torr with a Kimfol window of 270 $\mu gm/cm^2$ surface density. Absorption coefficients used in calculating this efficiency curve were taken from Henke et al (1967).

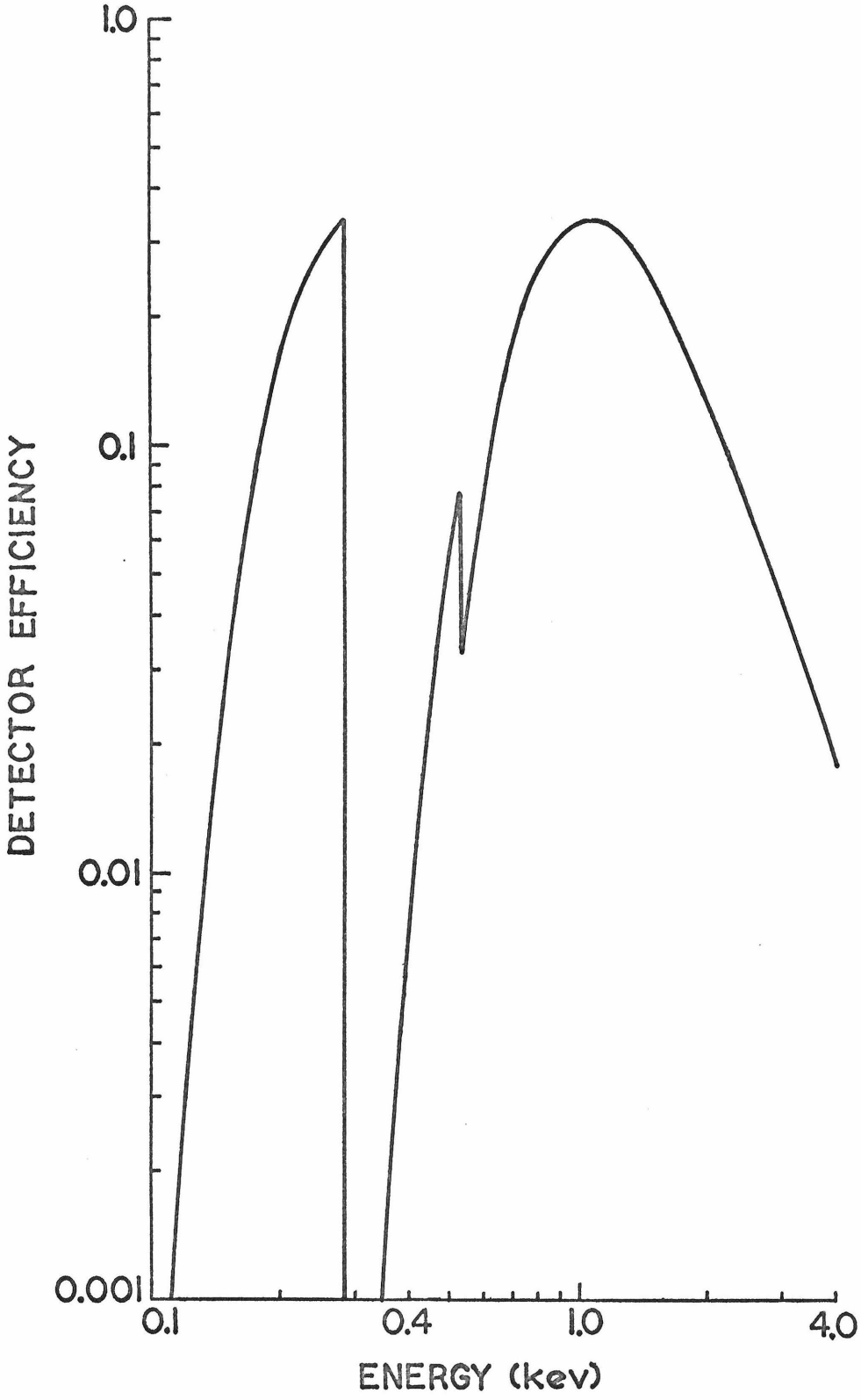

Figure 10

The bright visual emission region NGC 6992-5 (in the northeast portion of the Loop, see figure 1) is also bright in x-rays and in radio emission (figure 2). Similarly, NGC 6960 shows an $\approx 2\sigma$ enhancement in x-rays. The brightest resolution element in x-rays (in the northern region of the Loop) coincides fairly well with a relative maximum seen at long wavelengths in radio emission (Shklovskii, 1968), as does the southernmost element of the Loop in the x-ray map. However other relative radio maxima of comparable intensity show no enhancement in x-rays, so the correlation is not complete.

Several features of the x-ray mapping are conspicuous in their lack of correlating features in either radio or visual emission, and vice versa. The region below NGC 6992-5 in the southeast, which is a pronounced minimum in the radio maps (figure 2) and which shows very little Hα emission (figure 1) is a strong emitter of x-rays. In this respect the x-rays seem to define a more complete shell than either the visual or the radio emission shows.

The western half of the Loop shows a great deal of diffuse and filamentary visual structure. It is also a complex region of relative maxima at radio wavelengths. However in x-rays this region is much less intense than the eastern half of the Loop.

Further, the radio and visual emission continues to the south in the form of a large arc. This is the region of the Loop which displays large radio polarization (figure 2). The direction of polarization indicates that this arc contains material which has expanded along the local magnetic field and in so doing has formed the arc seen. The x-ray map does not rule out the possibility of emission from this arc but such emission must certainly be small. The only appreciable x-ray emission in this region of the Loop comes at a position which coincides well with the position of the relative radio maximum displaying no polarization.

The single most conspicuous resolution element is just east of the Loop's center. This element emits 1/12 of the total x-ray flux seen from the Loop and is uncorrelated with any radio or visual feature. It also shows a high percentage of 'hard' x-rays (Table 3). It is tempting to hypothesize that the stellar remnant of the supernova explosion is in this region and is responsible for this local maxima. However this x-ray data alone is not sufficient to warrant this hypothesis. This element is also the only region of pronounced x-ray emission which lies inside the shell of emission defining the edge of the Cygnus Loop. As such it is difficult to explain by the shock-wave models which can account for

the shell structure (see section VI).

Turning now to the question of whether spectral variations in the x-ray emission exist across the Cygnus Loop, the values presented in Table 3 turn out to be inconclusive. If the χ^2 criterion is used to judge whether the values of Table 3 are consistent with a constant fraction of x-ray emission greater than 0.56 kev, a value of this constant fraction of .57 is obtained. Using this fraction value the value obtained for χ^2 is 16.5 for 17 degrees of freedom. This implies that the values of Table 3 are indeed consistent with a constant fraction of x-ray emission greater than 0.56 kev. Hence this experiment must be regarded as inconclusive in regard to the existence of spectral variations within the Cygnus Loop.

IV. X-RAY LINE AND CONTINUUM RADIATION FROM THE ENTIRE CYGNUS LOOP

A. Overview

All four detectors used in this experiment were capable of yielding spectral information. Detectors A and B, because of their narrow collimation, did not provide a uniform sample of the spectrum of the Cygnus Loop in its entirety. Detectors C and D provide the best spectral information for the entire Loop. These detectors had large fields of view so they were able to view the entire Loop continuously while detectors A and B were viewing the Loop intermittently with their narrow fields of view. Detector D was also equipped with two filters to provide additional spectral information. Detectors C and D viewed the Loop continuously from 140 to 275 seconds. Detector D performed filtered measurements during 70 seconds of this time from 145 to 215 seconds. Detector C was unfiltered throughout the measurement, as was detector D from 250 to 275 seconds.

In section III it was shown that the x-ray surface brightness of the Cygnus Loop is spatially nonuniform. Besides the marked edge-brightening, figure 3 also shows intensity variations around the edge of the Loop. It seems probable that such intensity variations imply the

existence of spectral variations within the Loop. Experimental evidence of such spectral variations is not yet available, however the large physical size of the Cygnus Loop and the theoretical models presented in section VI support the hypothesis of such spectral variations. The overall spectrum of the Cygnus Loop is therefore most probably some form of average over dissimiliar regions having individually different x-ray spectra. The physical significance of the overall spectrum is therefore somewhat nebulous. Certainly comparison of the observed spectrum to detailed spectra calculated on the basis of a single temperature plasma would appear somewhat meaningless. Indeed, comparison to any spectral form has meaning only in providing a way, independent of detector parameters, of checking the observations against the results of future detailed models. To facilitate such comparison the observations should be described in terms of the simplest spectral models which provide consistency. This is the policy adopted below.

The filter system of detector D was designed to check for possible line emission between 0.53 and 0.69 kev. Shklovskii (1968) and Tucker (1971) have presented theoretical reasons for expecting line emission in this range of energies. Indeed, from an experimental

point of view, the reported observation of such radiation by Gorenstein et al (1971) is in itself sufficient reason to attempt confirmation of the line emission's existence.

B. Filtered Measurements of Cygnus Loop Spectra

The filters used were oxygen gas and a thin teflon sheet. More details concerning these filters are given in section II. Teflon sheet was used as a filter because it contains fluorine (CF_2). The presence of fluorine in the teflon produces a band-pass filter which transmits a narrow band of x-rays just below 0.69 kev, the fluorine K-edge. Similarly the oxygen serves as a band-pass filter transmitting a narrow band of x-rays just below 0.53 kev, the oxygen K-edge.

The oxygen filtered observations of the Cygnus Loop were from 144.0 to 172.9 seconds in the flight. The teflon filtered observations of the Loop were from 202.0 to 211.9 seconds. The x-ray fluxes observed during these periods of time were obtained by subtracting the instrumental background counting rate from the observed counting rate. The instrumental background rate is the rate which the detector records when the x-ray flux entering the detector is negligible. This condition was satisfied during two portions of the flight, from 82.0 to 93.9 seconds and again from 363.0 to 368.9 seconds when the

rocket was deep in the atmosphere and the teflon filter was in front of the detector. The counting rates observed during these periods of time are given in Table 4.

TABLE 4

OBSERVED COUNTING RATES (0.25 to 2.5 kev)

FOR DETECTOR D WINDOW

Detector	Time Interval (sec)	Average Counting Rate (Counts/sec)
window	82.0 to 93.9 plus 363.0 to 366.9	39.6 ± 1.5
	144.0 to 172.9	62.6 ± 1.5
	202.0 to 211.9	54.9 ± 2.3
middle+ side	82.0 to 93.9 plus 363.0 to 366.9	8.5 ± 0.7
	144.0 to 172.9	15.0 ± 0.7
	202.0 to 211.9	12.2 ± 1.1

These rates need to be corrected for the transmission of detector D's collimator. The average collimator transmission during the oxygen filtered measurement was 0.40 and during the teflon filtered measurement 0.59 . Using these values and the information given in Table 4 the fluxes detected during the filtered measurements are given in Table 5.

Because of the poor resolution of the detector it is

TABLE 5

FLUXES (0.25 to 2.5 kev) OBSERVED BY DETECTOR D DURING FILTERED MEASUREMENTS

Detector	Filter Material	Flux Detected (counts/sec)
Window	Oxygen	58.1 ± 5.3
Window	Teflon	25.9 ± 4.7
Middle+Side	Oxygen	16.4 ± 2.5
Middle+Side	Teflon	6.3 ± 2.2

not immediately apparent from the values given in Table 5 whether line emission has or has not been observed. To resolve this question it is necessary to assume trial input spectra and by convolving these spectra with the detector's efficiency determine the input spectral parameters consistent with the measurements. If the teflon filtered measurement then implies a much higher input spectral level than does the oxygen filtered measurement the existence of line emission between 0.53 and 0.69 kev will be demonstrated.

This detailed comparison is carried out in Appendix E. There it is shown that the teflon filtered measurement implies the existence of an excess emission over that expected from a simple thermal bremsstrahlung continuum in the energy range 0.53 to 0.69 kev. If this excess emission is assumed to come entirely from line emission

at 658 ev then an intensity in this line of 1.8±0.7 photons/cm^2-sec at the earth is needed to explain the observations. Similarly an intensity of 7.0±2.8 photons/cm^2-sec in a line at 575 ev is also consistent with the observations. These line intensities are relatively uncertain because of their large errors, however the values are significantly different from zero. A value as large as that obtained should occur less than 1% of the time by chance alone if the true line intensity was zero. The errors given are the statistical errors, they do not include the systematic errors. An estimate of the systematic errors can be obtained from the analysis of the unfiltered detector's measurements given below. The systematic errors, expressed as fractional errors, are much larger there (~25% in the intensity measurements) because of the higher counting rates seen in the unfiltered detector. It can be estimated that the lower filtered counting rate results in systematic errors of less than 5%. This size of systematic error does not significantly affect the measurements given above because of the relatively large statistical errors already present.

It has not been shown by this experiment that this excess emission must originate from the Cygnus Loop. This emission could conceiveably be a feature of the spectrum of the diffuse x-ray background radiation which

was also observed during the measurements of the Cygnus Loop. However the diffuse flux received by the detector was less than 1/6 of the Cygnus Loop flux. If this excess emission originates with the diffuse flux than the relative contribution of this excess emission to that of the continuum radiation is 6 times as large as it is for the Cygnus Loop. This excess emission represents 9% of the total energy flux observed from the Cygnus Loop so it would have to represent over 50% of the total energy flux from the diffuse background. The background radiation from a nearby region of the sky was examined during the same flight. This examination revealed no evidence for excess emission between 0.53 and 0.69 kev in the spectrum of this background radiation. This of course does not rule out the possibility that the diffuse background emission from the region of sky surrounding the Cygnus Loop is responsible for the excess emission observed, but it does render this possibility less plausible.

It should be emphasized that the excess emission given above represents the flux observed at the earth and not that emitted by the source. To arrive at the amount of excess emission which the source emits between 0.53 and 0.69 kev it is necessary to make an assumption about the amount of intervening absorbing material between the source and the detector. The unfiltered

spectra suggest that in the nomenclature introduced in Appendix E, $N_H = 0.47 \times 10^{21}$ atoms/cm^2. Using this value of N_H the interstellar transmission at 575 ev is 68% and at 658 ev is 77%. This leads to the following line intensities at the source; $I(658) = 2.3 \pm 0.9$ or $I(575) = 10 \pm 4$ photons/sec-cm^2.

Alternate ways of explaining the excess emission observed were investigated with uniformly negative results. These attempts at alternate explanations are discussed in the following paragraphs.

This excess emission could be explained if the teflon filter transmission had been underestimated. However, instead of 673 ± 34 μgm/cm^2, the measured surface density of the teflon sheet, a surface density of less than 480 μgm/cm^2 would be required for consistency of the filtered measurements without any excess emission. If the teflon filter were non-uniform, sections would have to display surface densities of much less than 400 μgm/cm^2. Both of these possibilites are inconsistent with the measurements made of the teflon sheet.

Similarly the excess emission could be explained if there were pinholes in the teflon sheet allowing a sufficient fraction of the Cygnus Loop spectrum through unattenuated. However, the fraction required, 2.7%,

is too large to be admissible since no holes were visible in a careful scrutiny of the teflon sheet after the flight.

Another explanation would require that the x-ray emission from the Cygnus Loop display large temporal changes during the filtered measurements. If the flux from the Loop were to have increased between the oxygen filtered measurement and the teflon filtered measurement by approximately a factor of 2 then this increase would have caused the observed excess flux in the teflon filtered measurement. Such an increase is incompatible with the observations of detector C which viewed the Loop without filters during this same interval of time. It is also inconsistent with the later unfiltered measurements by detector D itself which agree with the continuum level measured by the oxygen filtered detector.

Another proposed explanation of the excess emission seen would have the teflon filter flap acting as a fluorescence source and producing the excess emission seen by the detector. In its closed position the teflon flap was exposed to over 2 steradians of the sky with varying sensitivity (see figure 7b). Hence in addition to a large amount of x-ray diffuse background emission it also received emission from the discrete sources in this region of the sky; Cygnus X-1, Cygnus X-2, Cygnus X-3

and the Cygnus Loop. Therefore the amount of radiation impinging on its surface is potentially non-trivial. A calculation showed that the teflon sheet absorbed a total of 1.3×10^4 photons/sec above 0.7 kev from all of the above-mentioned sources. Assuming that the K-fluorescent yield of fluorine is $\approx 6.6 \times 10^{-3}$ (Gorenstein et al, 1968) then 85 photons/sec with energy 0.68 kev are generated in the teflon sheet. Of these $\approx$1.4 photons/sec escape from the teflon sheet in the appropriate direction so as to enter the detector. Finally only 7.5% of these x-rays, or 0.11 photons/sec, are transmitted by the two polypropylene windows prior to the window and absorbed by the detector gas. This falls far short of the $\approx$12 photons/sec needed to explain the excess emission observed.

C. Unfiltered Spectral Measurements of the Cygnus Loop

Detector C provided the best unfiltered measurements of the entire Loop because its window was only half as thick as the windows of detector D. In addition detector C viewed the Loop for over 130 seconds while detector D had only some 60 seconds of unfiltered observations of the Loop.

The statistical accuracy of the spectral data received by detectors C and D was quite high because of

the large flux of soft x-rays coming from the Cygnus Loop. Energies were recorded for over 101,000 detected events while the experiment was observing the Cygnus Loop. However not all of the photons for which energies were available were used to obtain the Cygnus Loop spectra. As mentioned in the description of the experiment in section II the atmospheric absorption effects limited the spectral measurement by detector C to the time period 197.0 to 270.99 seconds and the presence of some residual oxygen in the gas cell limited the unfiltered measurement by detector D to the time period 255.0 to 270.99 seconds.

The number of x-rays observed by each detector and used to give the spectra discussed below is given in Table 6.

The numbers given in Table 6 were obtained by subtracting the number of counts due to instrumental events and due to the diffuse x-ray emission from the number of counts observed while viewing the Cygnus Loop

TABLE 6

NUMBER OF X-RAYS FROM CYGNUS LOOP
USED TO OBTAIN OVERALL SPECTRA

Anode Wire Group	Detector C	Detector D
Window	34900	5100
Middle	8000	1000
Side	7500	900

during the time periods given above. The Cygnus Loop spectra discussed below were obtained in a similar manner by subtracting the background spectrum from the observed spectra. The number of counts (spectra) due to the combined instrumental and diffuse backgrounds was estimated from the rate observed during a later portion of the flight from 284 to 297 seconds. During this period of time the experiment was scanning between the Cygnus Loop and the Perseus cluster of galaxies. The region of sky examined during these 13 seconds was from $\alpha(1950) = 21^h$ to $\alpha = 2^h$ and from $\delta = 40^o$ to $\delta = 30^o$. The observations show that this region is featureless and free of discrete sources. The possibility exists that this region of sky is a significantly different source of discrete x-rays than is the region containing the Cygnus Loop. However if the difference is only one of intensity then the amount of background subtracted is still correct since this amount was normalized by looking at the x-rays with energies > 2.5 kev. The Cygnus Loop does not radiate significantly above 2.5 kev (Bleach et al, 1972), so that this region of the spectrum always represents the contribution due to the instrumental and diffuse backgrounds.

The corrections to the observed data due to this background subtraction were almost negligible (4%) for

detector C window and somewhat more significant for detector D window (17%). This correction was most significant in the middle and side detectors but even there it amounted to less than a 25% correction. The difference in the significance of this correction for the various detectors itself supports the validity of the correction since the different detectors give substantially the same results for the various spectral models discussed below. If the background subtraction was inappropriate and significant then the different detectors would arrive at different spectra for the Loop.

Spectra of the Cygnus Loop were obtained independently from six detectors, C window, C middle, C side, D window, D middle, and D side by correcting the observed spectra for the background as described above. The standard approach (Gorenstein et al, 1968) was employed to obtain the source spectrum from these observed spectra. This consists of assuming trial spectra attenuated by the interstellar gas and folding these spectra through the detector's efficiency and resolution functions to obtain predicted spectra. These predicted spectra are compared with the observed spectra using the χ^2 criterion to test for significance of agreement.

This process is carried out in Appendix F. Source spectra were obtained for each of the six detectors.

These source spectra were then combined to arrive at the Cygnus Loop spectra given in Table 7. The details are given in Appendix F.

TABLE 7

CYGNUS LOOP SPECTRA

Spectral Model*	A	kT (kev)	α	$N_H \times 10^{-21}$ (atoms/cm^2)	$I_o(658)$ (photons/cm^2-sec)
TB + L	130±30	.25±.02	---	.48±.02	1.4±0.5
TB	210±50	.23±.01	---	.55±.04	---
PL + L	2.1±1.1	---	4.4±0.3	.93±.13	2.3±0.5
PL	2.9±0.8	---	4.6±0.2	1.09±.06	---

*TB, PL, and L are Thermal Bremsstrahlung, Power Law and Line emission respectively. The functional form of these spectra are given in Appendix F.

Of the spectra given in Table 7 only the thermal bremsstrahlung with and without line emission can be regarded as giving a good fit to the observed data. For these two spectra the thermal bremsstrahlung with line emission gives a significantly better fit than does the thermal bremsstrahlung spectra alone. The power law spectra with or without line emission do not give an adequate fit to the observed data.

The value of the line emission given in Table 7 for the thermal bremsstrahlung model 1.4 ± 0.5 photons/cm^2-sec can be compared with the value found above from the

filtered measurements of 2.3 ± 0.9 photons/cm^2-sec. These values agree within their admittedly large errors.

The fact that the spectra are best fit by a thermal bremsstrahlung model should not be regarded as very strong evidence that the x-rays represent free-free emission from a plasma. In light of the intensity variations observed across the Loop by detectors A and B this overall spectrum must be regarded as a composite spectrum originating in a number of dissimilar regions. In section VI an inhomogeneous anisotropic model based on the interaction of a shock-wave with the interstellar medium is proposed to account for the observed x-ray spatial structure. The overall spectrum from the Loop is also calculated for this model as a summation over regions representing a continuum of temperatures and densities. It is found that such summations often appear quite similar to simple thermal bremsstrahlung or power law spectra as used above. So the fact that a simple approximation to a thermal bremsstrahlung spectrum fits the observed spectra should be regarded as fortuitous rather than conclusive.

The auxiliary fact that the fit is improved by the addition of line emission tends to verify the line emission observed using the filters. The closeness of the intensities of this line emission obtained by these two different measurements serve as a further verification of

the existence of this line emission. Such line emission is unlikely to be present if the x-ray emission mechanism is other than emission from a hot plasma.

The amount of energy observed at the earth from the Cygnus Loop can be calculated using the spectra given above. Because of the amount of intervening absorbing material this energy flux is essentially completely contained in the energy interval 0.2 to 1.5 kev. This experiment saw $1.2 \pm 0.3 \times 10^{-8}$ ergs/cm^2-sec in x-ray emission from the Cygnus Loop. Line emission appears to be present with an energy flux of $1.1 \pm 0.4 \times 10^{-9}$ ergs/cm^2-sec, which represents $9 \pm 4\%$ of the total energy flux seen from the Loop.

The amount of energy emitted by the source above a certain energy can also be obtained from these spectra by assuming a distance to the source. If this distance is taken to be 770 pc, then the Cygnus Loop emits $2.1 \pm 0.5 \times 10^{36}$ ergs/sec in x-rays with energies greater than 0.2 kev.

Finally, assuming that the observed radiation is free-free emission from a volume containing plasmas at different temperatures and densities, an integral relation for n^2/T, the local number density squared divided by the local temperature of the plasma, can be obtained. Cox (1972) gives an approximation to the amount of x-ray

energy emission, L, from a plasma between 10^5 and 10^7 ^oK from a calculation including line emission, free-free emission and radiative recombination processes. He finds:

$$L \approx 1.35 \times 10^{-16} \, n^2/T \text{ ergs/cm}^3\text{-sec}$$

where n is the number density in cm^{-3} and T is the temperature in ^oK of the plasma. This luminosity when integrated over the volume of the source gives the total energy emitted. Equating this to the total observed energy emission gives

$$1.35 \times 10^{-16} \int \frac{n^2}{T} dV = (2.1 \pm 0.5) \times 10^{36}$$

which leads to

$$\int \frac{n^2}{T} dV = (1.6 \pm 0.4) \times 10^{52} \text{ cm}^{-3} \, ^oK^{-1}$$

D. Temporal Variations in the X-Ray Emission from the Cygnus Loop

Because of the established existence of periodic pulsations in the x-radiation from at least 3 celestial objects and because in at least one of these objects, the Crab Nebula, this pulsed radiation is associated with the site of a recorded supernova, the x-ray emission from the Cygnus Loop was examined carefully for evidence of pulsations. The results of this examination were

uniformly negative. Upper limits on the percentage of pulsed emission with periods between ≈20 msec and ≈120sec were obtained from the experimental observations of detector C.

For periods between ≈20 msec and ≈2 sec a power spectrum was obtained by fourier transforming the data recorded by detectors C middle and C side as a function of time. These two detectors recorded ≈26,500 total counts during the Cygnus Loop measurement from 140 to 270 seconds. The power spectrum is shown in figure 11. An upper limit to the pulsed fraction was obtained by artificially introducing a periodicity into the data and noting at what signal level this periodicity disappeared. It was found that a periodic signal with a period between ≈20 msec and ≈2 sec and with an intensity of ≈2% of the total observed Cygnus Loop intensity would have been barely discernible if present.

For periods between ≈2 sec and ≈120 sec the intensity recorded by detectors C middle and C side was corrected for long-period systematic effects such as collimator response and deadtime corrections. The resultant intensity profile displayed no periodic fluctuations with periods between ≈2 sec and ≈120 sec larger than the noise level of ≈10% of the total intensity.

Figure 11. The power spectrum of the counting rate observed by detectors C middle and C side during the Cygnus Loop measurement. No periodic components are discernible in this spectrum.

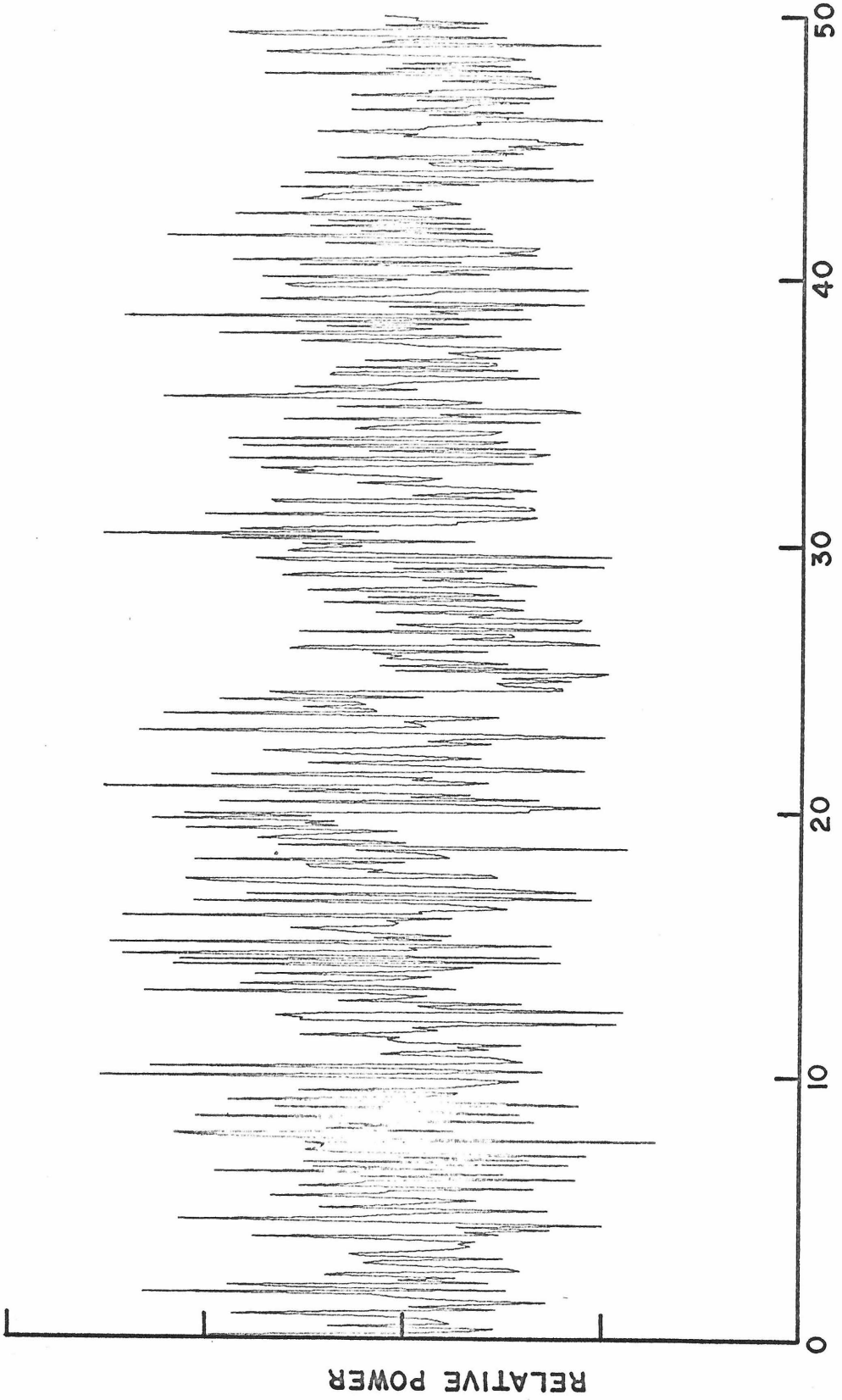

Figure 11

V. SUMMARY OF RESULTS AND COMPARISON WITH PREVIOUS OBSERVATIONS

A. Summary of Experimental Results

The results separate into two types, spatial results and spectral results. The spatial results were presented in figure 3 (pg. 12) and in Table 3 (pg. 43) . Figure 3 gives an intensity map of the Cygnus Loop in 0.2 to 1.5 kev x-rays. Table 3 gives the same information in numerical form. An attempt was made to discern spectral variations within the Loop without success.

The spectral results consisted of measurements of the x-ray continuum and line emission from the Cygnus Loop. An oxygen and teflon filter system was used to establish the presence of an excess emission over that expected on the basis of a simple thermal bremsstrahlung continuum spectrum. This excess was shown to be contained within the energy interval 0.53 to 0.69 kev. The energy distribution of this excess emission between 0.53 and 0.69 kev is indeterminable from this experiment. The intensity of this excess emission depends on the assumed energy distribution. For a single line at 658 ev this emission has the intensity 1.8 ± 0.7 photons/cm^2-sec at the earth. For a single line at 575 ev this excess emission has the intensity 7.0 ± 2.8 photons/cm^2-sec.

The continuum observations showed that the overall spectrum of the Cygnus Loop is well represented by a simple thermal bremsstrahlung spectrum with line emission. The characteristic temperature is 2.8 million degrees ($kT = .25 \pm .02$ kev). The amount of line emission at 658 ev was found by these continuum measurements to be 1.4 ± 0.5 photons/cm^2-sec (before interstellar absorption). The intensity of the x-ray emission from the Cygnus Loop observed at the earth was found to be $1.2 \pm 0.3 \times 10^{-8}$ ergs/cm^2-sec between 0.2 and 1.5 kev. The line emission represents 9 ± 4 % of this energy flux. The intensity of the source was found to be $2.1 \pm 0.5 \times 10^{36}$ ergs/sec in x-rays with energies greater than 0.2 kev. This value includes the effects of interstellar absorption at a columnar density of $.48 \pm .02 \times 10^{21}$ H atoms/cm^2.

A search for periodic pulsations in the x-ray emission from the Loop indicated no pulsations for periods between ~20 msec and ~2 sec with an upper limit of ~2% of the total x-ray emission. For periods between ~2 sec and ~120 sec the upper limit was ~10% of the total x-ray emission.

B. Comparison With Previous Observations

The most detailed spatial results prior to this experiment were those of Gorenstein et al (1971). These authors used a one-dimensional focusing x-ray detector

in a single scan across the Loop to obtain a "strip map" of the Cygnus Loop. They did not however attempt to deconvolve their data to obtain a map independent of their collimator response. The map they published is apparently a simple summation of the responses seen by their eight separate detectors. Hence their map and the map obtained by this experiment are not directly comparable. Since the angular response of their proportional counter element A was not completely given and since the shape of their detector's collimation in the long direction was not published, detailed quantitative comparison of the results of this experiment to the 1-dimensional map obtained by these authors is not possible. A rough comparison made, assuming that their collimation was approximately flat in its long direction, indicates that the two maps share some qualitative features. An example of the qualitative agreement is provided by the brightest resolution element of figure 3. This bright spot is at the correct location to cause the enhancement seen in the strip map. Their data exhibits internal inconsistencies which were not explained. Their proportional counter elements B and C have almost the same measured angular response to a point source. However the angular extent of the Loop as measured by their element B is much larger than that measured by element C. Also their elements A and D show

anomalous changes in their respective background rates which are not explained. Finally the angular response of their detector exhibited significant "wings" extending beyond the main response. Because of these difficulties, because the collimation of this experiment was triangular with no wings and because of the many scans across the Cygnus Loop employed in this experiment, the map produced by this experiment is felt to give a more accurate representation of the x-ray emission from the Cygnus Loop than that given by Gorenstein and co-workers. Because the broadening due to the collimator's angular response has been removed from the data in obtaining the map given in figure 3, and also because the map is a 2-dimensional representation, it is felt that this map is more intrinsically useful than that given by Gorenstein et al.

The spectral results of this experiment are also only in partial agreement with the results given by Gorenstein et al. They give the observed integrated intensity as 1.3×10^{-8} ergs/cm^2-sec, this experiment observed $1.2 \pm 0.3 \times 10^{-8}$ ergs/cm^2-sec. Both this experiment and the experiment of Gorenstein et al agree that the spectrum of the Cygnus Loop is well represented by a simple thermal bremsstrahlung continuum spectrum with line emission. However, this experiment finds different values for the spectral parameters. They found that 30% of the x-ray

emission was in a line at 650 ev. This experiment found a much lower value 9 ± 4 % of the total x-ray energy emission to be in line emission if the line is assumed to be at 658 ev. Their temperature of 4×10^6 °K is to be contrasted with the value found by this experiment of $2.8 \pm 0.2 \times 10^6$ °K. The amount of interstellar absorption also differs being $4.8 \pm 0.2 \times 10^{20}$ H atoms/cm^2 for this experiment and 2.6×10^{20} H atoms/cm^2 for the experiment of Gorenstein et al.

The spectral results of this experiment are therefore quite different quantitatively from those of Gorenstein et al. Since they did not give any indication of how large the errors in their spectral parameters were it is not possible to tell if the two experiment's results are indeed statistically consistent. However such consistency would require large errors in their results. This experiment used some 57,000 x-rays observed from the Cygnus Loop to obtain the Loop's spectrum. Gorenstein et al observed only some 1500 x-rays. In addition the details of the spectral reduction given in Appendix F show that when a single proportional counter is used in an attempt to observe line emission the results are highly subject to systematic errors. Their experiment also had to contend with the effects of the chromium L-edge on the reflection efficiency of their mirrow system. This

experiment was free of such difficulties. The line emission was observed by this experiment in two independent ways and the results were statistically consistent. This in itself lends support to the values found herein. For these reasons it is felt that the spectral results found by this experiment are more accurate than those of Gorenstein and collaborators.

VI. INTERPRETATION OF RESULTS IN TERMS OF A SHOCK-WAVE MODEL OF THE CYGNUS LOOP

A. Overview

The total observational information available on the Cygnus Loop is varied in both wavelength and in spatial resolution. To the data formerly available the results of sections III and IV can now be added. Parker (1964) and van der Laan (1962) have presented explanations of the observed visual and radio emission respectively, based on shock-wave models of the Cygnus Loop. Cox (1972) and Tucker (1971) have recently proposed theoretical models to account for the x-ray emission seen by Gorenstein et al (1971). Their works were based extensively on prior formulations of the same problem by Heiles (1964), Shklovskii (1968) and others.

Tucker considered several possible models and concluded that either a synchrotron model with extreme parameters or a shock-wave model with shock front expansion velocities of 400-600 km/sec would give the observed x-ray emission. This expansion velocity is 4-5 times the spectroscopic velocity of the filaments, 115 km/sec, measured by Minkowski (1958) and more recently by Doroshenko (1971).

The primary objection raised against this shock wave model has been this apparent discrepancy in velocities. However these previous models have tacitly assumed that the entire emission is from the plasma just inside the shock front at a particular temperature T_s. In fact, similarity solutions to the problem of a violent explosion in a medium of constant heat capacity given by Sedov (1959) suggest that the temperature, T, of the plasma increases and its density, ρ , decreases with increasing inward displacement away from the shock front. Since the total emission from a hot plasma is proportional to ρ^2/T for temperatures between 10^5 and 10^7 ^oK (Cox, 1972) the major portion of the radiation will indeed come from just inside the shock front. However if a shock velocity is assumed which is consistent with the filaments' velocity of ≈115 km/sec then the temperature just inside the shock will be ≈300000 ^oK and this maximum in the emission will occur mostly in the far ultra-violet and in the very soft x-ray range, $E < 0.1$ kev. This radiation is readily absorbed by the interstellar material and beyond ≈200 pc from the source only the harder x-rays with energies greater than ≈0.1 kev are visible. These x-rays are produced by the gas somewhat inside the shock front. This gas is hotter and less dense than the gas just inside the shock front.

It therefore produces higher energy photons than those from the shock front but at a somewhat lower intensity. The spectrum obtained by combining the radiation from these regions of different temperatures and densities is explicitly calculated below for a proposed inhomogeneous model of the Cygnus Loop. Prior to the development of this model evidence supporting the inhomogeneous anisotropic nature of the Cygnus Loop is cited. The developed model is shown to provide an explanation of the spatial structure and to a lesser extent the spectral nature of the x-rays from the Cygnus Loop. For completeness the predictions of the model proposed by Tucker, having the high expansion velocity, are also calculated and presented.

B. Evidence Supporting Inhomogeneous And Anisotropic Nature of The Cygnus Loop

In this discussion the Cygnus Loop is regarded as the visible remains at all wavelengths of the interaction between the ejecta from a supernova, its shock-wave and the interstellar medium. The model described below seeks to explain the observed x-ray structure of the Cygnus Loop in terms of this interaction. The physical quantities of interest in this description are ρ , the mass density of the plasma occupying a particular spatial

position and T its temperature; c , the shock velocity; ρ_i , the initial interstellar mass density before interaction with the shock and E_o , the energy of the initial supernova explosion involved in mass motion. T, ρ, and ρ_i are in general functions of spatial position. The geometry of the explosion prompts the use of spherical coordinates, (r, θ, ϕ), to describe the spatial position. In what follows a quantity will be said to be isotropic if it is independent of both ϕ and θ, and homogeneous if it is independent of r. Since only the projection of the Cygnus Loop along the line of sight is available for study, observational anisotropy will mean a dependence on θ in the projected coordinate system (r,θ).

Previous models of the Cygnus Loop have assumed an initially homogeneous and isotropic distribution of the interstellar material. The passage of the shock wave outward through this medium introduces a radial dependence but does not disturb the symmetry so ρ and T inside the shock are inhomogeneous and isotropic. The radial dependencies of ρ and T are fixed by the initial radial distribution of the interstellar material. Inhomogeneity of the initial distribution of the interstellar material therefore is reflected in the final radial dependence of the observable quantities but in a non-trivial way. Anisotropy of the observables

immediately implies anisotropy of the initial distribution of matter. The present claim is that the observations require an inhomogeneous anisotropic initial distribution of the interstellar medium.

The spatial structure of the Cygnus Loop at all the observed wavelengths supports the anisotropic nature proposed. Besides the detailed anisotropies such as particular filaments, there are also large scale anisotropies such as the arc extending to the southwest in the Hα and radio maps. The x-ray structure also supports this anisotropy, the western half of the Loop being noticeably a weaker source of x-rays.

The x-ray structure in particular requires an inhomogenous initial distribution of the interstellar matter if the expansion velocity is assumed consistent with the spectroscopically observed filament velocity. The discussion below of the proposed model includes a discussion of the homogeneous case. It will be shown below that for a shock velocity consistent with the measured filament velocity of 115 km/sec the radial dependence predicted in the homogeneous model for the surface brightness exhibits a peak at 0.6 r_s, where r_s is the radius of the shock front. The x-ray map (see figure 3) does not permit such a radial dependence. This map shows that the x-ray emission is largely

concentrated in the ring r = 20±4 pc, i.e. between 0.8 and 1.2 r_s. The shock front radius, r_s, is assumed to be the distance from the geometrical center of the Loop to the edge of the bright filaments. This is consistent with the explanation of the observed radio emission structure since the radio emission is supposed to come from just in front of the shock wave. The homogeneous model having the high shock velocity cannot be ruled out by this argument. This discussion is expanded below in the development of the proposed models.

Indeed the Cygnus Loop occupies a volume sufficiently large that inhomogeneities would be expected to be present solely on the basis of studies of the interstellar medium. The size and distance of the Loop are determined from a measurement by Hubble (1937) of the diametral angular expansion rate of 0.06"/yr combined with the measured spectroscopic velocity of 115 km/sec. Assuming that the filaments expand at the same velocity normal to the line of sight as they do along the line of sight leads to a distance of 770 pc and a diameter of 40 pc for the Cygnus Loop.

Spitzer (1968) gives the size of interstellar clouds as ≈14 pc and their average number per kpc^3 as 5×10^4. The center of the Cygnus Loop is at $b^{II} = -8^o$. Assuming that it is at a distance of 770 pc then it lies

110 pc below the galactic plane. This displacement from the plane decreases the density of interstellar clouds by about a factor of e (Lequeux, 1969). Thus the 40 pc diameter spherical volume of the Loop should contain approximately one cloud. The hypothesis that NGC 6992-5 is a region where the shock wave has recently encountered such a cloud seems somewhat warranted.

Besides the probable existence of this cloud there is an easily visible dust lane to the west of the Cygnus Loop which suggests initial inhomogeneities. Oort (1946) mentioned this lane and speculated about the possibility of interaction between it and the shock front. Since the boundary of a portion of this dust lane coincides with the edge of the bright Hα filamentary structure at the western edge of the Loop, NGC 6960, this interaction seems quite likely. Detailed comparison of the Palomar Sky Survey red and blue plates of this region reveals some dark nebulosity extending into the topmost filaments of the Loop. The existence of such regions of nebulosity further supports the inhomogeneous anisotropic nature suggested for the Cygnus Loop.

C. Inhomogeneous Isotropic Model of the Cygnus Loop

The model developed herein is inhomogeneous in that prior to the supernova explosion the interstellar

material is assumed to be distributed according to $\rho_i = \rho_o(r_i/r_o)^n$. Here ρ_i and ρ_o are the initial densities at the radii r_i and r_o respectively. The radius r_o is taken to be slightly larger than the shock front radius, r_s, so that ρ_o becomes the interstellar density just in front of the shock wave. This radial dependence was chosen because it allows analytical solutions to be obtained for the temperature, T , and density, ρ , as a function of the radius, r , after the passage of the shock wave. These solutions have been given by Sedov (1959). Sedov gives parametric equations for T/T_s , ρ/ρ_s and r/r_s . The subscript s is used to denote the values of the quantities just inside the shock front. These dimensionless quantites, T/T_s , ρ/ρ_s and r/r_s are independent of time. The quantities T/T_s and ρ/ρ_s can without loss of generality be considered as functions of r/r_s. Since Sedov's parametric equations are somewhat involved, the dependence of T/T_s and ρ/ρ_s on r/r_s is graphically given in figures 12 and 13.

Before these solutions can be employed to calculate the x-ray emission the dimensional quantities T_s and ρ_s must be related to observational quantities. T_s , ρ_s and r_s are time dependent quantities. They are determined from the conditions on the shock front and from the equation of motion:

Figure 12. The spatial variation of the plasma temperature behind the shock front for various values of the model parameter n.

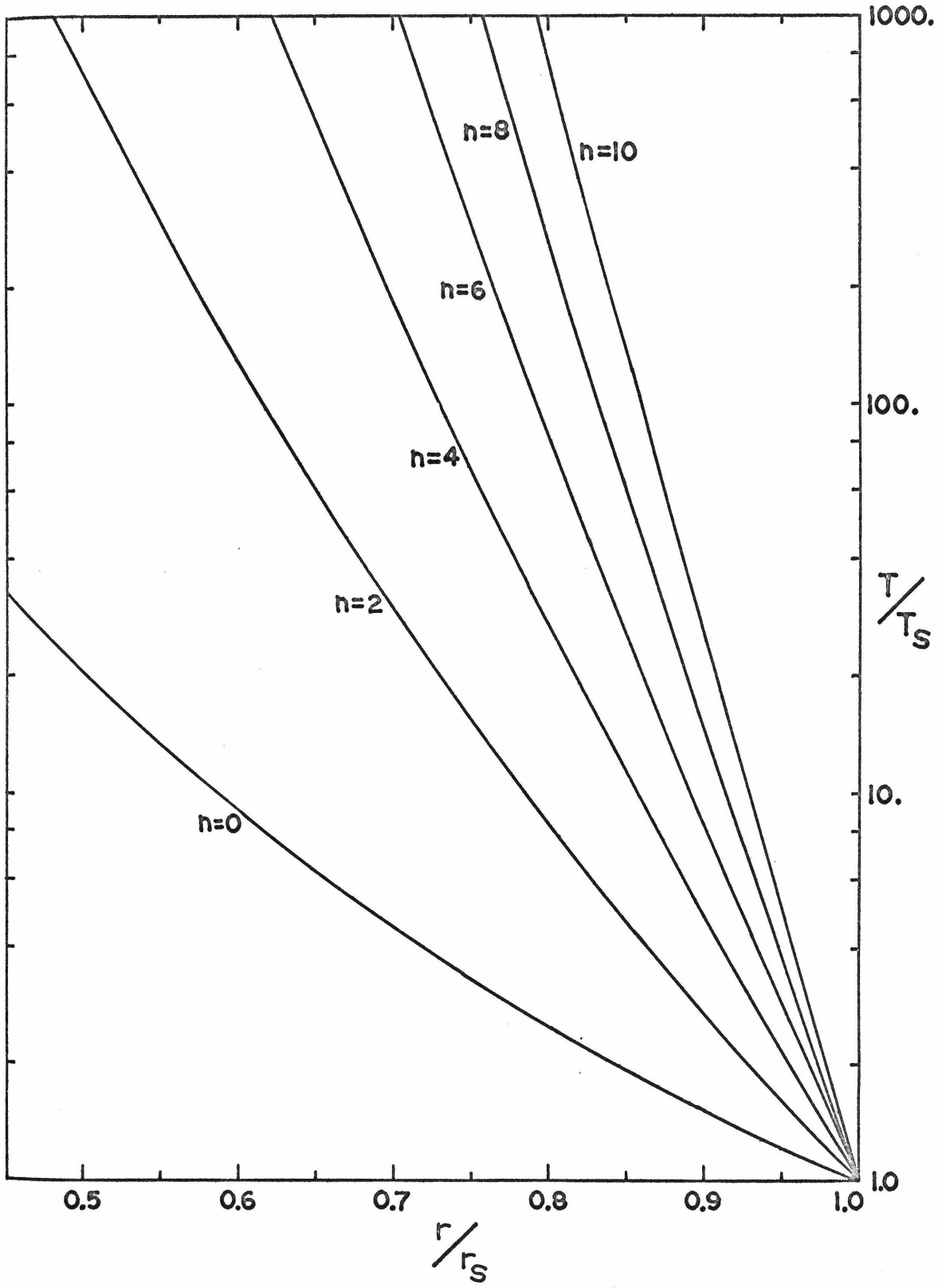

Figure 12

Figure 13. The spatial variation of the plasma density behind the shock front for various values of the model parameter n.

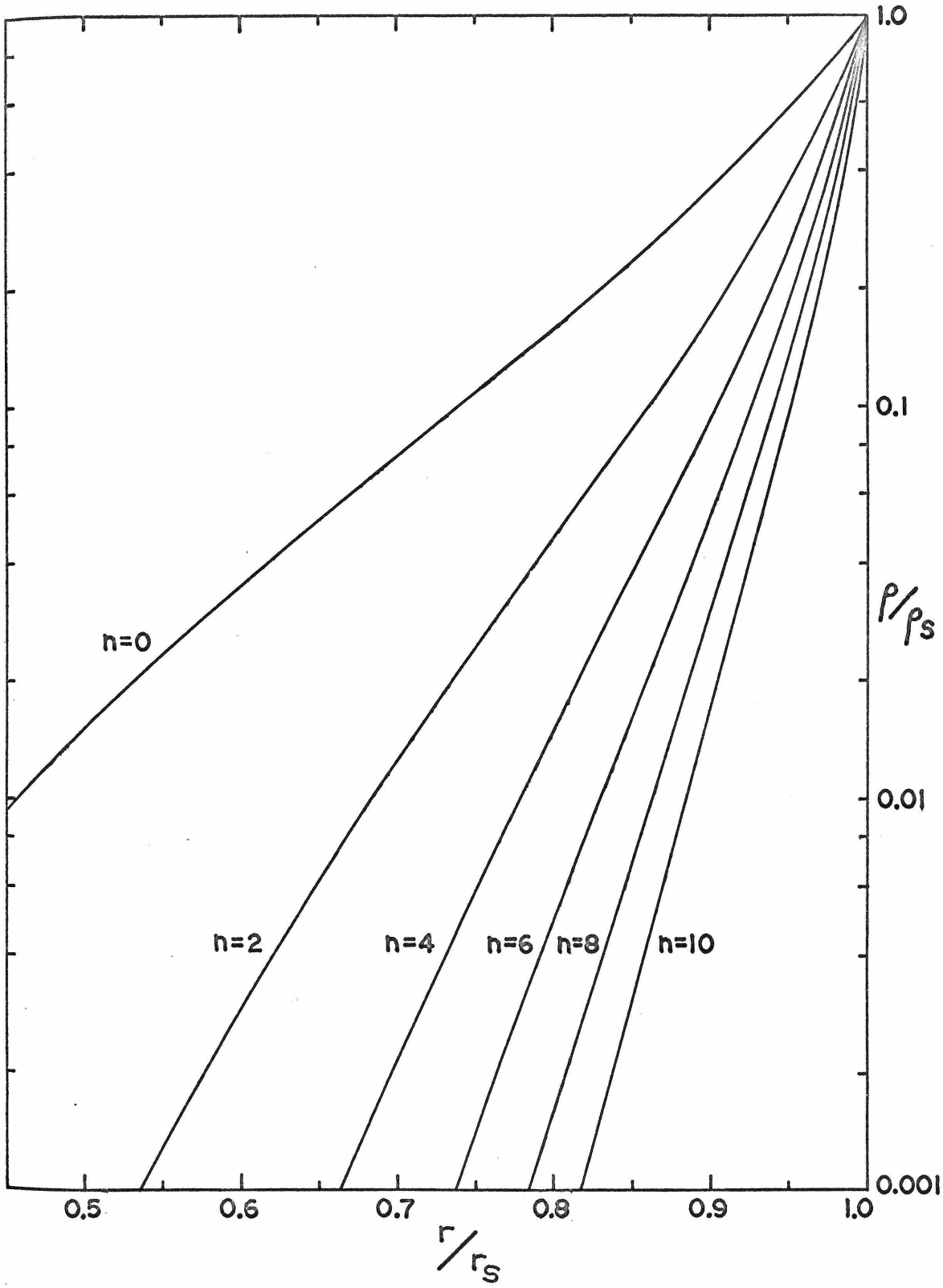

Figure 13

$$r_s = \left(\frac{E_o}{\beta A} \right)^{\frac{1}{5+n}} t^{\frac{2}{5+n}}$$

Here E_o is the energy of the initial explosion involved in mass motions, $A = \rho_o r_o^{-n}$, t is the time since the explosion and β is a constant which depends on the value of n assumed. Figure 14 gives the dependence of β on n.

The velocity, c , of the shock wave is given by

$$c = \frac{dr_s}{dt} = \frac{2}{5+n} \frac{r_s}{t}$$

This velocity is to be distinguished from that of the gas just inside the shock front, v_s . According to the physics of shock fronts these velocities are related by (Sedov, 1959 & Spitzer, 1968)

$$v_s = \frac{2}{\gamma+1} c$$

where γ is the adiabatic index of the gas. γ is assumed to be 5/3 for these calculations, the value for a monatomic gas, hence:

$$v_s = \frac{3}{4} c$$

If the visual filamentary structure is assumed to be embedded in the gas, then the velocity observed for these

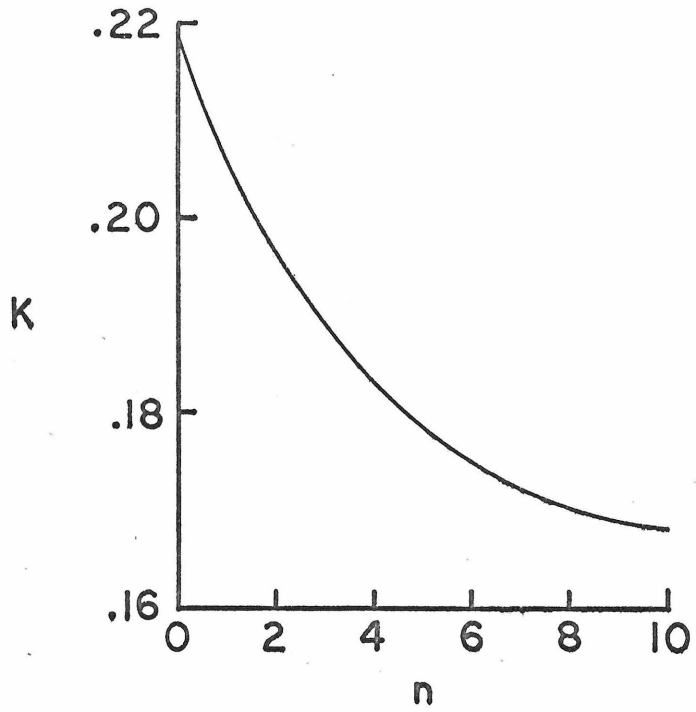

Figure 14. Variation of $K = (5+n)^2\beta/18\pi$ with n. These values of K were calculated from the shock wave solutions shown in figures 12 and 13 according to the prescription given by Sedov (1959).

filaments is that of the gas, v_s . Minkowski (1958) and more recently Doroshenko (1971) have spectroscopically measured the expansion velocity of these filaments to be ≈115 km/sec. The shock wave velocity therefore is ≈150 km/sec.

The pressure and density of the plasma just behind the shock front are given in terms of the density, ρ_o , just ahead of the shock front by (Sedov, 1959 & Spitzer, 1968)

$$\rho_s = \frac{\gamma+1}{\gamma-1} \rho_o = 4\rho_o$$

and

$$p_s = \frac{2}{\gamma+1} \rho_o c^2 = \frac{3}{4} \rho_o c^2$$

From these the temperature can be found:

$$kT_s = \mu \frac{p_s}{\rho_s} = 2\mu \frac{(\gamma-1)}{(\gamma+1)2} c^2$$

where μ is the average mass per particle and k is Boltzmann's constant. Assuming that the gas is 10% (by number) helium and the rest atomic hydrogen, and assuming both constituents are essentially completely ionized then $\mu = 0.61\ m_H$, where m_H is the mass of the hydrogen atom. This also assumes that the electrons and ions come to equilibrium rapidly with respect to the expansion times

(see Heiles, 1964; Spitzer, 1968 and Shklovskii, 1968). If these assumptions hold then,

$$T_s = 0.115 \frac{c^2 m_H}{k}$$

The temperature just inside the shock front is therefore completely determined by the shock velocity c. For the assumed shock velocity of ≈150 km/sec this temperature is ≈310000 ^oK (kT_s = 27 ev).

The discussion immediately above indicates that a model is completely specified by three parameters, ρ_o (or ρ_s), c (or T_s) and n. In the calculations below the value of ρ_o is usually used as a normalizing factor to bring the predictions and observations into agreement. The values of T_s and n are both assumed prior to the calculations. Two models are of primary interest and are developed in some detail below. These will be labeled model (0,216) and model (10, 27) for reference convenience. Model (0,216) is the model suggested but undeveloped by Tucker. It is characterized by a high shock expansion velocity ≈425 km/sec which gives a high shock temperature $T_s = 2.5 \times 10^6$ ^oK (kT_s = 216 ev). This model assumes an initially homogeneous distribution of the interstellar medium, i.e. n = 0.

The other model, (10,27), is an inhomogeneous

model with n = 10. This model assumes a shock velocity equal to that found above to be consistent with the spectroscopically measured filamentary velocity, i.e. 150 km/sec. This gives a shock temperature of $\approx 3.1 \times 10^5$ ^{o}K (kT_s = 27 ev). This model is presented as an approximation to the situation of a shock wave encountering the abrupt boundary of an interstellar cloud or a dust lane at $\approx 0.9\ r_s$. This density distribution is particularly suggested by the visual and x-ray appearances of the Cygnus Loop in the region of NGC 6992-5.

Table 8 summarizes the observational properties of the Cygnus Loop used in the calculations. Table 9 summarizes the parameter values assumed for models (0,216) and (10,27). Note that the reference nomenclature for these two models is (n, kT_s).

TABLE 8

SUMMARY OF OBSERVATIONAL PROPERTIES OF CYGNUS LOOP

Distance	770 pc
Angular Size	160'
Shock Front Diameter	40 pc
Diametral Expansion Rate	0.06"/yr
Visual Expansion Velocity	115 km/sec

TABLE 9

PARAMETERS ASSUMED IN TWO PRIMARY MODELS

	Model (0,216)	Model (10,27)
Initial Density Dependence	homogeneous	inhomogeneous
Model Parameter n	0	10
Shock Velocity, c	430 km/sec	150 km/sec
Shock Temperature, T_s	2.1×10^6 °K	3.1×10^5 °K
kT_s	216 ev	27 ev

In the following calculations the derived properties are usually depicted graphically in the accompanying figures. More models than these two primary models are usually shown in these figures. These additional models are included to illustrate how a particular functional dependence progresses. The discussion in the text will be primarily concerned with the two models detailed in Table 9.

D. Spectrum Calculation

For calculation of the spectrum expected from the whole Cygnus Loop the emission from each unit volume of plasma is approximated by the expression for free-free (or thermal bremsstrahlung) radiation:

$$L_{ff}(E) = 7.0 \times 10^{-11} \frac{\rho^2}{E(kT)^{\frac{1}{2}}} e^{-E/kT} \quad \text{photons/sec-kev-cm}^3$$

where both E and kT are in ev and ρ is the density of the gas in units of m_H , the mass of the hydrogen atom per cm^3. To obtain this formula the same assumption about the interstellar gas was made as above, i.e. 90% (by number) hydrogen and 10% helium. Also the gaunt factor has been set equal to 1.

The total x-ray emission at energy E from the entire volume within the shock front is therefore given by

$$\int_0^{r_s} L_{ff}(E) 4\pi r^2 dr$$

This assumes that the absorption in the Cygnus Loop itself is negligible for the observed x-rays. Substituting the expression for L_{ff} from above leads to

$$8.8 \times 10^{-10} \frac{\rho_s^2 r_s^3}{E} \int_0^{r_s} \frac{e^{-E/kT}}{(kT)^{\frac{1}{2}}} \left(\frac{\rho}{\rho_s}\right)^2 \left(\frac{r}{r_s}\right)^2 \frac{dr}{r_s}$$

The integration proceeds using the values given by the solutions shown in figures 12 and 13 once a shock temperature or equivalently a shock velocity is assumed. The value of ρ_s is left to be determined so as to bring the intensity predicted into agreement with the observations.

The spectra obtained through numerical integration

of this equation are shown in figures 15, 16, and 17. Figure 15 shows the effect on the spectrum of varying the power n while holding the shock temperature fixed. Figures 16 and 17 show how the spectrum depends on the assumed shock temperature (velocity) for n = 0 (the homogeneous case) and n = 10 respectively.

These composite spectra need to be described in terms of the simple spectral functions used in

so that they can be compared to the experimental results. These spectral functions were:

1) Thermal Bremsstrahlung Spectrum

$$\frac{dN}{dE} = \frac{A}{E} \exp\left(\frac{-E}{kT}\right) \qquad \text{photons/sec-kev}$$

2) Power Law Spectrum

$$\frac{dN}{dE} = AE^{-\alpha} \qquad \text{photons/sec-kev}$$

In general the composite spectra obtained for low shock velocities (temperatures) are well described by the power law spectral form and as the shock velocity (temperature) is increased these composite spectra become better approximated by the thermal bremsstrahlung spectral form. Model (0,216) is best fit by the thermal bremsstrahlung form with kT = 295 ev. The fact that the

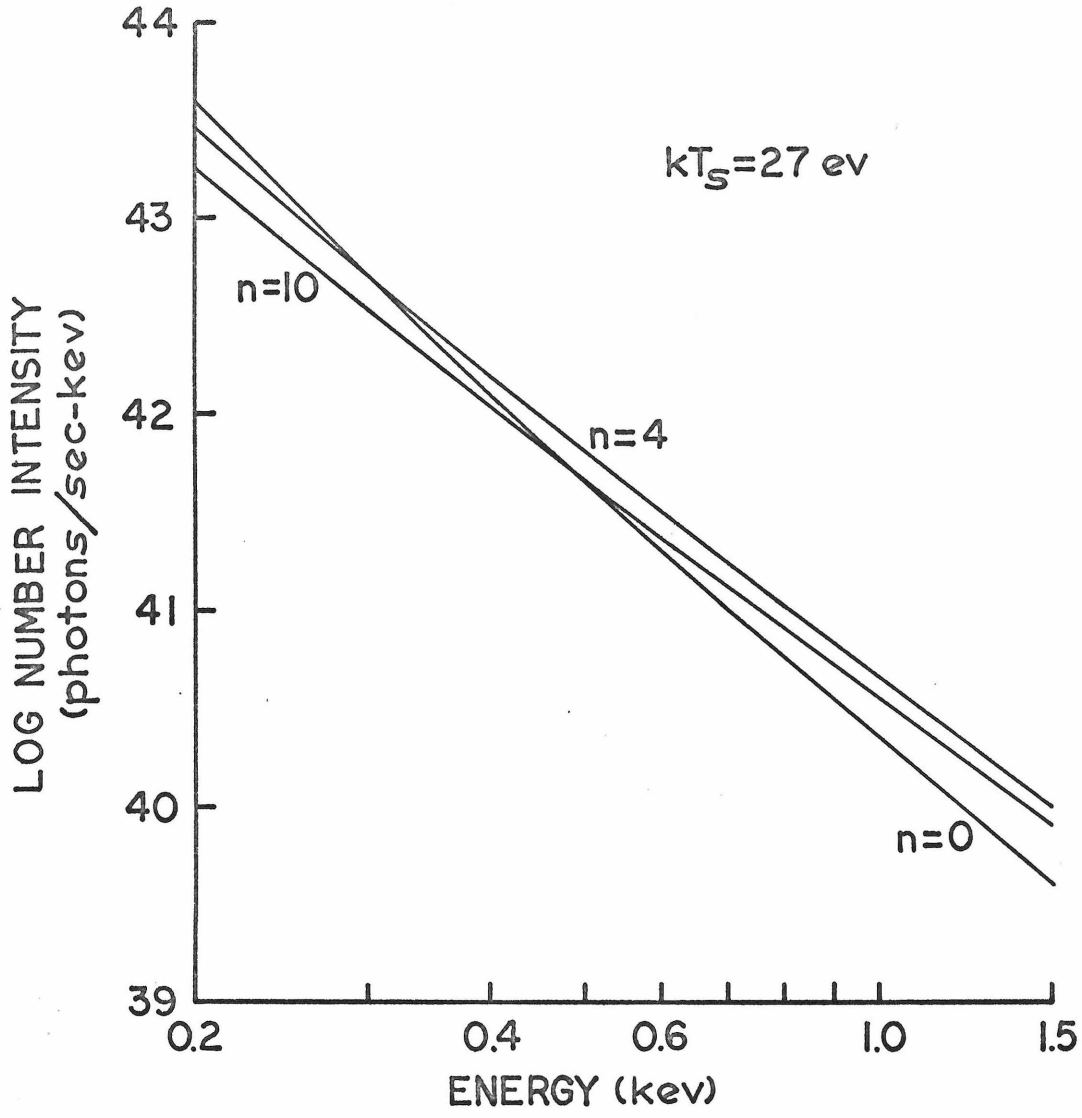

Figure 15. Calculated x-ray spectra of Cygnus Loop for three values of the model parameter n. The curves shown in this figure are for an assumed shock temperature, kT_s = 27 ev, and an assumed density ρ_s = 1.0 m_H/cm^3 . The curves are proportional to ρ_s^2 .

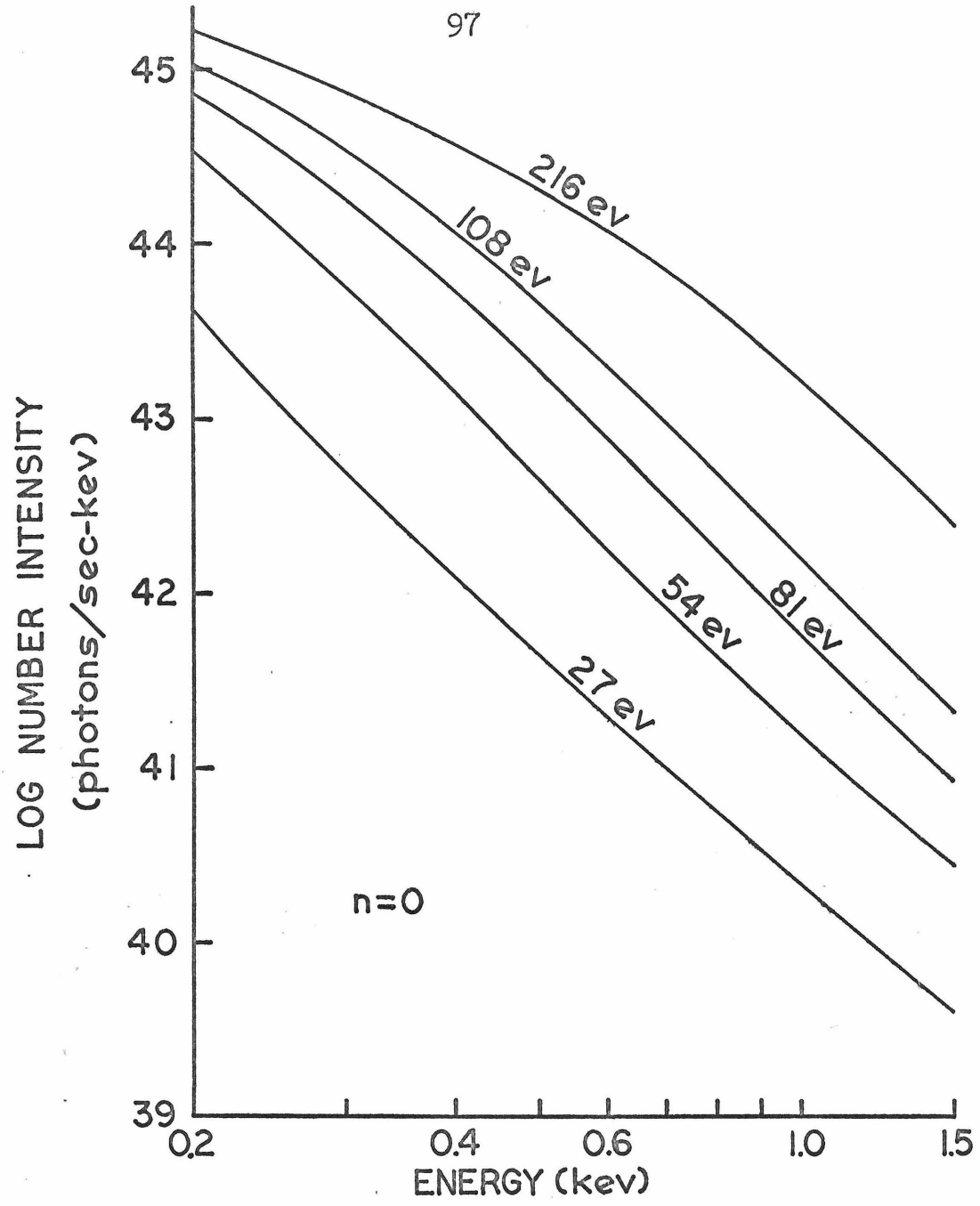

Figure 16. Calculated x-ray spectra of Cygnus Loop for the homogeneous model, n = 0, with various values of the shock temperature, T_s. The curves are labeled with the assumed value of T_s. The density, ρ_s, has been assumed to be 1.0 m_H/cm^3 in these curves. The curves are proportional to ρ_s^2.

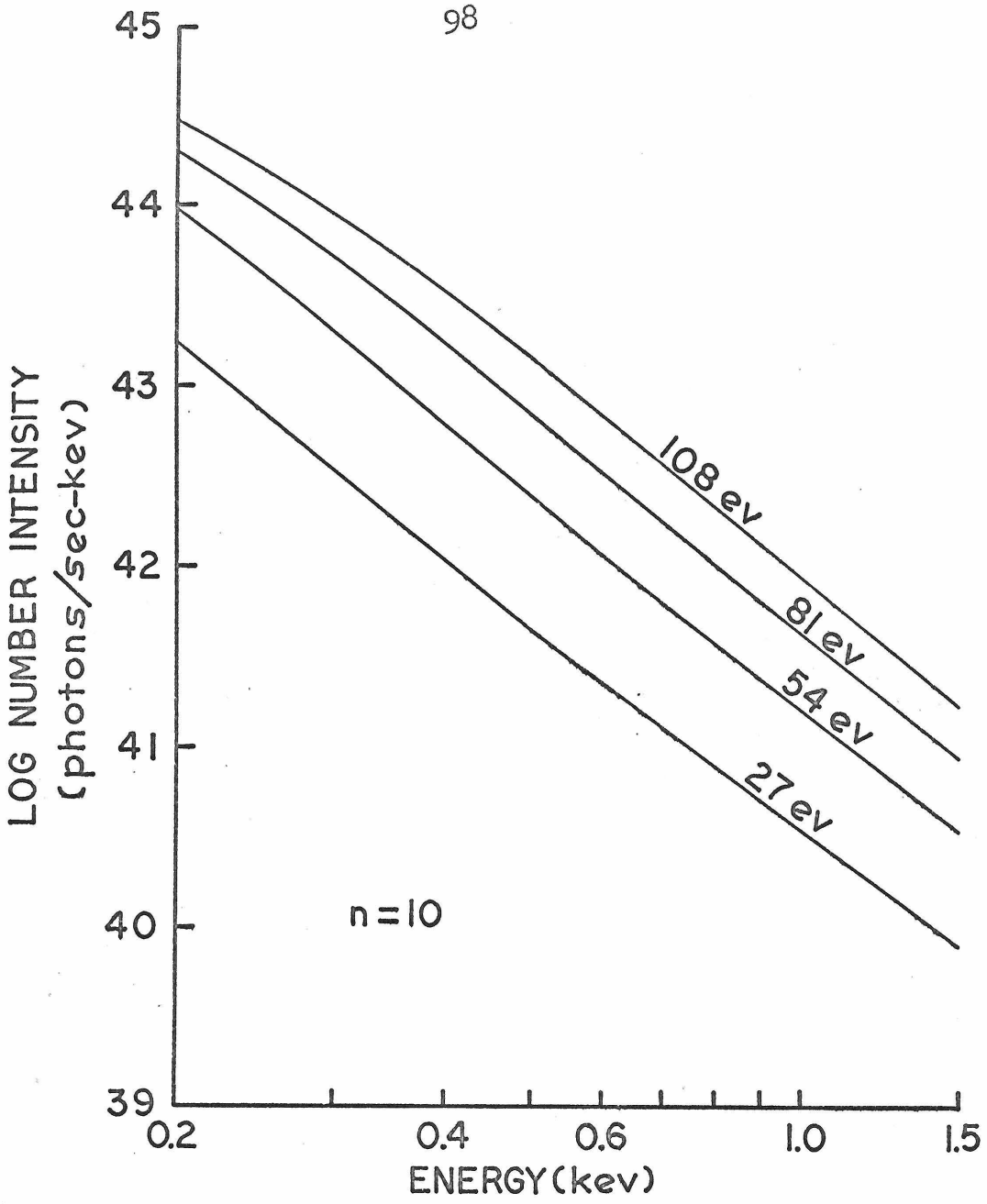

Figure 17. Calculated x-ray spectra of Cygnus Loop for the inhomogeneous model, n = 10, with various values of the shock temperature, T_s. The curves are labeled with the assumed value of T_s. The density, ρ_s, has been assumed to be 1.0 m_H/cm^3 in these curves. The curves are proportional to ρ_s^2.

equivalent temperature found for the composite spectra, 295 ev, is higher than the shock front temperature, 216 ev, is noteworthy. Model (10,27) is best fit by the power law form with $\alpha \approx 3.9$. These spectral parameters are to be compared with the values found from the x-ray observations of kT = 230 ev and $\alpha \approx 4.4$. The agreement between predictions and observations must be considered satisfactory especially in view of the uncertainties involved in these composite spectral calculations. The poor knowledge of the anisotropies present in the Cygnus Loop does not permit a more precise calculation of these composite spectra even if a more precise approximation to the x-ray emission from a plasma were utilized.

Comparison of the intensity levels of these composite spectra to those of the spectra derived from the experimental observations will give the value of ρ_o. The experimental observations gave 5.2×10^{45} photons/sec-kev @ 0.23 kev for the thermal bremsstrahlung model. The composite spectrum for the model (10,27) gives $1.6 \times 10^{43}\ \rho_o^2$ photons/sec-kev @ 0.23 kev. Therefore $\rho_o = 18\ m_H/cm^3$ to give consistency between the observations and calculations. For model (0,216) the composite spectrum gives $2.1 \times 10^{45}\ \rho_o^2$ photons/sec-kev @ 0.23 kev which implies $\rho_o = 1.6\ m_H/cm^3$. These results are

summarized in Table 10.

TABLE 10

SPECTRAL FEATURES OF TWO PRIMARY MODELS

	Model (0,216)	Model (10,27)
Spectral Shape	thermal brems.	power law
Spectral Parameters	kT = 295 ev	$\alpha \approx 3.9$
Density, ρ_o, Needed for Consistency with Observations	1.6 m_H/cm^3	18 m_H/cm^3

E. Surface Brightness Calculations

The solutions given by Sedov can also be used to calculate the expected variation of the surface brightness with radius. The surface brightness spectrum is first calculated as a function of radius and then this is integrated over energies greater than 0.15 kev to give the integrated surface brightness as a function of radius. The actual calculation is analogous to that done above for the composite spectra. The volume integral there becomes here an integral through the assumed spherical volume over a unit area at a radius r. This integral is written in terms of the quantities available from the solutions by Sedov and numerically evaluated. Again a factor of ρ_s^2 is left to be determined by comparing the observations and the predictions.

Figures 18 and 19 show the dependence of the relative surface brightness at energy E on radius. From these figures it can be seen that the higher the energy of x-rays the further inward from the shock front is the peak in the surface brightness. Figure 18 shows that when the shock temperature is increased the position of the maximum surface brightness at a given energy moves closer to the shock front. Figure 19 shows that steepening the initial density dependence on radius, i.e. increasing n, increases the maximum surface brightness to surface brightness at r = 0 ratio while it also moves the position of maximum surface brightness toward the shock front.

This radial dependence of the surface brightness spectrum is potentially an observable phenomenum. Since the Loop is 160' in diameter, 1/10 of the radius is 8'. This resolution will be easily obtainable with future focusing x-ray telescopes. A detector with resolution of 8' would be able to detect spectral variations if model (0,216) is valid and not if model (10,27) is more applicable. This is made more clear in figures 20 and 21. These show the spectrum to be seen at selected radii for both models. Comparison of these two figures shows that the shape of the spectrum is essentially independent of radius for r less than $\approx 0.88\ r_s$ for model (10,27)

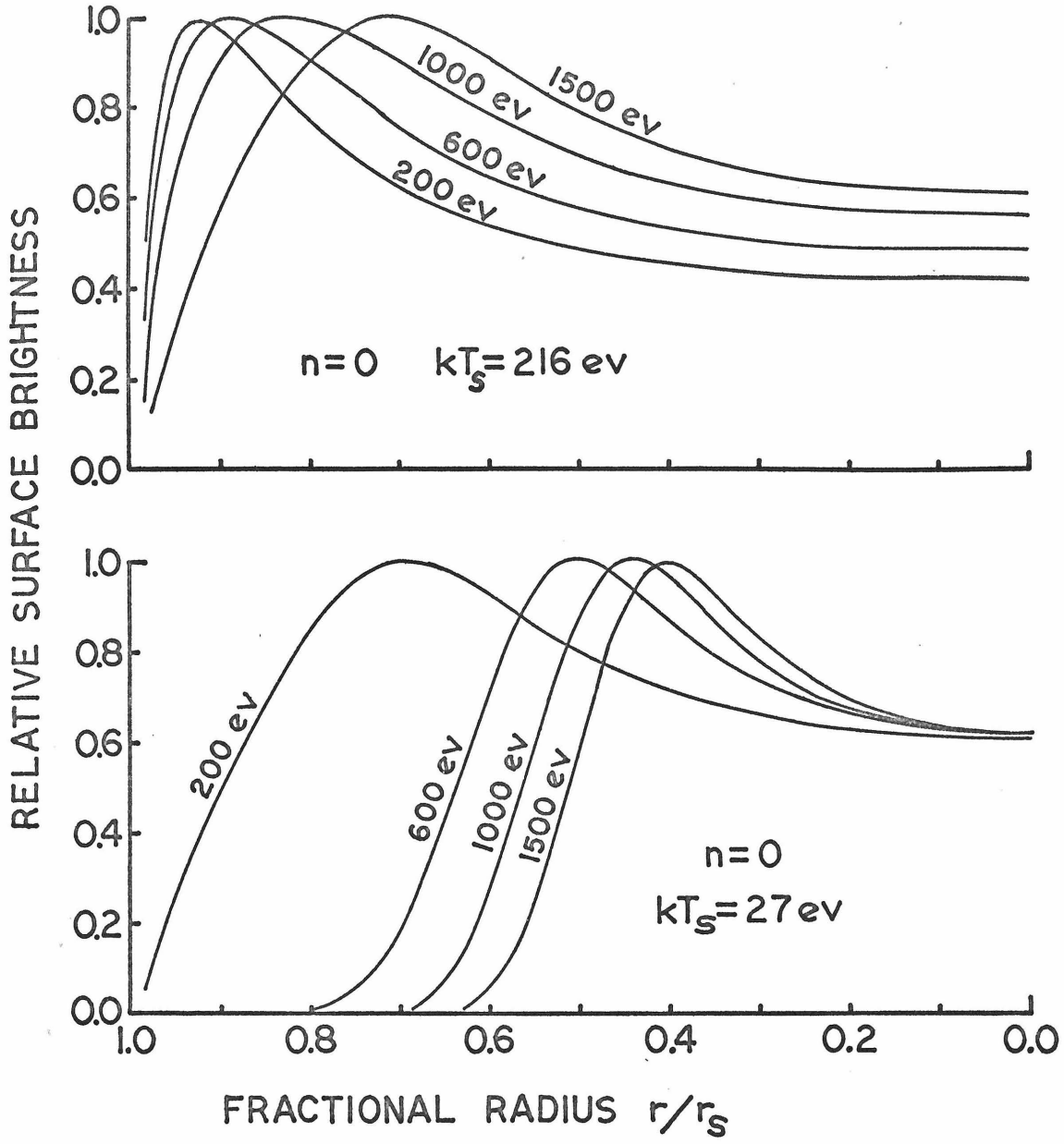

Figure 18. The radial dependence of the surface brightness of the Cygnus Loop calculated at four selected energies for the homogeneous model with two values of the assumed shock temperature. The curves are labeled with the energy at which the surface brightness was calculated. All of the curves have been normalized to peak at 1.0 .

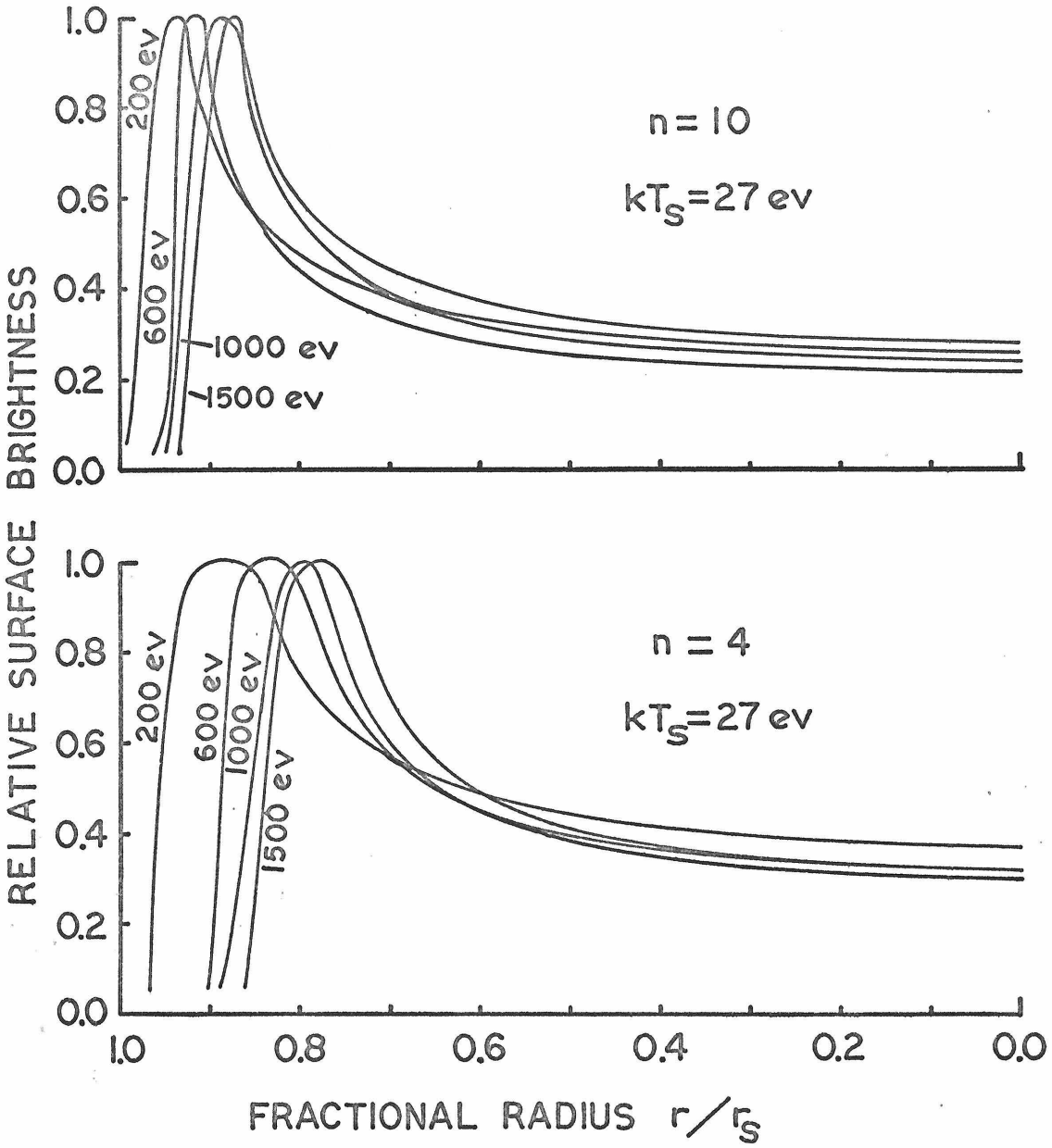

Figure 19. The radial dependence of the surface brightness of the Cygnus Loop calculated at four selected energies for two inhomogeneous models, n = 4 and n = 10, with an assumed shock temperature of kT_s = 27 ev. The curves are labeled with the energy at which the surface brightness was calculated. All the curves have been normalized to peak at 1.0 .

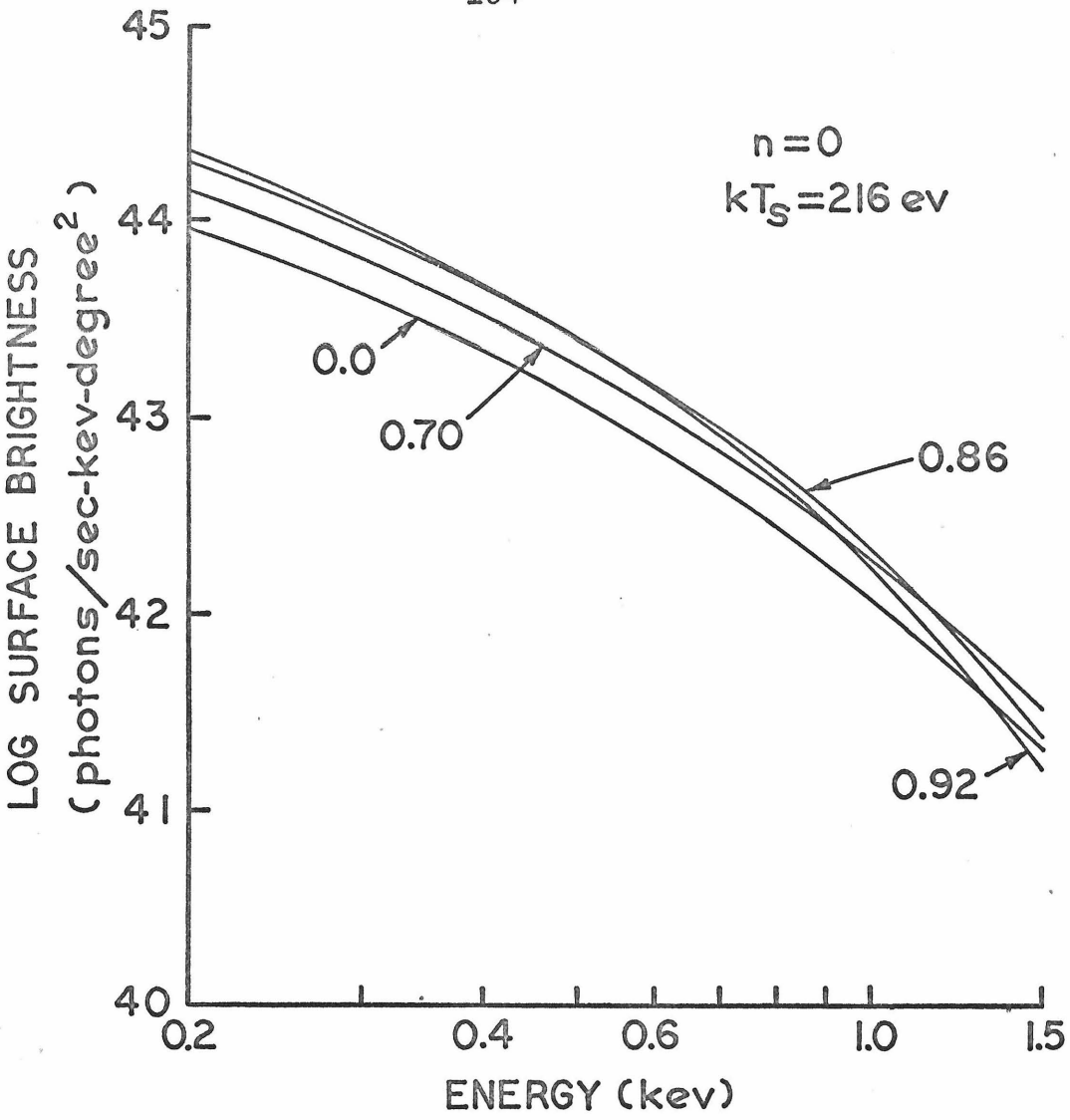

Figure 20. Calculated x-ray spectra of the surface brightness of the Cygnus Loop at various radii. The spectra shown are for model (0,216). Each spectrum is labeled with the appropriate value of the radius r/r_s. The spectra are proportional to ρ_s^2 and are shown for an assumed density $\rho_s = 1.0\ m_H/cm^3$.

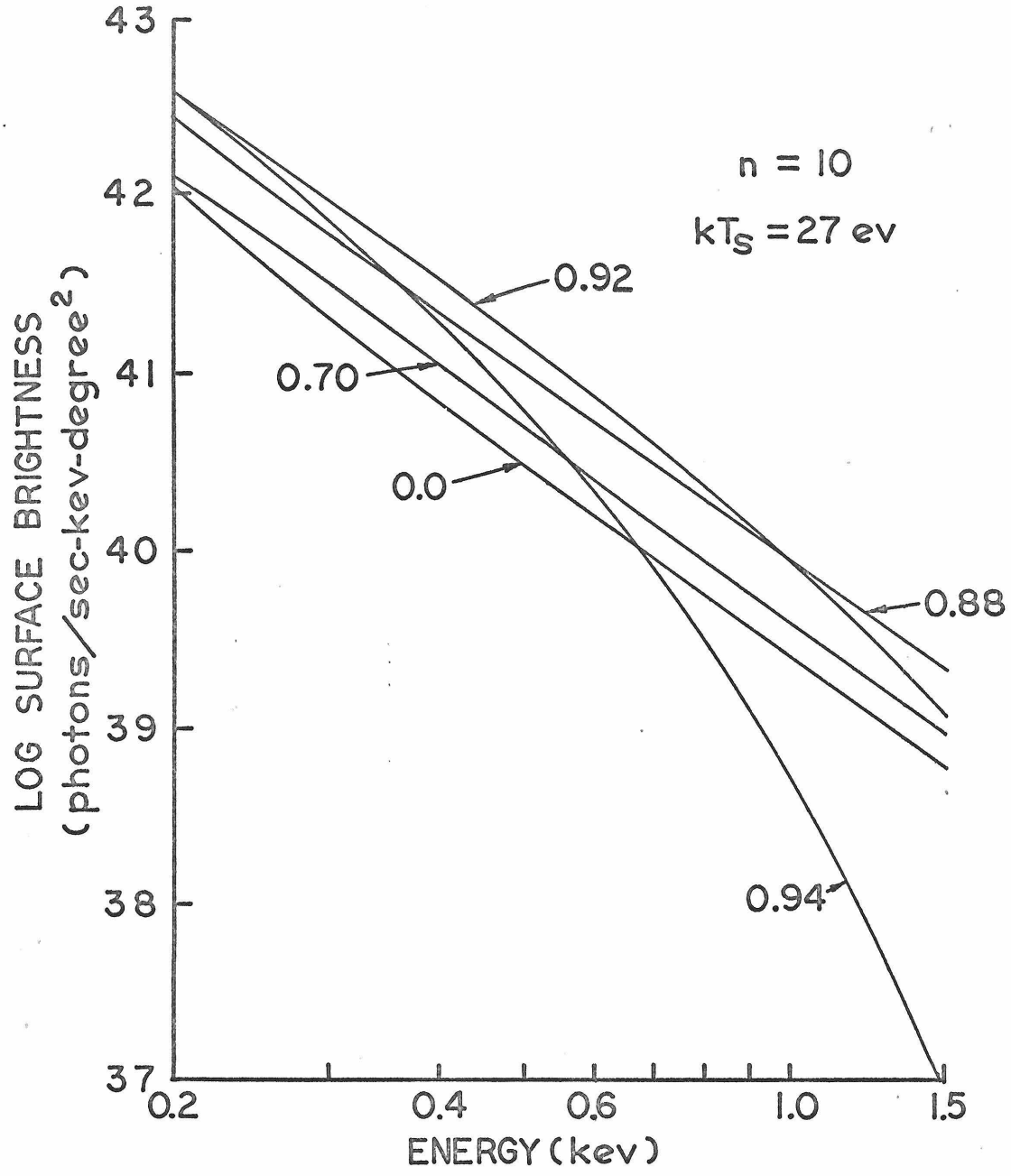

Figure 21. Calculated x-ray spectra of the surface brightness of the Cygnus Loop at various radii. The spectra shown are for model (10,27). Each spectrum is labeled with the appropriate value of the radius r/r_s. The spectra are proportional to ρ_s^2 and are shown for an assumed density $\rho_s = 1.0\ m_H/cm^3$.

and remains dependent on radius down to $r \approx 0.70\ r_s$ for model (0,216). These spectral variations are potentially observable and furnish a test between the two models given here.

The integrated surface brightness above 0.15 kev is shown in figure 22 as a function of radius. These curves are again for an isotropic distribution, i.e. the Cygnus Loop is assumed to be spherically complete. Comparison of the curves in figure 22 with those in figures 18 and 19 shows that the radial dependence of the total emissivity and the radial dependence of the relative surface brightness at a particular energy vary with the shock temperature and the model number n in entirely analogous manners.

The dependencies of the surface brightness on radius shown in figure 22 are to be compared with the x-ray map given in figure 3. The predicted peaking of the emission toward the edges of the Loop is clearly visible in the observed map. Also the regions just inside the edge of the Loop display some emission as the curves of figure 22 indicate they should. However the ratio of the emission from the edge of the Loop to the emission just inside the edge of the Loop is too high in the observations. As an example, looking at NGC 6992-5 the average emission observed along the edge is 4.9×10^{35}

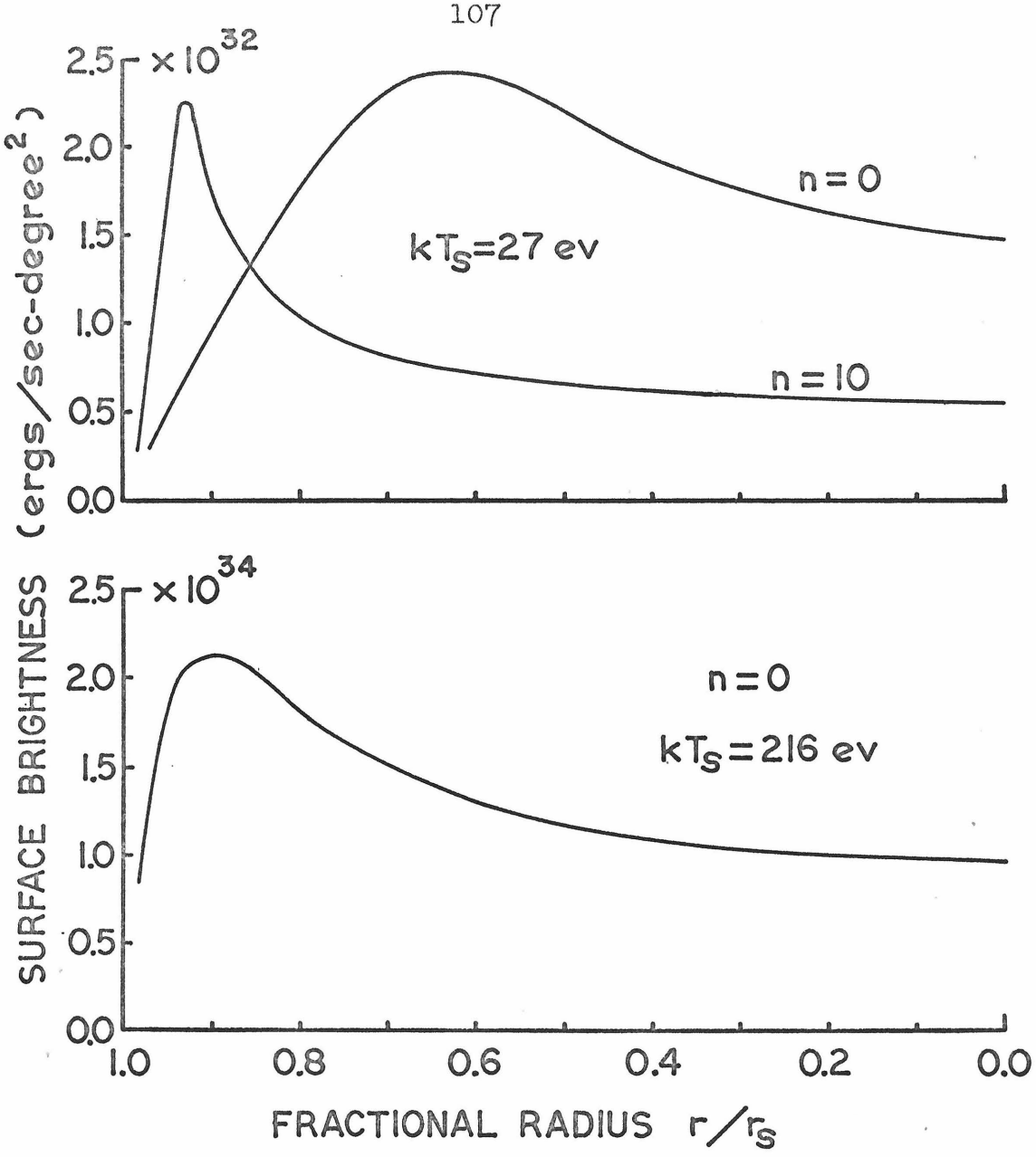

Figure 22. The radial dependence of the calculated surface brightness, 0.15 to 1.55 kev, of the Cygnus Loop for several models. The curves are proportional to ρ_s^2 and are shown for an assumed density $\rho_s = 1.0\ m_H/cm^3$.

ergs/sec-degree^2 whereas the average emission observed from the next set of resolution elements inward along the radius is 2.3×10^{35} ergs/sec-degree^2 . Thus the edge is $\approx$2.1 times as bright as the region just inside the edge. An estimate of what the curves of figure predict for this ratio is obtained by averaging the surface brightness from 0.8 r_s to 1.0 r_s and comparing this to the average surface brightness from 0.5 r_s to 0.8 r_s . Clearly, as advertised in the introductory discussion above, the homogeneous model, n = 0, with kT_s = 27 ev does not provide an adequate description of the observations. Model (10,27) is the more peaked of the two primary models. The ratios for these two models are: 1.7 for model (10,27) and 1.3 for model (0,216). In light of the relatively large errors associated with the x-ray map the value of the ratio found for model (10,27) is probably consistent with the value observed for NGC 6992-5 whereas the value found for model (0,216) probably is not consistent. The fact that the ratio for model (10,27) falls below the observed value may imply that in actuality the shock velocity is higher or the density dependence more abrupt than those assumed for this model. Table 11 summarizes the surface brightness predictions for both models.

TABLE 20

SURFACE BRIGHTNESS FEATURES OF TWO PRIMARY MODELS

	Model (0,216)	Model (10,27)
Spectral Shape is Dependent on radius outside	0.70 r_s	0.88 r_s
Edge to Interior Surface Brightness Ratio (Observations give 2.1)	1.3	1.7

F. Density Variations Implied by Observed Intensity Variations

The value of ρ_o, the density just beyond the shock wave, can also be found from these observations. Clearly either ρ_o is anisotropic and/or the model does not hold equally well in all directions. For NGC 6992-5, the predicted intensity for the edge of the Loop according to model (0,216) is $3.1 \times 10^{35} \rho_o^2$ ergs/sec-degree^2. Comparing this to the observed value, 4.9×10^{35} ergs/sec-degree^2, yields a value of $\rho_o = 1.3\ m_H/cm^3$ for consistency. For model (19,27) the predicted value $2.3 \times 10^{33} \rho_o^2$ ergs/sec-degree^2 requires $\rho_o = 15\ m_H/cm^3$ for consistency. This same calculation was done for the emission from each segment of the edge of the Loop to give the values shown in figure 23. The densities necessary to make both models consistent with the

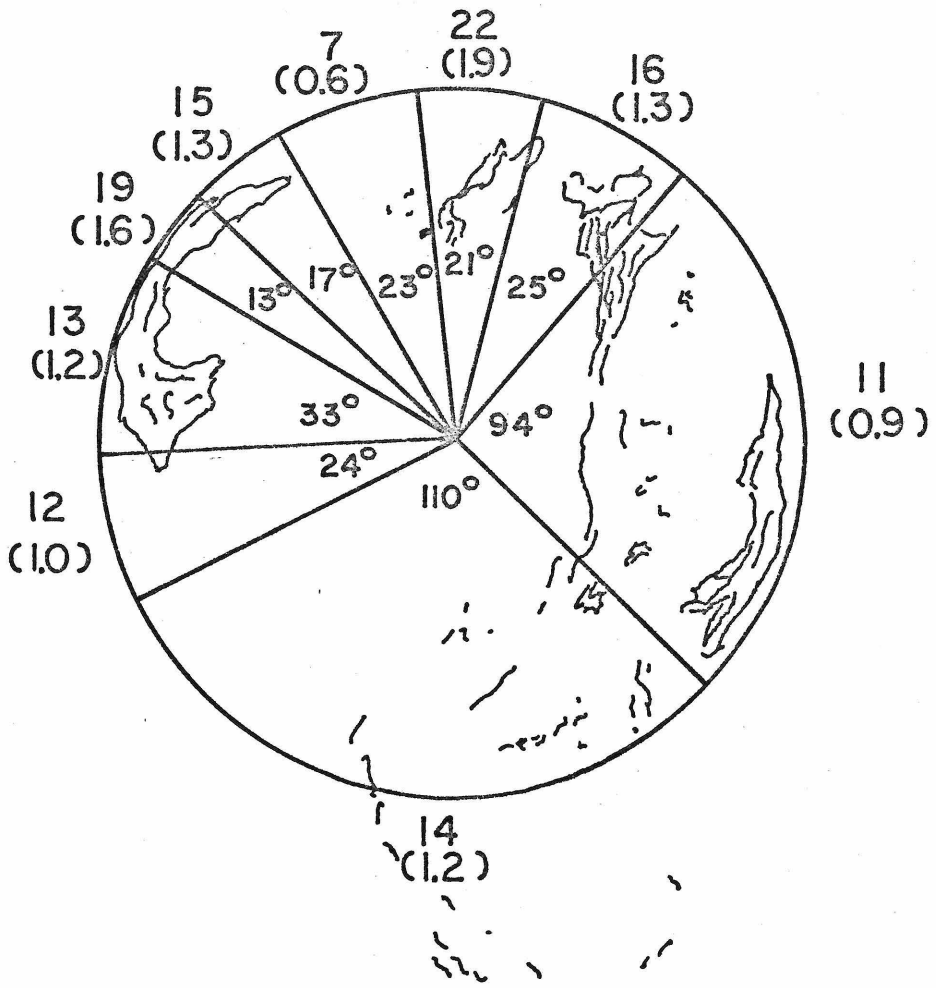

Figure 23. The interstellar density just beyond the edge of the Cygnus Loop according to the models developed in the text. The Loop is segmented so that the x-ray intensity of the edge of the Loop in each segment is constant according to the x-ray map in figure 3. The densities are given in units of m_H/cm^3. The top value for each segment is the density obtained from model (10,27) and the lower value (in parenthesis) is the density obtained from model (0,216). For reference purposes the density map is superimposed on a crude sketch of the Hα emission from the Loop.

observations are given in this figure.

The assumption upon which this density map is based is that the observed variations in the x-ray intensity around the edge of the Loop are due to density variations rather than shock temperature variations. These density variations will result in pressure variations around the edge of the Loop. If these pressure variations cause equalization of the density variations faster than the shock wave produces them then no intensity variations should be apparent. The velocity with which these pressure variations will be equalized is the sound velocity, if the mean free path of the ions is small compared to other characteristic dimensions. The mean free path, d, for the ions is given by $d \approx (N\sigma)^{-1}$, where N is the number density and σ is the interaction cross-section, σ is at least as large as the geometrical cross-section, $\approx 10^{-16} cm^2$. N is of order 0.1 cm^{-3} so $d \approx 1/30$ pc. Hence the plasma inside the Cygnus Loop will exhibit mass motions and will equalize pressures at the local speed of sound. This speed s, is given by:

$$s = (\gamma p/\rho)^{\frac{1}{2}}$$

where p is the pressure, ρ the density and γ the adiabatic index of the gas. Expressing the pressure in terms of the density and temperature T of the gas gives:

$$s = (\gamma kT/m_H)^{\frac{1}{2}} \simeq 1.25 \times 10^{-5} \sqrt{kT} \quad \text{pc/yr}$$

where kT is in units of ev. This velocity must be large compared to the shock velocity $c = 1.5 \times 10^{-4}$ pc/yr in order that pressure equilibrium can be achieved. A further complication arises in that there is a mass motion of the gas inside the shock front toward the shock front which reduces the radial sound velocity. The velocity of this mass motion is 75% of the shock velocity near the shock front and decreases with decreasing radius. Roughly speaking, the velocity of sound must therefore be at least twice the shock front's velocity in order that pressure equilibrium can be achieved. This is equivalent to requiring that kT > 580 ev. For model (0,216) this temperature is achieved at $\approx 0.79\ r_s$. For model (10,27) this temperature is reached at $\approx 0.91\ r_s$. Inside these radii, according to the models employed here, the pressure variations due to density variations at the shock front will equalize faster than they are established. Complete equilibrium will require a non-negligible amount of time but certainly should be achieved inside $r \approx 0.5\ r_s$. It is therefore reasonable to hypothesize that the density variations shown in figure 23 are responsible for the

observed intensity variations around the edge of the Loop.

These density variations, if present for a sufficiently long time, will cause a distortion away from a spherical shock front by retarding some regions of the shock front more than other regions. From above, the radius of the shock front is given by:

$$r_s = \left(\frac{E_o r_o^n}{\beta \rho_o}\right)^{\frac{1}{5+n}} t^{\frac{2}{5+n}}$$

If ρ_o is determined for the material just beyond the shock front then $r_o = r_s$ regardless of ρ_o. The expression for r_s then becomes:

$$r_s = \left(\frac{E_o}{\beta}\right)^{1/5} t^{2/5} \left(\frac{1}{\rho_o}\right)^{1/5}$$

Thus r_s is only nominally dependent on ρ_o. The ratio of the maximum density to the minimum density shown in figure 23 is ≈ 3.1. This density variation, if it had existed throughout the evolution of the Cygnus Loop, would have caused a discrepancy in the present radii of only $\approx 25\%$ between the regions of high and low density. This discrepancy, even if present, would not have been detected by this experiment. However future focusing x-ray telescopes will be able to detect variations of this order without difficulty.

G. Mass of X-ray Emitting Region

The total mass responsible for the x-ray emission can be determined in two ways. The first uses the densities given in figure 23 to determine an average density for the interstellar material just beyond the shock front and from this density, using the initial density distribution's radial dependence, calculates the total mass of interstellar gas inside the Loop. Clearly this is an overestimation of the mass emitting x-rays. The spectral approximation to thermal bremsstrahlung used in these models will give an underestimation of the x-ray emission to be expected from a hot plasma because it ignores line emission and radiative recombination. Since the plasma will in actuality be a better x-ray emitter than assumed here the total mass required to give the observed x-ray intensity found by this method will be an overestimation. Also this first method of calculating this mass assumes that all the mass inside the shock front emits x-rays. Nonetheless, the calculation gives a useful upper limit.

The initial density distribution for a model with power n is $\rho_i = \rho_o(r_i/r_o)^n$. Hence, knowing ρ_o at $r_o = r_s$ the amount of matter initially inside r_s can be easily calculated. The value of ρ_o was obtained by

averaging the square of the densities given in figure 23 weighted according to the angle for which they are applicable. The values of ρ_o and M, the x-ray emitting mass, obtained for model (0,216) were respectively 1.2 m_H/cm^3 and 1200 $M_\odot$. The same values obtained for model (10,27) were 13.5 m_H/cm^3 and 3000 $M_\odot$.

The other method of estimating the mass makes use of the expression obtained at the end of section V:

$$\int \frac{\rho^2}{T}\, dV = 1.6 \times 10^{52} \quad cm^{-3}\ {}^oK^{-1}\ m_H^2$$

Reexpressing this in terms of the quantities available from Sedov's solutions and using the conditions on the shock front leads to

$$4\pi \int_0^{r_1} \left(\frac{\rho}{\rho_s}\right)^2 \frac{T_s}{T} \left(\frac{r}{r_s}\right)^2 \frac{dr}{r_s} = \frac{T_s}{\rho_o^2 r_s^3}\ 1.0 \times 10^{51}$$

The upper limit of integration, r_1 , was chosen so as to include only those plasmas which would emit a significant amount of x-radiation above 0.2 kev, i.e. only those plasmas with $kT \gtrsim 0.1$ kev. The integral was evaluated numerically for each model and values of ρ_o and M were obtained. Table 12 gives the values of r_1 , ρ_o and M for both models.

TABLE 12

PARAMETERS USED TO OBTAIN X-RAY EMITTING MASS FOR TWO PRIMARY MODELS

	Model (0,216)	Model(10,27)
r_1 , the upper limit of integration	1.0 r_s	0.97 r_s
ρ_o (m_H/cm^3)	0.16	0.73
$M/M_\odot$	160	180

The agreement between the values of M found by these two models is remarkable. A priori, the inhomogeneous model (10,27) might be thought to be much less efficient than the homogeneous model (0,216) because of the higher shock temperature of the latter. However the dependence of the emission on ρ^2 and the high radial dependence of the initial density distribution for model (10,27) precisely compensate for its lower temperature.

These masses are more accurate than those obtained above but these probably are slight underestimations. They are based on the assumption that all of the x-rays which this mass emits have energies above 0.2 kev. This assumption was made in order to equate the total observed luminosity to the calculated luminosity.

Since some of the luminosity of the source is actually not observed because it is radiated below 0.2 kev the calculated luminosity should be increased in order to compensate for this. Hence the x-ray emitting mass is underestimated by this calculation.

H. Line Emission Calculation

This experiment's observation of line emission still needs to be reconciled with these shock wave models. From detailed calculations of the x-radiation expected from a hot plasma done by Tucker et al (1971) intense line emission from collisionally excited multiply-ionized oxygen atoms is expected to be present if the plasma temperature is between 1.0 and 4.0 x 10^6 ^oK. These temperatures are seen to occur in a specific range of radii according to the above models. This will result in the surface brightness in these lines peaking very strongly at these radii. Outside these radii these lines will not be present and inside, the surface brightness in these lines will be low.

The total line intensity predicted for each of these two models is obtained from the integral:

$$\int_{r_1}^{r_2} L_{1e}(E,T)\, \rho^2\, dV$$

where $L_{le}(E,T)\,\rho^2$ is the power emitted in line emission at energy E from a plasma at temperature T as given by Tucker et al (1971) and corrected for the interstellar abundance of oxygen given by Brown and Gould (1970). The limits of integration, r_1 and r_2, are given below in Table 22. The function $L_{le}(E,T)$ was approximated by three lines, one at 561 ev, another at 577 ev and the third at 652 ev. There are other lines between 0.53 and 0.69 kev but these emit less than 20% of the power in the above lines. Expressing the integrand in terms of the quantities obtained from Sedov's solutions, the integral becomes:

$$64\pi r_s^3 \rho_o^2 \int_{r_1}^{r_2} \left(\frac{\rho}{\rho_s}\right)^2 \left(\frac{r}{r_s}\right)^2 \left[L_{le}(0.56,T)+L_{le}(0.58,T)+L_{le}(0.65,T)\right] \frac{dr}{r_s}$$

The integration was carried out numerically. The value of ρ_o was taken from Table 12. The results of this integration are given in Table 13. The observational results found above from the filtered measurements of the Cygnus Loop depend on the energy assumed for the line emission (see section IV). This calculation can be used to give an estimation of the percentage of the number flux at 0.65 kev. This percentage was used to

obtain the correct admixture of the observational results to be compared to the predicted results. These observational results are given also in Table 13.

TABLE 13

CALCULATED LINE EMISSION FROM THE CYGNUS LOOP

	Model(0,216)	Model(10,27)
Range of Integration r_1 to r_2	0.91 r_s to 1.0 r_s	0.92 r_s to 0.97 r_s
Predicted Line Emission Between 0.53 and 0.69 kev (photons/cm^2-sec)	35	5.0
Percentage of Predicted Line Emission in 0.65 kev line	40%	11%
Observational Results (photons/cm^2-sec)	5 ± 2	9 ± 4

As Table 13 shows, the prediction of model (10,27) is consistent with the observed line emission. However the factor of 7 discrepancy between the predicted and the observed values for model (0,216) is beyond the inaccuracies involved in the calculation.

I. Age of Cygnus Loop

From the equation for the shock velocity given above:

$$t = \frac{2}{5+n} \frac{r_s}{c}$$

The quantity r_s/c can be defined as the age of the Loop assuming no deceleration of the shock front. The expression for t shows that the larger the power n the more rapid the deceleration. The quantity r_s/c is obtained from Hubble's measurement of the actual angular expansion of the Cygnus Loop of 0.06"/yr coupled with the measured diameter of ≈160'. If the assumption is made that this expansion appears to proceed at the shock velocity then these measurements give r_s/c = 160000 years. Thus the age for model (0,216) becomes 64000 years and the age for model (10,27) becomes 21000 years.

J. Initial Explosion Energy

The energy involved in mass motion in the initial explosion, E_o, can also be estimated from these models and the x-ray observations. From above combining the expressions for c and r_s, and solving for E_o gives:

$$E_o = \beta\, c^2\, r_s^3\, \rho_o \left(\frac{5+n}{2}\right)^2$$

The value of the constant β is obtained from figure 14. The values of β appropriate to each model are given in Table 14. The density, ρ_o, for each model

was taken from Table 12. The energies found for each model are given in Table 14.

TABLE 14

KINEMATIC ENERGY OF INITIAL SUPERNOVA EXPLOSION

	Model (0,216)	Model (10,27)
Constant β	0.49	0.042
E_o (ergs)	4.0×10^{49}	1.3×10^{50}

K. Concluding Remarks

Two models of the physical structure of the Cygnus Loop have been considered above in some detail. Both models explain the x-ray emission through the interaction of a shock wave from a supernova explosion and the interstellar medium. The passage of this shock wave through the interstellar gas gives rise to high temperature plasmas which produce the x-radiation observed.

One model is the development of a model proposed by Tucker (1971). This model treats the passage of a shock wave through an initially homogeneous interstellar medium. A major difficulty is that this model requires a shock velocity ≈ 3 times as large as would be consistent

with optical spectroscopic measurements of the velocity of the filaments.

The other model is an inhomogeneous model suggested as an approximation to the situation of a shock wave encountering the abrupt boundary of a dust lane or an interstellar cloud. The model is inhomogeneous in that it assumes that the initial distribution of the interstellar material varied according to $\rho = \rho_o(r/r_o)^{10}$. This model requires a shock velocity only as large as that implied by the optical spectroscopic velocity measurements.

Both models give consistency with the spectral observations of the Cygnus Loop reported in section IV although the models are not very refined in this aspect. They also qualitatively account for the observed spatial structure. Quantitatively the homogeneous model is somewhat less able to give the peak in intensity seen at the edge of the Loop than is the inhomogeneous model although both models fail slightly in this regard. The data seems to suggest either a sharper boundary or a higher shock velocity than assumed in the inhomogeneous model.

The observed line emission is consistent only with the predictions of the inhomogeneous model. The homogeneous model predicts 7 times more line emission than

is actually observed. This must be regarded as another major difficulty with the homogeneous model.

The best estimate of the mass of the x-ray emitting region is $\approx 170\ M_{\odot}$. Both models give this value. The original energy released by the supernova explosion in mass motion is found by the two models to be between 0.4 and 1.3×10^{50} ergs. The age of the Cygnus Loop given by the homogeneous model is 6×10^{4} years and from the inhomogeneous model 2×10^{4} years.

The models cannot account for the intense resolution element observed in the x-ray intensity map just to the east of the center of the Loop (see figure 3). This region would require an inordinately large density of matter in a small region displaced in front of or behind the Cygnus Loop if it is to be explained on the basis of the shock wave mode. The possibility that this resolution element represents the emission from a point source cannot be ruled out by this experiment. This source, if indeed present, would not necessarily be located at the same distance as the Loop. More observations are needed to resolve the questions posed by the existence of this unique feature in the x-ray map.

The two models developed here do not treat the question of optical emission. Cox (1972) has proposed that the optical emission occurs in the final stages of

the evolution of supernovae remnants. He has suggested that the emission in x-rays and UV radiation becomes sufficient at some stage to dominate the subsequent dynamics of the shock wave. He shows how this leads to very dense sheets of gas with thickness $\approx 10^{15}$ cm. These sheets have temperatures $\approx 10^{4} - 10^{5}$ ^{o}K and are strong emitters of optical line emission. Seen edge-on they form narrow filaments such as those seen in the Cygnus Loop. The evolution of the x-ray emitting regions after optical emission becomes pronounced has not been treated in any depth. Certainly these high temperature plasmas must gradually cool through expansion and radiative losses. It is to be expected that optical emission will be visible after the x-ray emission has ceased, since the optical emission in general requires lower temperature plasmas than does the x-ray emission. So regions could exist with appreciable optical and little or no x-ray emission. The arc to the southwest of the Cygnus Loop would appear to be such a region, for it displays no appreciable x-ray emission. Also the western edge of the Loop, NGC 6960, shows little x-radiation and relatively strong optical emission. This region would seem to be a region where the major portion of the shock front's energy has been dissipated at some earlier epoch. All that remains today is

essentially the low temperature plasmas giving rise to the optical emission.

NGC 6992-5, on the other hand, displays strong emission in both Hα and x-radiation. From this discussion it would appear that NGC 6992-5 is a region where the shock front has recently encountered a relatively dense region of gas and has been strongly decelerated. Since the region to the south of NGC 6992-5 displays x-ray emission and almost no optical emission this must be a region where the interstellar density is low and where the shock wave's motion has been relatively unabated.

The overall picture which developes from the above discussion is that the geometrical center of the Cygnus Loop is not the kinematic center, i.e. the site of the initial supernova explosion. This kinematic center would seem to be displaced to the west of the geometrical center. This displacement would then explain the differences in the current x-ray emission intensities seen from NGC 6960 and NGC 6992-5. NGC 6960 becomes the position where at some much earlier epoch the shock wave encountered the dust lane which now lies to the west of the Loop and was decelerated substantially by this encounter. In the opposite direction the shock wave proceeded essentially unhindered until it encountered an interstellar cloud at the present position of NGC

6992-5. This encounter occurred more recently than that of NGC 6960.

Clearly much of this discussion is preliminary and further observational evidence is needed to provide substantiation. Further theoretical work is also required to establish what the temporal behavior is of the radiation produced by a shock-wave encountering the abrupt boundary of an interstellar cloud or a dust lane. Future x-ray observations with higher spatial resolution than employed in this experiment will do much toward increasing the knowledge of the physical processes at work in the Cygnus Loop.

APPENDIX A: CALIBRATION OF DETECTOR WINDOWS

As described in section II there were two kinds of thin plastic windows used in this experiment. Detectors A and B had kimfol windows. The single window on detector C and both of the two windows on detector D were polypropylene plastic.

The kimfol plastic used in detectors A and B was as supplied by the commercial manufacturer. Previous tests have shown that this plastic is quite uniform and since detectors A and B were used primarily for spatial mapping only spot checks on their windows' surface densities were carried out. These consisted of measuring the x-ray transmission of several 2 cm x 2 cm samples of the window material at some five energies between 0.2 and 2.5 kev.

The surface densities of the polypropylene windows used on detectors C and D were also obtained by measuring their x-ray transmission at several energies.

A value of the surface density is obtained at each energy at which the window's x-ray transmission is measured. At the energies involved here x-rays are absorbed according to an exponential law, i.e. if x-rays of intensity $I_o(E)$ at energy E are incident on a slab of material of surface density σ having an absorption

coefficient $\mu(E)$ at energy E, then the intensity of x-rays which are transmitted by the slab, I(E), is given by:

$$I(E) = I_o(E) \exp(-\mu(E)\,\sigma)$$

Thus at a particular energy E' measurements of I(E') and $I_o(E')$ together with knowledge of $\mu(E')$ give the surface density at this energy:

$$\sigma(E') = \frac{1}{\mu(E')} \ln \frac{I_o(E')}{I(E')}$$

For a uniform sheet of material with a well determined absorption coefficient, this surface density will be independent of energy. However even for such a material the experimentally determined surface density will appear to vary with energy because of the experimental inaccuracies. In general at each energy E a different surface density $\sigma(E)$ will be found with some accuracy $\delta\sigma(E)$. The errors in the experimentally measured quantities I(E) and $I_o(E)$ are $\delta I(E)$ and $\delta I_o(E)$ respectively. From these the error $\delta\sigma(E)$ can be obtained by differentiation of the expression given above for $\sigma(E)$. This gives:

$$\delta\sigma(E) = \pm\frac{1}{\mu(E)} \left[(\delta I(E)/I(E))^2+(\delta I_o(E)/I_o(E))^2\right]^{\frac{1}{2}}$$

The χ^2 criterion with χ^2 defined by:

$$\chi^2 = \sum_i \left(\frac{\sigma(E_i) - \sigma_o}{\delta\sigma(E_i)} \right)^2$$

can now be used to test the hypothesis that the surface densities measured at different energies are statistically consistent with a constant surface density, σ_o, independent of energy. Indeed the requirement that the χ^2, considered as a function of σ_o, be a minimum for the best guess value of the surface density, i.e. for σ_o, can be used to obtain this best guess value. Differentiating χ^2 with respect to σ_o and setting the result equal to zero gives the minimum value sought. It also gives upon rearrangement:

$$\sigma_o = \frac{\sum_i \frac{\sigma(E_i)}{(\delta\sigma(E_i))^2}}{\sum_i \frac{1}{(\delta\sigma(E_i))^2}}$$

Adopting this value of σ_o the value of χ^2 becomes:

$$\chi^2 = \sum_i \left(\frac{\sigma(E_i)}{\delta\sigma(E_i)} \right)^2 - \sigma_o \sum_i \frac{\sigma(E_i)}{(\delta\sigma(E_i))^2}$$

A table of the χ^2 distribution test can now be employed

to determine at what confidence level the hypothesis of constant surface density is valid.

The kimfol plastic was tested as outlined above and was found to be consistently described by a constant surface density of 270 $\mu gm/cm^2$.

The values of $\sigma(E_i)$ and $\delta\sigma(E_i)$ found at several energies E_i for the polypropylene windows were found to be inconsistent with a constant surface density independent of energy. The values of σ_o and χ^2 obtained for this constant surface density model are given below in Table 15. Indeed the polypropylene plastic windows visually displayed multi-color streaks. The difficulties inherent in uniquely assigning a particular surface density to regions of a particular color are discussed in Appendix C. The important conclusion reached is that the visual color is not a valid means of determining the thickness of the polypropylene. However the multi-color streaks are suggestive of non-uniform thickness. Indeed the method of obtaining these films (see Appendix C) does not discriminate, except in a crude way, against the existence of more than one thickness. Since the transmission properties of these films were of importance in determining the spectra of the Cygnus Loop, these films were measured at some length.

The polypropylene windows used on detectors C and

TABLE 15

WINDOW PARAMETERS DETECTORS C AND D

	Constant Surface Density Model			Two-Thickness Model					
Window Section	σ_o(μgm/cm^2)	χ^2	DOF*	p_1	σ_1(μgm/cm^2)	p_2	σ_2(μgm/cm^2)	χ^2	DOF
Window C End 1	143 ± 1.7	9.9	3	0.2	368.0	0.8	113.0	1.53	1
Window C End 2	138 ± 1.5	35.1	3	0.2	449.6	0.8	105.1	1.69	1
Window D End 1	270 ± 2	25.4	5	0.1	793.6	0.9	245.6	5.69	3
Window D End 2	273 ± 7	3.9	2	**					

*DOF: Degrees Of Freedom in χ^2 criterion

** One of the two windows comprising window D end 2 was measured at 284 ev only

D consisted of two sections each approximately 11 cm by 24 cm. Each window was measured still attached to the aluminum frame which was used to maintain the physical dimensions of the film (see Appendix C). This ensured that the film as measured was under nearly the same overall stretch as it was in the flight configuration. The windows in-flight supported 15 cm differential pressure but it did not prove possible to easily duplicate this condition in the lab so the film as measured was under zero differential pressure. Each section of the window was measured in 1.3 cm wide strips across the short dimension of the section. The transmission of each such strip along the length (≈19 strips long) of the window was measured at more than four of the following energies, 0.28 kev (C Kα x-rays), 0.52 kev (O Kα), 0.57 kev (Cr Lα), 0.68 kev (F Kα), 0.85 kev (Ni Lα) , 0.93 (Cu Lα), 1.04 kev (Na Kα), 1.23 kev (Mg Kα) and 1.49 kev (Al Kα). Surface densities were obtained for each 1.3 cm wide strip across the window at each energy. Hence the values of surface density obtained could depend on both the strip of window and on the energy. It was found that the values of surface density obtained did not show any dependencies on which strip of window was examined. This was apparently because the color streaks ran across the strips rather than

along them. So each strip represented an average of dissimilar regions. Such an average might show no strip dependence but it would still be expected to show energy dependence and indeed such a dependence was observed. This observed energy dependence was explained by means of a simple two-thickness model of the polypropylene film.

This two-thickness model breaks the total area of window into two fractions p_1 and $p_2 = 1 - p_1$. The fraction p_1 of the window is assumed to have a uniform surface density σ_1 and the rest of the window, a fraction p_2, is assumed to have a surface density σ_2, different from σ_1. Then the predicted transmission of the entire window at energy E is given by:

$$T(E) = p_1 e^{-\mu(E)\sigma_1} + p_2 e^{-\mu(E)\sigma_2}$$

An average surface density s(E) can be obtained from the relation

$$S(E) = \frac{-\ln T(E)}{\mu(E)}$$

Because of the unequal surface densities σ_1 and σ_2 the average surface density defined in this way will be energy dependent. Since p_1 and p_2 are related by $p_1 + p_2 = 1$, this is a 3 parameter model, p_1 (or p_2),

σ_1 and σ_2 . The values of the parameters, p_1 , σ_1 and σ_2 were taken to be those values which minimized the χ^2 defined by:

$$\chi^2 = \sum_i \left(\frac{\sigma(E_i) - s(E_i)}{\delta\sigma(E_i)} \right)^2$$

For the polypropylene windows $\delta\sigma(E_i)/\sigma(E_i) \approx 1 - 6\%$. Several two-thickness models were found to give acceptable fits to the measured $\sigma(E_i)$ according to the χ^2 criterion. Table 24 gives the parameter values which gave the minimum χ^2 .

As mentioned in section II the lower section of the outer gas cell window in front of Detector D broke during reentry. It was restretched using tape to mend the broken areas and calibrated. It was measured only at C Kα (0.28 kev). This measurement agreed quite well with the measurement for window D end 1 so the results of window D end 1's calibration were assumed true for end 2 also.

The two-thickness model is used herein as the next higher approximation beyond the constant surface density model. It was chosen not because it necessarily provides a valid description of the physical situation but because it is computationally simple and because it provides an adequate description of the measured

transmission properties of the polypropylene windows. Figure 24 and Table 15 show that this model works substantially better than the constant surface density model.

Figure 24. Measured surface density of window C end 1 as a function of energy. The data points are the experimentally determined values. The curves show the two models discussed in the text. Curve a is the two-thickness model with $p_1 = 0.2$, $\sigma_1 = 368.0$ $\mu gm/cm^2$ and $p_2 = 0.8$, $\sigma_2 = 113.0$ $\mu gm/cm^2$. Curve b is the constant surface density model with $\sigma_o = 143$ $\mu gm/cm^2$.

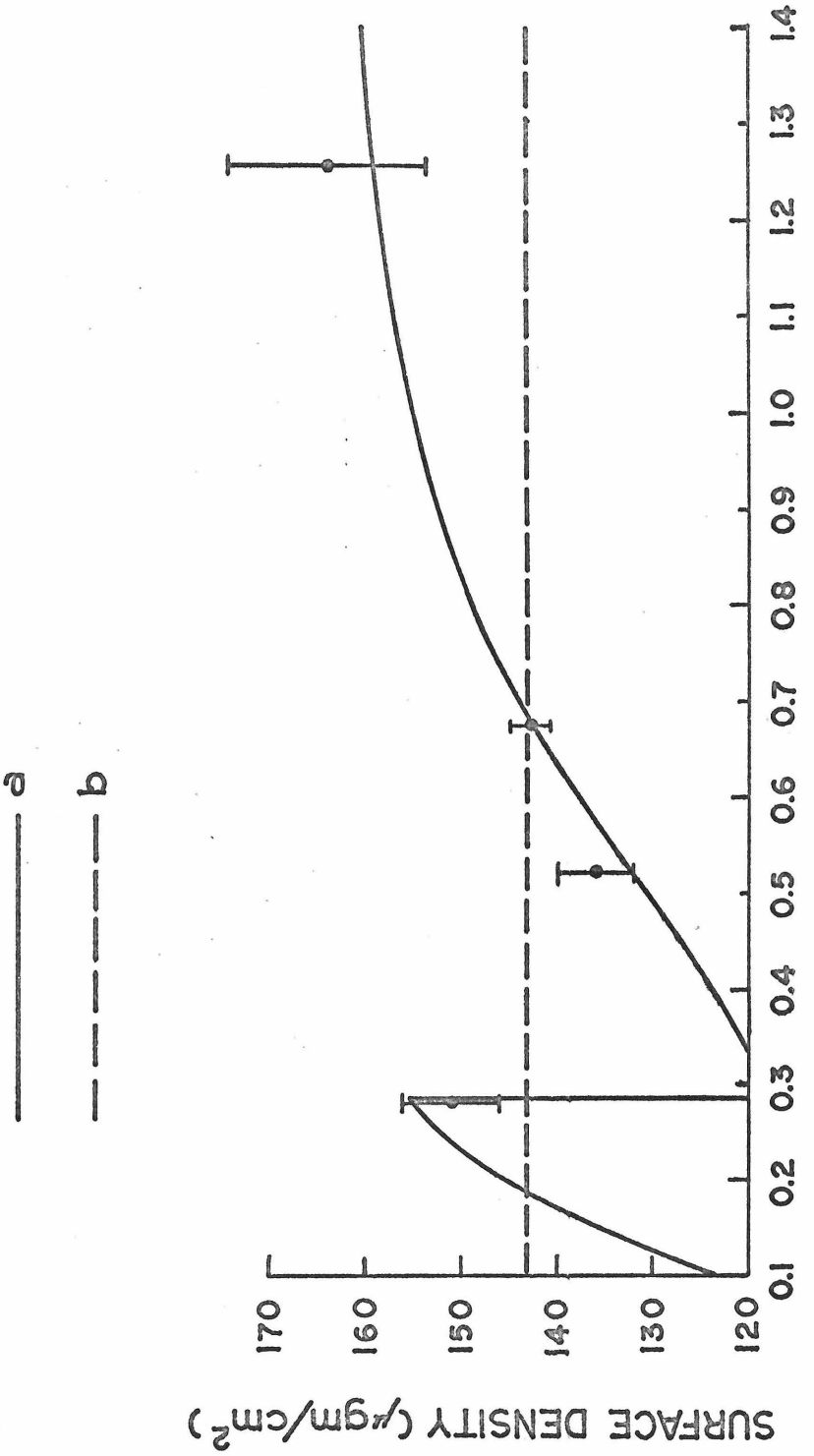
a
b
SURFACE DENSITY (μgm/cm²)
170
160
150
140
130
120
0.1
0.2
0.3
0.4
0.5
0.6
0.7
0.8
0.9
1.0
1.1
1.2
1.3
1.4
ENERGY (kev)

Figure 24.

APPENDIX B: COLLIMATORS DESIGN, ASSEMBLY AND CALIBRATION

1. Overview

The collimators used on this experiment were of two types, slat or egg-crate and stacked-grid. The egg-crate collimators provided a large field of view and were used on all detectors to support the windows. The stacked-grid collimators were used on detectors A and B to provide the 0.4^{o} wide fan beam necessary for mapping the x-ray structure of the Cygnus Loop.

The egg-crate collimators were of a standard design and have been adequately described in the literature (Giacconi et al, 1968). This appendix will describe only the calibration procedure for these collimators.

The stacked-grid collimators are more unique. This type of collimator has been used infrequently so the design parameters and construction of this type of collimator have not been reported in the literature. Hence both the design details and the calibration procedure will be described for these collimators.

2. Stacked-Grid Collimators Design

The basic unit is an etched stainless steel plate. This has rectangular holes etched in a regular pattern leaving a grid of stainless steel wires. These grids are

then stacked so that the rectangular holes align and form cells. The cells provide the mechanical collimation required.

Consider first the simple collimator composed of opaque slats of width d spaced a distance s apart. These slats collimate by virtue of their shadowing properties. Referring to figure 25, the transmission at an angle θ to the normal is $w/(s + d)$, w is the width of the region of unshadowed transmission normal to the line of sight between consecutive slats and $s + d$ is the distance between the centers of consecutive slats.

$$s = s_1 + s_2$$

therefore $s = w/\cos\theta + L \tan\theta$

and $$\frac{w}{s + d} = \frac{s}{s + d} (\cos\theta - L/s \sin\theta)$$

defining $\tan\theta_o = s/L$ then

$$\frac{w}{s + d} = \frac{s}{s + d} \cos\theta (1 - \tan\theta/\tan\theta_o)$$

for small angles this becomes,

$$\frac{w}{s + d} \cong (1 - \theta/\theta_o) \frac{s}{s + d}$$

The convention in x-ray astronomy is to label the

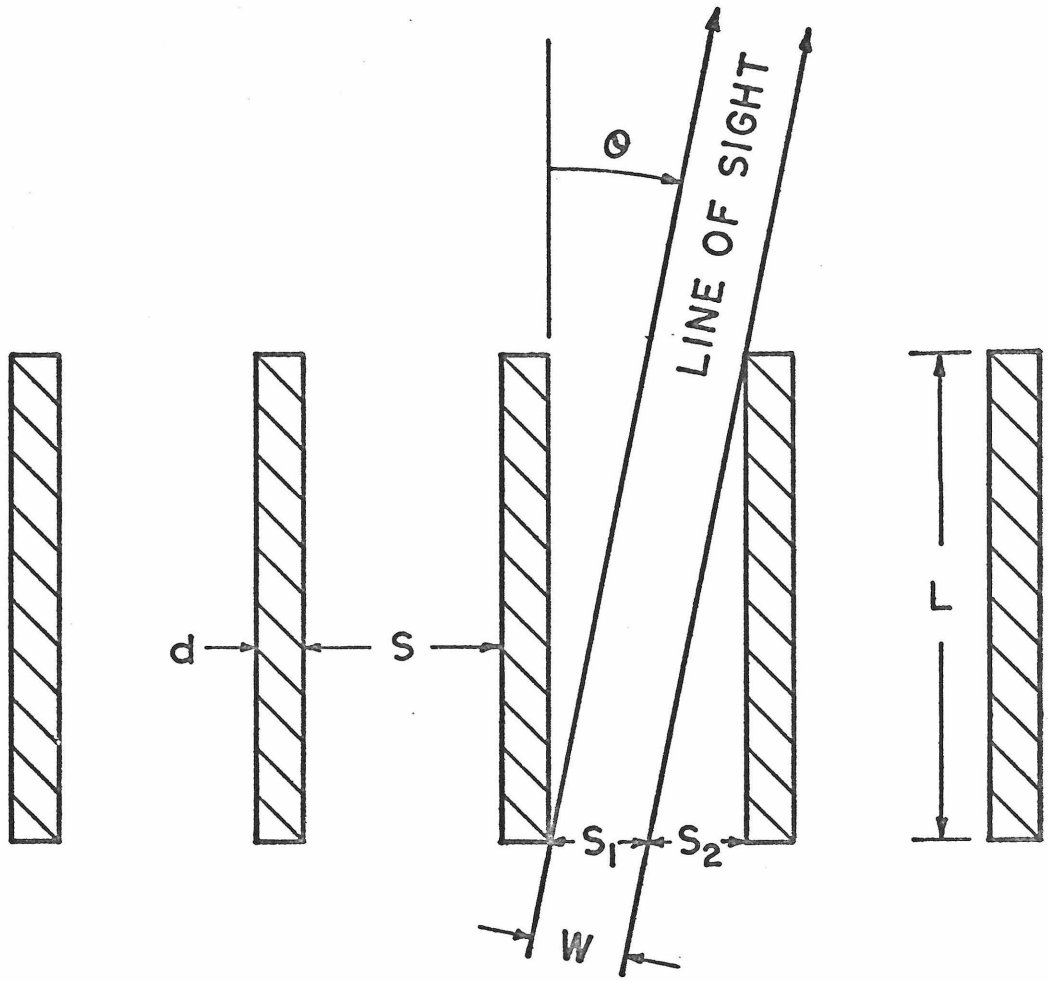

Figure 25. A cross sectional view of a simple slat collimator. This collimates because of the shadowing properties of the slats.

angular response of a collimator according to twice the angle at which the response is one-half the maximum response. This is called the full width at half-maximum (FWHM). In terms of the quantities defined here the maximum response is $s/(s + d)$ at $\theta = 0^{o}$ and the response is down by half when

$$\cos \theta \left(1 - \frac{\tan \theta}{\tan \theta_{o}} \right) = 1/2$$

For collimators having FWHM $< 10^{o}$ the approximate formulae hold and the response is down to half the maximum response when

$$1 - \theta/\theta_{o} \cong 1/2$$

or

$$\theta \cong \theta_{o}/2$$

The FWHM is twice this angle or FWHM $= \theta_{o}$.

To achieve a collimation of $\theta_{o} < 1.0^{o}$ using this technique requires a large number of slats since the height L available is usually restricted by the payload size. These slat assemblies are usually quite massive. Since the altitude reached by the rocket carrying the experiment depends on the weight of the payload and the collimators can represent a sizeable portion of this

weight, reducing the collimators' weight becomes an important design criterion. The stacked-grid collimator reduces the weight of the slat collimator considered above by eliminating those portions of the slats which are redundant. Figure 26 shows the stacked-grid collimator which results. The grids are used to provide those portions of the slats whose shadowing is essential to the production of the desired response pattern. Referring to figure 26 the parameters defining the grid are: t, the thickness of the grid (all grids have this same thickness), d, the wire width and s the distance between wires. The first grid is called grid 0, the second grid 1 and so forth. The distance between grid i and grid i-1 is Δ_i . The distance between grid i and grid 0 is L_i .

Figure 27 shows the critical light ray which determines the location of grid n with respect to grid n-1. This ray grazes the top corner of grid 0 and the bottom corner of grid n-1. Grid n must be close enough to grid n-1 to stop this ray. This is equivalent to requiring that

$$\frac{\Delta_n}{d} \leq (L_{n-1} + 2t)/s \qquad n>1$$

Since $$L_n = L_{n-1} + t + \Delta_n \qquad n>1$$

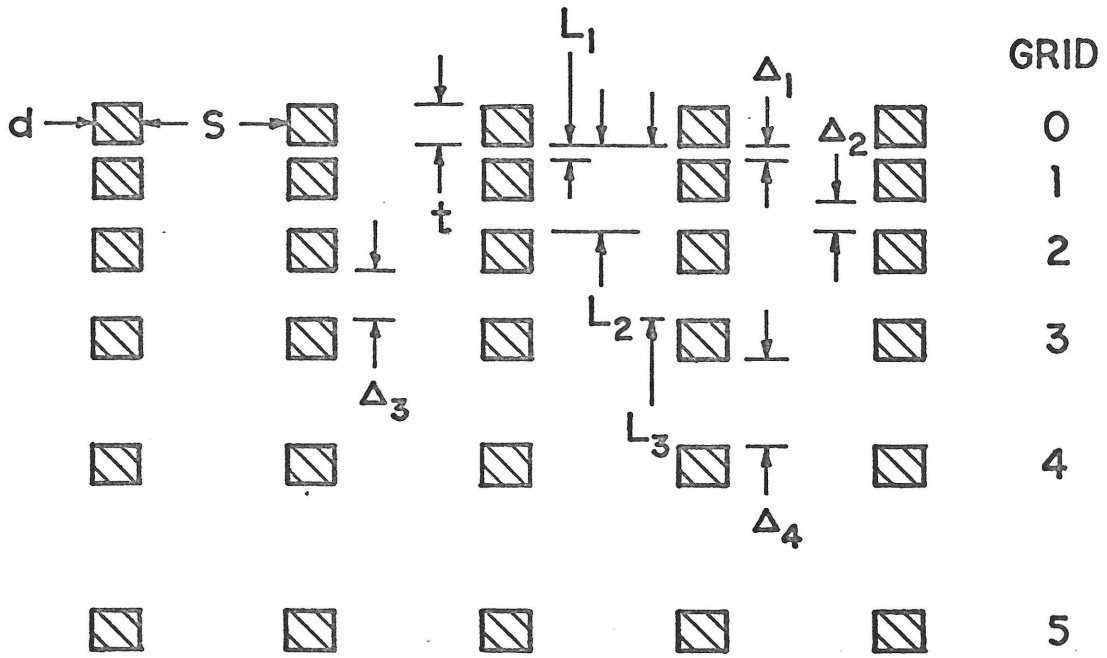

Figure 26. A cross sectional view of the stacked-grid collimator used in this experiment. This collimates because of the shadowing properties of the rectangular wires.

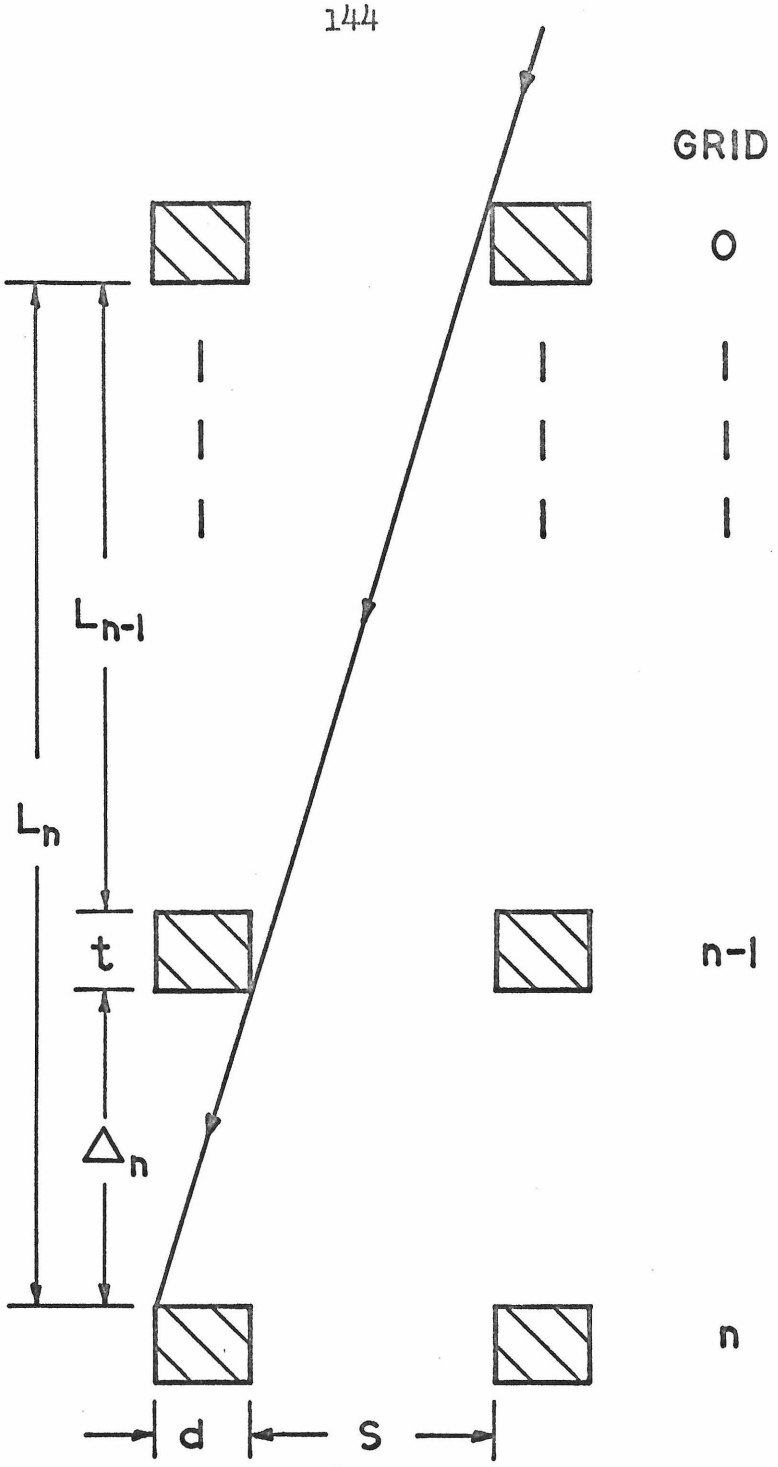

Figure 27. Critical x-ray which locates grid n from the positions of grids 0 and n-1. Grid n must be close enough to grid n-1 to stop this x-ray.

therefore $L_n \leqslant L_{n-1}(1 + d/s) + t(1 + 2d/s) \qquad n > 1$

for $n = 1 \qquad L_1 \leqslant dt/s$

In order for the collimator assembly to achieve the desired collimation i.e. FWHM = θ_o (θ_o is assumed to be less than 10^o) the condition

$$L_{n_o} \geqslant \frac{s}{\theta_o} - t$$

must be satisfied, where n_o is the final grid. These relations are sufficient to determine the minimum number of grids, n_{min}, necessary to achieve the desired collimation. This minimum number will be when the equality holds in the expression for L_n for all the grids $n = 2, \ldots, n_{min}$. When the equality holds it is straightforward to show that

$$L_n = A^{n-1} L_1 + (1 + 2d/s)\, t \sum_{i=0}^{n-2} A^i$$

where $A = 1 + d/s$

using $L_1 = dt/s$, $L_{min} \geqslant s/\theta_o - t$ and

noting that $\sum_{i=0}^{n-2} A^i = \frac{1}{A - 1}(A^{n-1} - 1)$

leads to

$$\frac{s}{\theta_o} - t \leq A^{n-1}\, dt/s + (1 + 2d/s)(A^{n-1} - 1)\, st/d$$

where $n = n_{min}$

recalling $A = 1 + d/s$ this reduces to

$$(1 + d/s)^{n+1} \geq 1 + d/s + d/(\theta_o t) \qquad n = n_{min}$$

which gives

$$n_{min} \geq \frac{\ln (1 + d/s + d/(\theta_o t))}{\ln (1 + d/s)} - 1$$

This expression gives the minimum number of grids necessary to produce the desired FWHM. The expression given depends on the wires of the grid having a rectangular cross-section. The etching process gives the wires a slightly non-rectangular cross-section so more than n_{min} grids are required for complete extinction of the x-rays at angles greater than θ_o. The grids are located with respect to each other by the use of aluminum and magnesium spacers. The commercially available thicknesses of these low-density materials puts some restrictions on the final choice of spacings between grids. This also causes the number of grids to exceed n_{min}. For more than n_{min} grids the grids should be spaced according to

$$\Delta_1 \leq dt/s \qquad L_1 = \Delta_1$$

$$\Delta_n \leq d(L_{n-1} + 2t)/s \qquad n > 1$$

$$L_n = L_{n-1} + t + \Delta_n \qquad n > 1$$

These equations determine the critical parameters necessary for the design of these collimators. The maximum desired transmission and the difficulties involved in etching the grid determine the wire width d, the spacing s and the thickness t . For this experiment d was .015 cm, t was .013 cm and s was .048 cm. The collimation achieved using 24 grids was .007 rad (0.4°) FWHM.

The etched grids and the spacers which determine the grid separations are relatively expensive but this cost is partially defrayed by the ease of assembly. Assembly is aided by including small notches in the edges of the etched grid to serve as fiducial marks. Also etched in the edge of the grid are holes to provide passage for long bolts which hold the grids and spacers together as an integral sandwich. Since it is considerably cheaper to etch these grids in small areas, use of this integral sandwich approach allows several small area collimators to be assembled and calibrated separately and then combined to form the final configu-

ration. Figures 28 and 29 show a grid and spacer respectively which are identical to those used in this experiment.

There were two stacked-grid collimators used in this experiment. These were initially assembled as four separate smaller collimators. These four collimators were independently calibrated. During calibration small mirrows were permanently attached using quick-curing epoxy to each collimator to indicate the direction of the collimator's maximum responser. Then these four collimators were paired to form the final two collimators. The separate packages were mounted in one frame which locates the collimators in front of the detectors. Each member of each pair of collimators was aligned with respect to the other member of the pair by optically aligning the normal directions of their mirrows.

3. Collimators' Calibration

The calibration of these collimators separates into two parts. First the collimators' angular response must be measured since significant departures from theory are usually present. Then the response maximum for each collimator must be referenced to the camera's field of view in order to know where each collimator is pointed during the actual experiment.

Figure 28. Grid used in the stacked-grid collimators of this experiment shown at ≈90% of its actual size. The thin wires provide the collimation. The wider wires are for support. Note the fiducial marks in the lower and upper edges near the right side and in the center of the left hand edge. The holes are for the long bolts which held the grids and spacers together.

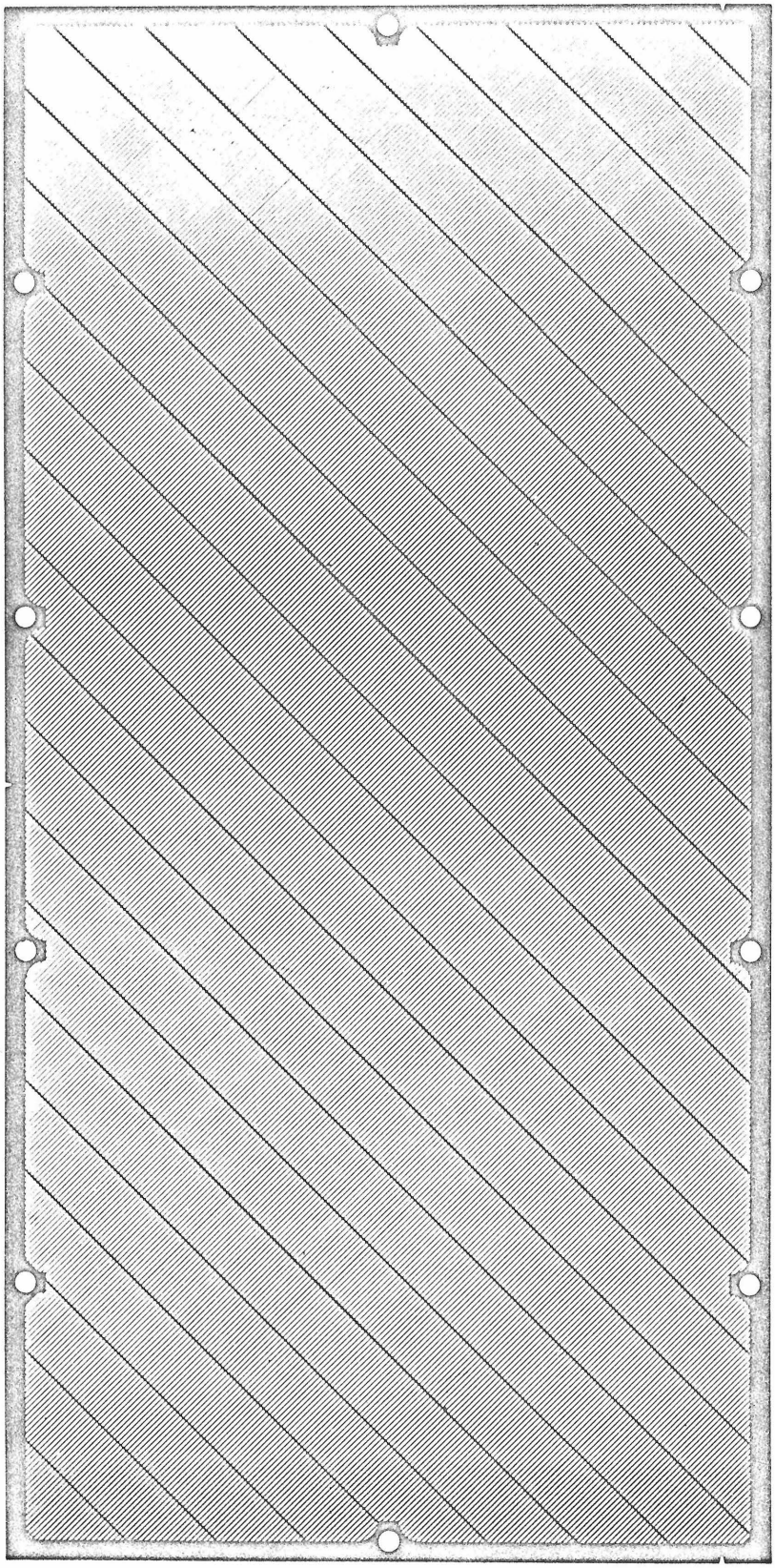

Figure 28.

Figure 29. Spacer used in the stacked-grid collimators of this experiment shown at ≈90% of its actual size. Note the notches at the location of the fiducial marks in the grids. These allow alignment of the grids without hindrance by the spacers.

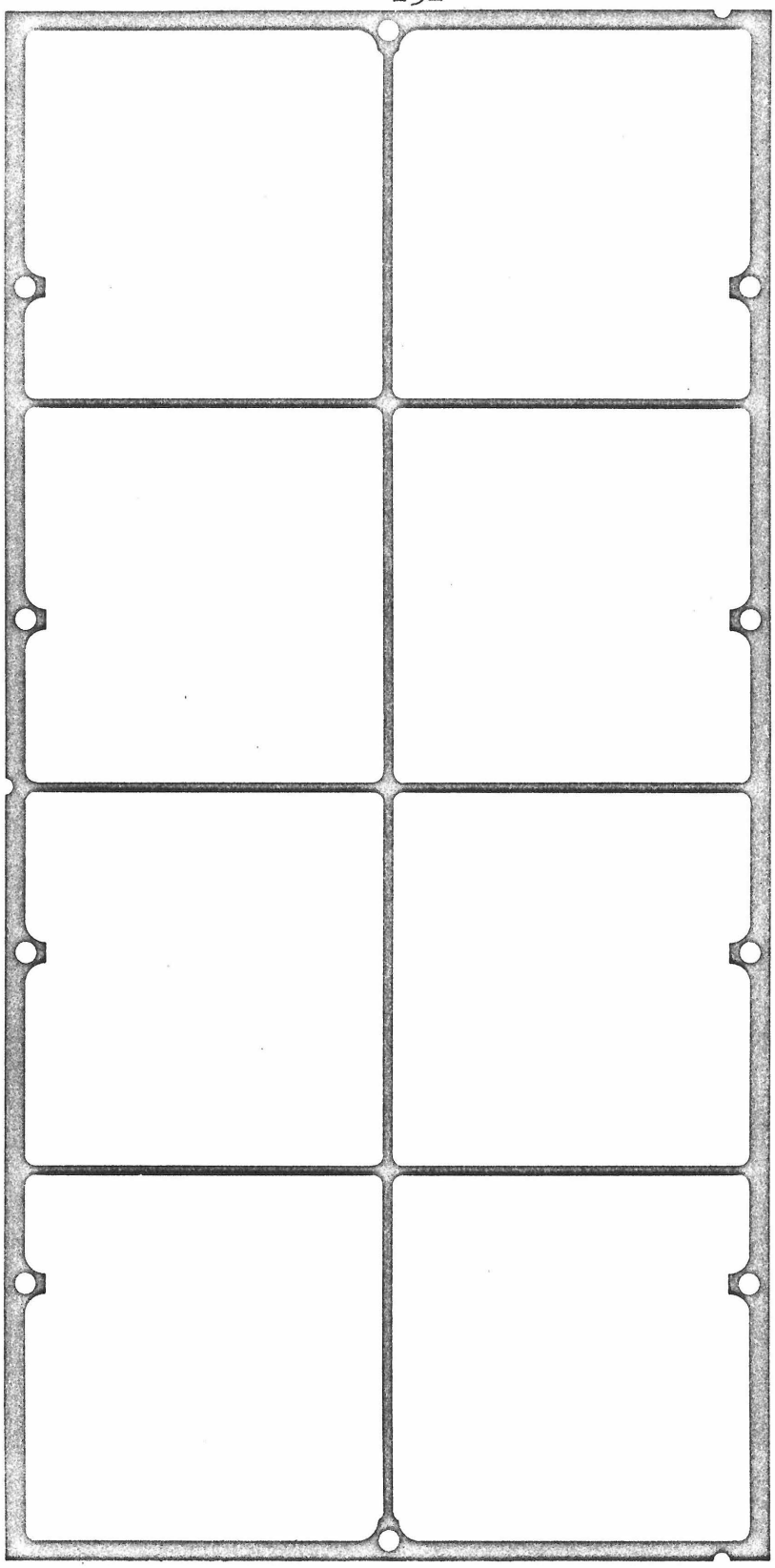

Figure 29.

The angular response of each of the egg-crate collimators was measured along both of the principle directions of the collimator. The response of the stacked-grid collimators was measured only in the narrow field of view direction since the collimation of these collimators in the other direction is nominal.

The angular response of the collimators was measured by passing a fan beam of x-rays through the collimator into a proportional counter. The modulation of the x-ray intensity measured by the proportional counter as the collimator-to-beam angle is varied gives the angular response of the collimator in one of its principle directions. The collimator is then rotated through 90^{o} and its angular response in the other direction is measured.

The fan beam was defined by two slits, one at the x-ray source and the other at the proportional counter. The angular spread of the beam depends on the size of both slits. These slits were chosen so as to give a beam width of less than 1/10 the collimator's width (FWHM). Another detector shared the x-ray beam but was not modulated by the collimator. This detector monitored the beam intensity so that variations in this intensity did not distort the angular response measurement.

The x-rays were produced by a commercial x-ray machine with a chromium target. This was run at 16 kev accelerating potential and therefore produced thick target bremsstrahlung with little line emission. The aluminum slats begin to be significantly transparent to x-rays above ≈10 kev so these higher energies were reduced by putting a 0.007 cm sheet of copper foil in the beam between the source and the first slit. This sheet converted a large fraction of these higher energy x-rays to 8.0 kev x-rays, the Cu Kα transition. The x-rays detected by the proportional counter were put through a window discriminator to further restrict the high energy x-rays sampled during calibration.

The FWHM measured in this way for the various collimators are given in Table 16. The stacked-grid collimators were also examined with regard to possible secondary transmissions outside the primary response pattern of these collimators. These secondary responses would occur if the grids did not provide complete shadowing at some angle. Extensive examinations showed no secondary maxima in the angular response of these collimators. A secondary maximum would have been detected in these investigations if its integrated intensity had exceeded 5% of the integrated intensity of the primary maximum.

TABLE 16

MEASURED ANGULAR RESPONSE OF COLLIMATORS

Collimator	Detector	Measured FWHM
Egg-crate	A	$9.8^{\circ} \times 19.6^{\circ}$
Egg-crate	B	$9.8^{\circ} \times 19.6^{\circ}$
Egg-crate	C	$12.2^{\circ} \times 11.9^{\circ}$
Egg-crate	D	$12.0^{\circ} \times 11.8^{\circ}$
Stacked-grid	A	0.42°
Stacked-grid	B	0.43°

The theoretical angular response function for both the eggcrate or slat collimators and the stacked-grid collimators is the usual isosceles triangle (Giacconi et al, 1968). The measured values showed small (less than 10%) departures from these theoretical angular response functions. The measured response curves were all smooth functions which displayed a tendency to be slightly broader than the theoretical response functions. A careful examination of the response curves showed no "wings" (increased width at the base of the triangle).

The angular response function of its collimators defines the direction which each detector views. In order to relate these directions to the α, δ astronomical coordinate system during the actual experiment, the directions of maximum response for each collimator were recorded by the aspect camera before and after the flight.

This cross-referencing of the collimator maximum and the camera's field of view was done by first locating small mirrows on each collimator so that the normal to the mirrow was coincident with the direction of the collimator maximum. Then both before and after the flight these mirrows were used to complete the cross-referencing sequence. Use of these mirrows permits the collimators to be measured once using x-rays and then all later alignment can be done using visual optics.

The mirrows were located as follows: the direction of maximum response for each collimator was determined during the angular response measurements and the collimator was oriented so that this direction coincided with that of the x-ray beam. The x-ray source was then replaced by a laser. Using this laser a small mirrow was positioned so that the laser, striking this mirrow, returned on itself. For the egg-crate collimators this mirrow was only temporarily attached to the collimator. For the stacked-grid collimators this mirrow was epoxied to the framework of the collimator. The epoxy used required ≈5 minutes curing time. It proved quite easy to tweak the mirrow into alignment using a pair of tweezers as the epoxy cured.

The completion of the cross-referencing sequence also used the laser. First the laser was oriented so

as to strike a mirrow and return upon itself. Then the laser was translated parallel to itself using a mill table until it was shining into the camera through an appropriate neutral density filter. It was then photographed and produced a well defined spot on the film which was referenced to two similar spots produced by two fiducial light sources located in the camera's focal plane. The directions of all of the collimators' maxima were recorded in this way. The two fiducial lights allowed cross-referencing between the maxima of the various collimators and, after the experiment, cross-referencing between the derived spatial locations and the detectors' viewing directions.

More care was taken with the calibration of the stacked-grid collimators than with the egg-crate collimators. For the stacked-grid collimators the positioning of the mirrows and the location of the mirrow's direction on the camera's film was done to $\approx\pm 2$ arc minutes. The inaccuracies involved in determining the aspect brought the total error in the positioning for the stacked-grid collimators to $\approx\pm 5$ arc minutes. The directions of the egg-crate collimators were determined with a positional accuracy of $\approx\pm 20$ arc minutes.

In addition to determining the direction of the collimator's maximum response, the spatial data reduction

required determination of the angular orientation of the collimators. This was determined by referencing to a direction established on the camera film during the cross-referencing sequence. The inaccuracy of this angular determination was $\sim \pm 0.3^{o}$ for most of the Cygnus Loop measurement. However for the measurements taken during the rapid rotations in pitch occuring at ~190 sec and ~230 sec this inaccuracy was somewhat larger $\sim \pm 2.0^{o}$.

APPENDIX C : POLYPROPYLENE PLASTIC WINDOWS; STRETCHING AND MOUNTING TECHNIQUES

1. Overview

The polypropylene plastic used in this experiment as window material for detectors C and D is not commercially available in micron thicknesses. Polypropylene plastic is available from several manufacturers in 0.0025 cm thick sheet. Such sheet was stretched to micron thicknesses by the processes described below. This stretching involves a great deal of elastic as well as inelastic deformation. When the sheet is stretched and released it will contract and thereby become thicker. In this experiment the dimensions of the stretched plastic were maintained by epoxying the plastic to an aluminum frame while it was in its stretched configuration. The plastic window and its frame were then used as a single unit on the detector. This mounting arrangement is detailed below.

2. Stretching Techniques

Several techniques of stretching the 0.0025 cm thick sheet were tried. One, the "bubble" method, was marginally successful over small areas while another, the "tube" method was quite successful and provided the plastic films used in this experiment.

The marginally successful "bubble" technique stretched the plastic by blowing the flat sheet into a spherical bubble. The apparatus is shown in figure 30. It consists of a metal ring which can be bolted to a lucite plate. Between this ring and plate is placed a sandwich composed of a ≈0.3 cm thick gum rubber sheet, the 0.0025 cm thick polypropylene sheet and a 0.04 cm thick gum rubber gasket. The ordering is shown in figure 30. Gas is admitted through an inlet in the lucite plate to inflate the bubble. The ≈0.3 cm thick gum rubber sheet helps to achieve a more uniform result. Heating the polypropylene sheet with heat lamps shining through the lucite plate during inflation also increases the likelihood of a satisfactory result. The polypropylene sheet was given an opaque coating of carbon using an aerosol form of carbon dag before inflation in order to increase its heat absorption. This carbon coating, since it will concentrate the heat absorption to the unstretched areas of the polypropylene, provides some negative freeback and therefore also promotes uniformity of the final film. Equally satisfactory results were also obtained by putting the ≈0.3 cm thick rubber sheet between the lucite plate and the polypropylene sheet and heating from the ring side.

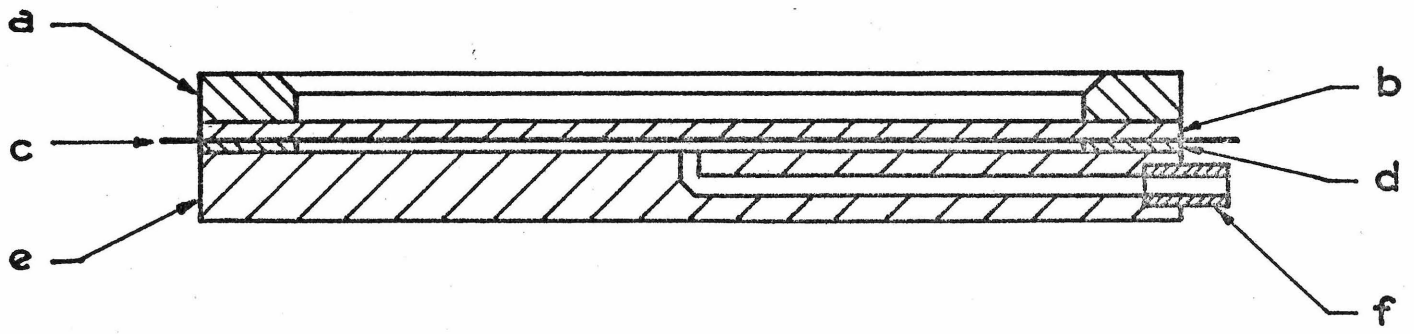

Figure 30. A cross sectional view of the apparatus used to blow polypropylene bubbles. The various pieces are: a-a metal ring having one inside edge (up in the figure) beveled, b-a gum rubber sheet ≈0.3 cm thick, c-the 0.0025 cm thick polypropylene sheet to be inflated, d-a gum rubber gasket 0.04 cm thick, e-a lucite plate with, f-the gas inlet for inflation.

The results obtained with this technique depend to a large extent on the personnel. Patience and experience are required to produce useable results. The films which this technique yields are not flat and this increases the difficulty of using them. This technique also appears to have definite size limitations. A 15 cm ring was employed with success but attempts to extend the method to a 51 cm ring were completely unsuccessful. This method seems to produce more uniform and slightly thinner films than those produced by the "tube" method.

All methods of stretching have to contend with thin striations of unstretched polypropylene which are always present to some degree. Even small amounts of non-uniformity can sizeably affect the x-ray transmission properties of these plastic films (see Appendix A). To an extent depending entirely on the operator's finesse and patience these striations can be removed by localized application of heat when using the "bubble" method.

The "tube" technique uses several of the operations discussed above for the "bubble" technique. The apparatus is shown in figure 31. It consists of a double set of rings which bolt together holding a sheet of polypropylene flat. This sheet is then forced over the end of a tube. As the sheet is pressed over the tube the

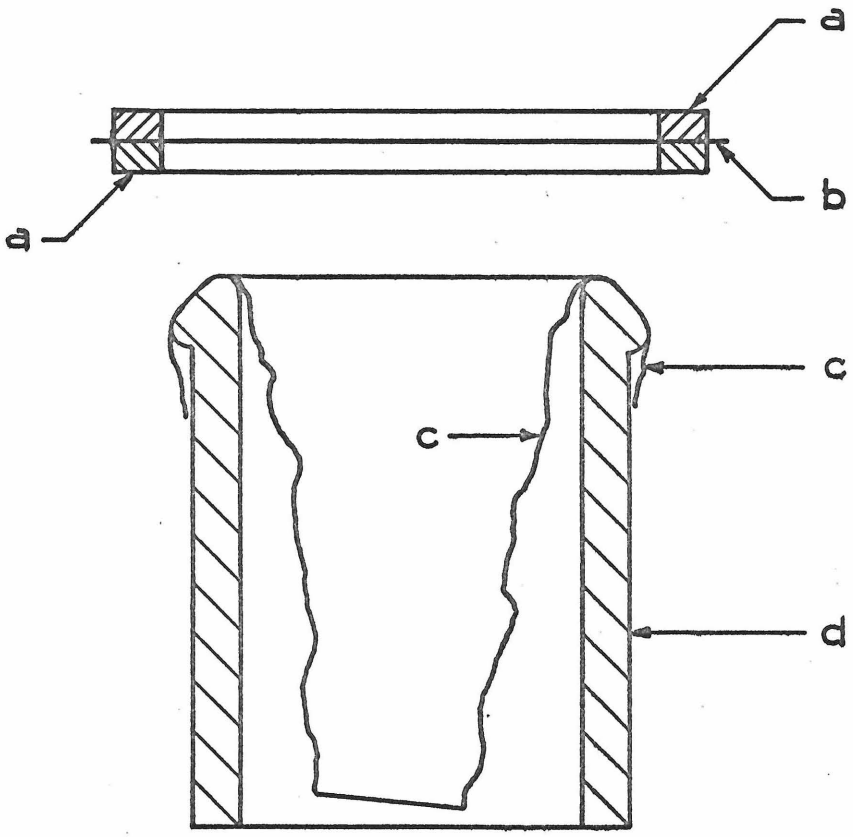

Figure 31. A cross sectional view of the apparatus used to stretch polypropylene sheets. The various pieces are: a-metal holding rings, b-0.0025 cm thick polypropylene sheet, c-fabric tube and d-metal tube (note the upset, beveled and polished end on tube).

portion of the sheet remaining over the end of the tube sees a uniform radial force which stretches it. The tube end is rounded and polished to reduce drag. A tube of fabric is used between the tube and the polypropylene sheet as a lubricant and conveyor. The fabric tube starts inside the metal tube with its end folded back over the end of the metal tube (see figure 31). As the polypropylene is forced over the end of the tube it drags the fabric tube with it. The fabric does not need to be attached to the rings holding the polypropylene, the friction alone is sufficient to draw it along the tube with the polypropylene. The best results were obtained using fabric of a loose knit composition. The amount of force required to force the polypropylene over the tube is considerably reduced if the polypropylene is heated before and during the stretching process. The heating of the polypropylene is facilitated by coating it with carbon in the same way as described above for the "bubble" technique. It was found that one person could, without assistance, easily stretch windows using the 40 cm diameter rings. CAUTION: When using this technique avoid standing directly over the tube while stretching the plastic since this position could result in injury and/or loss of teeth if the plastic should break.

The primary difficulty in both of these techniques lies in knowing when to stop stretching. The plastic is thin enough so as to display color fringes but these did not prove to be a reliable indicator of the film's thickness. Apparently the fringe color seen depends both on the macroscopic thickness and on the direction and degree of the alignment of the polymer chains at the microscopic level. In addition the carbon coating makes these fringes difficult to observe. The knowledge of when to stop stretching comes only with experience. The colors sometimes provide a guideline. Another possible indication is an apparent increase in the force required to push the ring down the tube just before the film breaks. With experience the variation in the final thickness of the stretched films can be less than 10%. The individual films are also non-uniform in thickness (see Appendix A).

3. Mounting Techniques

Most of the stretching done to the polypropylene is non-elastic distortion. This accounts for the majority of the ≈20:1 reduction in thickness. However there is a significant amount of elastic and quasi-elastic distortion which tend to increase the thickness of the plastic if it is allowed to relax. The quasi-elastic distortion

is a tendency for the plastic to continue contracting over a several day span of time. If the thickness of the films is not critical these relaxed films can be restored to their earlier condition by manual stretching just prior to use. For this experiment however it was necessary to calibrate the surface density of the plastic films used as windows extensively, a task which could most easily be done with the windows removed from the detector. This surface density of course depends on the amount of tension which the film is under. In order to achieve thin windows and still have reproducible tension on the windows it was decided to mount the films on thin aluminum frames. The film and its frame then becomes a single unit and were used as such in both the calibration sequence and on the detectors. An added advantage is interchangeability of these framed films. This allows quick replacement of leaky or destroyed windows.

A difficulty arises in that polypropylene is widely used as a release agent because most glues do not bond well to this plastic. It was found that Resiweld #7004 an epoxy manufactured by the H B Fuller Company provided an adequate if not outstanding bond. The frames used were machined out of 0.064 cm (0.025 inch) thick aluminum (7075 alloy) and provided adequate

support for 11 cm x 23 cm films ≈.00013 cm thick. The process used to transfer the films from the stretched configuration on the end of the tube to their final position on the frames was as follows: The stretched film was held in its stretched configuration by providing a constant tension on the ring. While in this configuration the carbon was carefully removed with a kleenex moistened with methol alcohol. When the film was clean a transfer frame slightly larger than the final frame was glued to the film using rubber cement. When the rubber cement had dried the tension was released from the rings and they were passed back over the transfer frame lifting it and the film from the tube. The excess film was then carefully trimmed from the transfer frame using a sharp pair of scissors. The final frame, having been previously deburred and sanded smooth, was painted very thinly with Resiweld epoxy mixed in the 1:1 "hard" ratio. The transfer frame was located with respect to the final frame and lowered onto the epoxy. A lucite rectangle was then placed on the final frame so as to apply pressure to the polypropylene-Resiweld-aluminum bond. This rectangle did not apply any pressure to the unsupported film inside the final frame because of the thickness of this frame. The lucite rectangle was then weighted and the assembly was left undisturbed until

the Resiweld was cured (at least 5 hours). After the Resiweld was cured the transfer frame was cut away from the final frame and the excess film was trimmed from the final frame.

The film on the frame was mounted in the detector so that an "o"-ring seal pressed on the film side of the frame (see figure 4). The transfer frame and lucite plate were designed so as to allow the "o"-ring seal to rest entirely on the polypropylene film providing an additional sealing force. Placing the film side of the frame toward the detector meant that the film needed to bow outward from the detector the thickness of the window frame, 0.064 cm (0.025 inch), before it was supported by the egg-crate collimators. No difficulties were experienced in having the film bow outward this amount.

APPENDIX D : PROCEDURE FOR INVERTING STRIP SCANS OF CYGNUS LOOP TO OBTAIN TWO-DIMENSIONAL MAP OF X-RAY EMISSION

Two detectors, A and B, having fan-beam collimators with a $0.4^{o} \times 9.8^{o}$ FWHM field of view, each scanned across the Cygnus Loop 4 times. For each detector one of these scans was redundant in the direction of scan so that the Cygnus Loop was scanned in six different directions. The data obtained during these six scans was used to obtain the two-dimensional mapping of the Cygnus Loop.

The direction of the fan beam for detector A was normal to that of detector B so the two fan beams together formed an "X" response pattern on the sky. In addition the centroid of the collimator response pattern for detector A was slightly displaced on the sky from that of detector B. Hence it was necessary to treat each detector separately. A superscript A or B will be used to distinguish the quantities defined for each detector. The observations were divided into 1-second intervals. The observed quantities are the number of counts received in each 1-second interval of time by each detector, F_k^m for m=A,B and k=1 to 130. These data have been displayed in figure 9.

The calculations were simplified by transforming

from astronomical coordinates (α,δ) to a cartesian coordinate system (x,y). The origin of this cartesian system was taken to be $\alpha(1971.8)=20^h\ 50^m$ and $\delta(1971.8)=30.5^\circ$. The tranformation was accomplished in two steps. First the astronomical coordinates (α,δ) were transformed into the polar coordinate system (θ,ϕ) defined so that the region of sky of interest was centered at $\theta=90^\circ$ and $\phi=0^\circ$ and so that the great circle $\phi=0^\circ$ was a line of constant right ascension. Next the realization was made that the coordinate system defined by $x=-\phi$, $y=90-\theta$ is locally cartesian in the region of interest. Since all of the significant strip scans of the Cygnus Loop were made at positions less than 4° removed from the origin this cartesian approximation was quite accurate.

The aspect solution gave the orientation of each detector's collimator as a function of time. The angular response of each collimator was calibrated before the flight. Hence the transmission of each detector's collimator, $\eta^m(x,y,t)$ m=A,B , to x-rays coming from the position (x,y) as a function of time could be determined. Since the collimators used on detectors A and B were fan-beam collimators having fields of view 9.8° x 0.4° FWHM, at any particular time t the functions $\eta^m(x,y,t)$ were zero for most values of x and y. Only for those values of x and y which were inside the

collimators' fields of view at the time t were the functions $\eta^m(x,y,t)$ non-zero. A substantial time-savings was realized in the computations discussed below by treating only those values of x and y for which the $\eta^m(x,y,t)$ were non-zero at each time t.

If s(x,y) represents the actual intensity of x-rays coming from the location (x,y) then the number of x-rays entering the detector in the kth 1-second interval will be:

$$F_k^m = \iint_{\substack{\text{collimator} \\ \text{field of view}}} s(x,y) \int_{139+k}^{140+k} \eta^m(x,y,t)\, dt\, dx\, dy$$

For calculation purposes the region of the x,y plane of interest was divided into 0.5^o x 0.5^o cells. The region of interest was 69 cells wide in both directions, giving 4761 cells total, and covered approximately the celestial region $\alpha(1971.8)=22^h 4^m$ to $\alpha=19^h 36^m$ and $\delta(1971.8)=12.5^o$ to $\delta=49^o$. The double integral over x and y could then be approximated by a double sum;

$$F_k^m = \sum_{i,j} S_{ij} \int_{139+k}^{140+k} \eta_{ij}^m(t)\, dt\, \Delta x\, \Delta y$$

where S_{ij} is the average source intensity in the i,jth cell and $\eta_{ij}^m(t)$ is the average value of $\eta^m(x,y,t)$ for the i,jth cell. The sum is over all values of i and j

for which $\eta^{m}_{ij}(t)$ is non-zero in the time interval in question. The quantities involved in the integral over time can all be calculated. Performing the integral gives the quantities H^{m}_{ijk} defined by:

$$F^{m}_{k} = \sum_{ij} S_{ij} H^{m}_{ijk}$$

where the sum is over all i and j for which H^{m}_{ijk} is non-zero. The observations give the values F^{m}_{k} for m=A, B and k=1,...,130 . From the aspect solution and the known angular response function the values H^{m}_{ijk} can be calculated. The solution proceeds by assuming values for the S_{ij} and modifing these values in an iterative manner until the predicted values f^{m}_{k} agree with the observed F^{m}_{k} . All of the values S_{ij} were initially assumed to be zero. This initial source function is labeled S_{ij0} for convience. The iteration began with detector A for the time period 140 to 141 sec, i.e. k=1, and calculated the predicted number of counts f^{A}_{1} according to:

$$f^{A}_{1} = \sum_{ij} S_{ij0} H^{A}_{ij1}$$

This predicted value did not agree with the observed value since all the S_{ij0} were zero. So a correction was applied to the values S_{ij0} to bring f^{A}_{1} into agreement with

F_1^A. This correction modified the S_{ij0} according to how much they were sampled by the angular response function for detector A's collimator, H_{ij1}^A. The modification was given by:

$$S_{ij1} = S_{ij0} + Q_1 \, (F_1^A - f_1^A) \, H_{ij1}^A$$

where

$$Q_1 = \left(\sum_{ij} (H_{ij1}^A)^2 \right)^{-1}$$

and where all sums are over all i and j for which H_{ij1}^A is non-zero.

The S_{ij1} are the source values required to give the observed value F_1^A. These source values were then used to obtain a predicted value f_2^A. In a way entirely analogous to that given above the values S_{ij1} were modified to give agreement between the values f_2^A and F_2^A. This gave the values S_{ij2}. This process was continued through the 128 remaining 1-second intervals of detector A and the source values S_{ij130} were obtained. These served as the initial values for the 1st time interval of detector B. After iterating through the 130 1-second intervals of detector B the values S_{ij260} were obtained. These values were used as the initial values for the 1st time interval of detector A and the process was continued until the source values converged.

These convergent values are labeled $\bar{S}_{ij}$.

The routine was tested on a trial source distribution consisting of a single source cell being non-zero and the rest zero. The expected response f_k were generated for six scans across the source and then these f_k were inverted by the above technique to arrive at the source values $\bar{S}_{ij}$. The $\bar{S}_{ij}$ obtained reproduced the original function to within a small fractional error attributable to the inaccuracies involved in the integration scheme used to obtain the H_{ijk}.

The rate of convergence of this iterative process depends on the collimator response functions and on the number of scans taken across the field of interest. It is straightforward to show that two scans are insufficient to reveal the source distribution. Three scans are sufficient but only if each passes relatively close to the source center. To ensure that sufficient redundancy was present the Cygnus Loop was scanned in six different directions. The convergence of the source values for most of the Cygnus Loop proved to be quite rapid. Ten passes through the 260 data points yielded essentially the final distribution for these regions. However the convergence of some small regions of the map was much slower. By considering the 3 scans by each detector separately it was found that these regions were those which were most

poorly sampled by the detectors. These small regions had the form of "wings" to the northeast and to the west of the Loop. The observed convergence of these "wings" and the data points themselves as examined below both support the instrumental rather than real nature of these "wings". Therefore the convergence of these small regions was aided by resetting these "wings" to zero after 10 passes through the data and another 10 passes were taken through the data. The "wings" returned at a much lower level so the process was repeated. After another ten passes (making a total of 30 pases) through the 260 data points the wings were no longer visible. The $\overline{S}_{ij}$ obtained have been displayed above in figure 3 and in Table 3.

The consistency between these $\overline{S}_{ij}$ and the observed data was verified in several ways. First, the resulting source field is essentially zero except in two regions representing the Cygnus Loop and Cygnus X-1. These regions are widely separated and easily identified. Cygnus X-1 was seen in only one strip scan by detector A and so a strip source was generated at this location. Because this occured at the turning point of one of the scans (at 197 sec in figure 9) detector B never scanned this region and so the strip source was never reduced to a point source. With the exception of these two sources the region covered by the source field revealed no statistically significant

deviations from zero. The predictions of this source field were compared to the 260 detector response points and a value of χ^2 was generated. This was quite low, being less than 100. Since only some 30 source cells, out of the 4761 total source cells, were statistically different from zero, it seems justified to claim that the low value of χ^2 has some significance.

Secondly, simultaneously but independently, another method was used to obtain a source distribution. This was simply to guess at a source distribution and fold this guess through the collimator response for each second to obtain an expected datum. The deviations between the expected and the actual data points were then used to suggest a new source distribution. This is an iterative scheme which differs from the iterative scheme given above only in that the iterations occur after an entire pass through the data and the iterations are determined by an intuitive, guess and err, approach rather than by a mathematical expression. This approach is of course highly subject to the experimenter's preconceptions. However the rough source distribution obtained in this way was vindicated in every essential point by the source distribution obtained through the other technique. The mathematically governed iteration should be quite free of bias and is felt to give an accurate

picture of the x-ray structure of the Cygnus Loop.

An examination of the observed data is useful as an example of the intuitive approach and also to show how the observations alone limit the extent of the Cygnus Loop to the region of sky displaying Hα emission. Figure 32 shows the x-ray extent of the Cygnus Loop as determined directly from the observations. An example of how this extent is derived from the observations is provided by detector B for the time intervals 205 to 206 sec and 214 to 215 sec. These are the intervals numbered 1 and 2 in figure 32. These two abrupt changes in the counting rate of detector B give the two extent limit lines marked 1 and 2 in figure 32. In obtaining these extent limits no attempt was made to correct for the triangular response of the collimators. Hence the limits shown should be regarded as being $\sim 0.2^{o}$ wide. For clarity of presentation not all of the scans of the Cygnus Loop were used to give extent limits. In general figure 32 depicts extent limits only for those scans having the highest signal to noise ratios. For those scans having signal levels comparable to the noise level the points where the Cygnus Loop is first and last detected cannot be as accurately obtained as for the high signal level scans. However these low signal level scans substantially agree with the extent limits determined from the higher signal level scans. The

Figure 32. The x-ray extent of the Cygnus Loop as determined directly from the observations. This figure is the same as figure 9 except for the lines indicating the limits of the x-ray extent of the Cygnus Loop. The data points used to obtain these extent limits are identified by the number appended to each extent line.

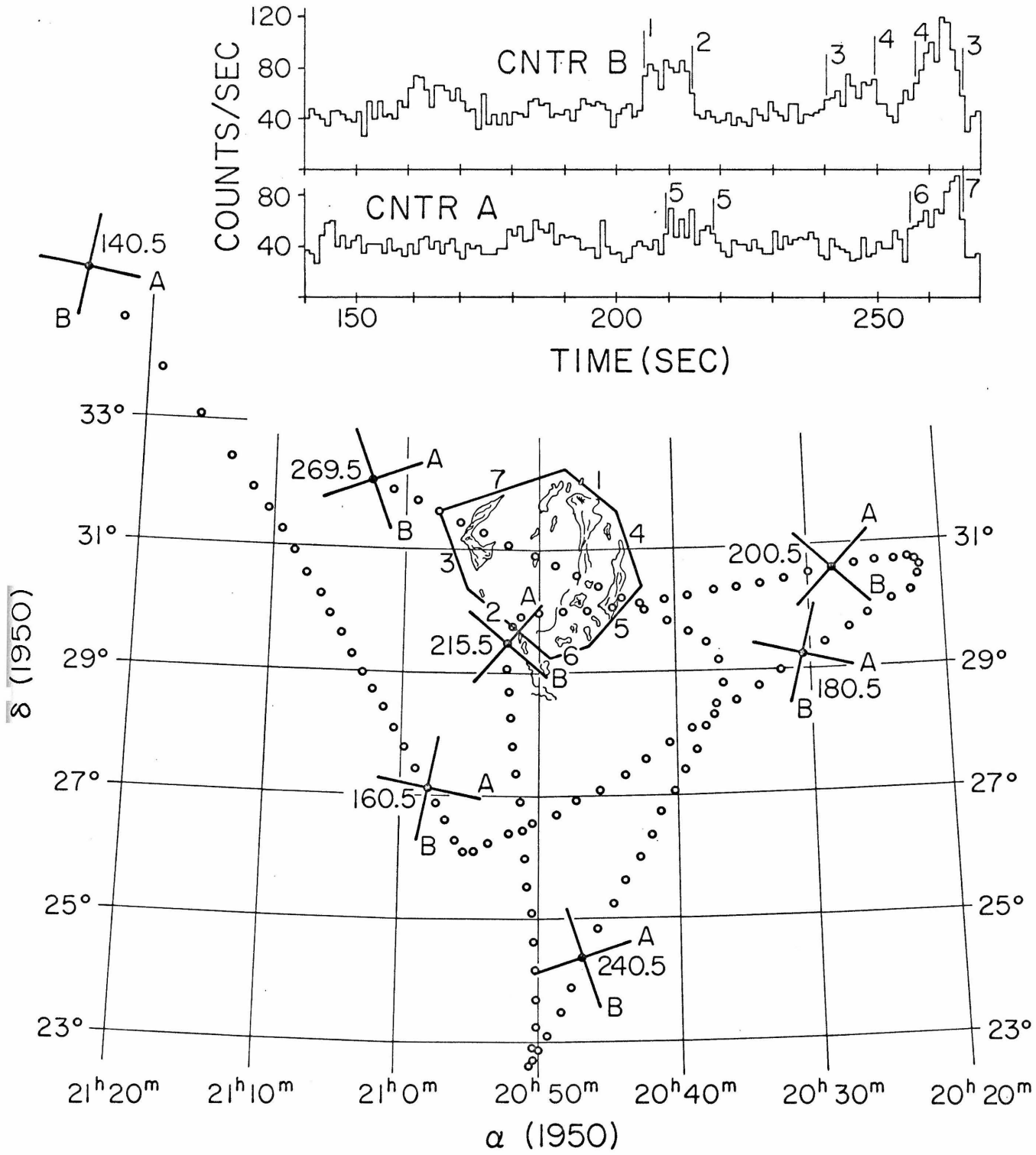
120
80
40
COUNTS/SEC
CNTR B
CNTR A
150
200
250
TIME (SEC)
140.5
269.5
215.5
160.5
240.5
200.5
180.5
A
B
33°
31°
29°
27°
25°
23°
δ (1950)
21h20m
21h10m
21h0m
20h50m
20h40m
20h30m
20h20m
α (1950)

Figure 32

data clearly indicate that the x-ray extent of the Cygnus Loop is closely restricted to the optical extent. The internal structure is more difficult to obtain by this type of intuitive reasoning. To obtain this internal structure some form of iterative process such as those described above must be used.

APPENDIX E : REDUCTIONS OF THE FILTERED MEASUREMENTS OF THE CYGNUS LOOP SPECTRUM

In section IV the fluxes between .25 and 2.5 kev observed by detector D during its filtered measurements were obtained. These fluxes, because of the filters, must have come from one of several narrow ranges of energies. This is made more obvious in figures 33 and 34 where the detector efficiency of detector D with each of its filters is shown. These figures show that the efficiency of the detector is limited to rather narrow intervals in energy. The detector resolution was comparable to the spacings in energy of these intervals of increased detector efficiency. For detector D the resolution was ~0.27 kev FWHM at 0.28 kev, ~0.37 kev at 0.53 kev and ~0.43 kev at 0.69 kev. Hence the two bands of detector efficiency at ~0.28 kev and ~0.53 kev for the detector with the oxygen filter gave spectral distributions which strongly overlaped. Also, since the spectrum of the Cygnus Loop falls rapidly with increasing energy (see Appendix F) the contribution to the observed spectrum resulting from the increased detector efficiency band from 0.8 kev to 3.0 kev (for the detector with the oxygen filter) appeared as a small bump on the spectral distributions resulting from the other two increased detector

Figure 33. Efficiency of detector D with oxygen filter. Curve a is for detector D window, i.e. for a 2.5 cm thick detector filled with methane gas at 150 torr and 20°C with 270 $\mu gm/cm^2$ of polypropylene window material and with 390 $\mu gm/cm^2$ O_2 gas filter. Curve b is for detectors D middle and D side and was calculated using the same parameters as for curve a except that 2.5 cm of methane gas at 150 torr and 20° C was introduced as an attenuator. This represents the absorption due to detector D window (see figure 4). The absorption coefficients used in calculating these efficiency curves were taken from Henke et al (1967).

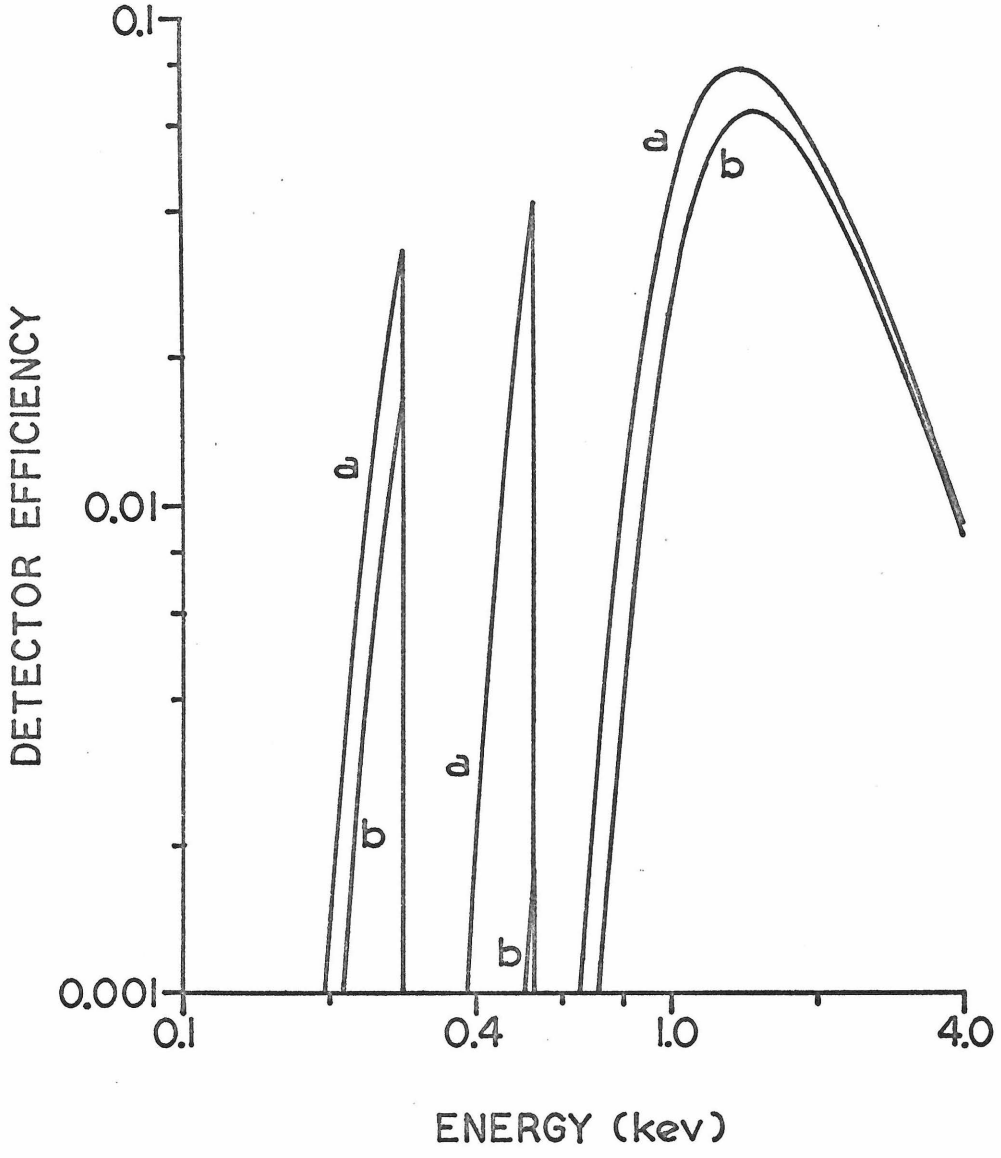
0.1
0.01
0.001
DETECTOR EFFICIENCY
a
b
a
b
a
b
0.1
0.4
1.0
4.0
ENERGY (kev)

Figure 33

Figure 34. Efficiency of detector D with teflon filter. These efficiency curves also include the absorption due to the oxygen remaining in the gas cell (see section II) because of the gas cell's slow bleed rate. This oxygen causes the drop in efficiency seen for the teflon filter at 0.53 kev. Curve a is for detector D window i.e. for a 2.5 cm thick detector filled with methane gas at 150 torr and 20° C with 270 $\mu gm/cm^2$ of polypropylene window material and with 57 $\mu gm/cm^2$ O_2 gas and 670 $\mu gm/cm^2$ teflon sheet as filters. Curve b is for detectors D middle and D side and includes the absorption due to detector D window.

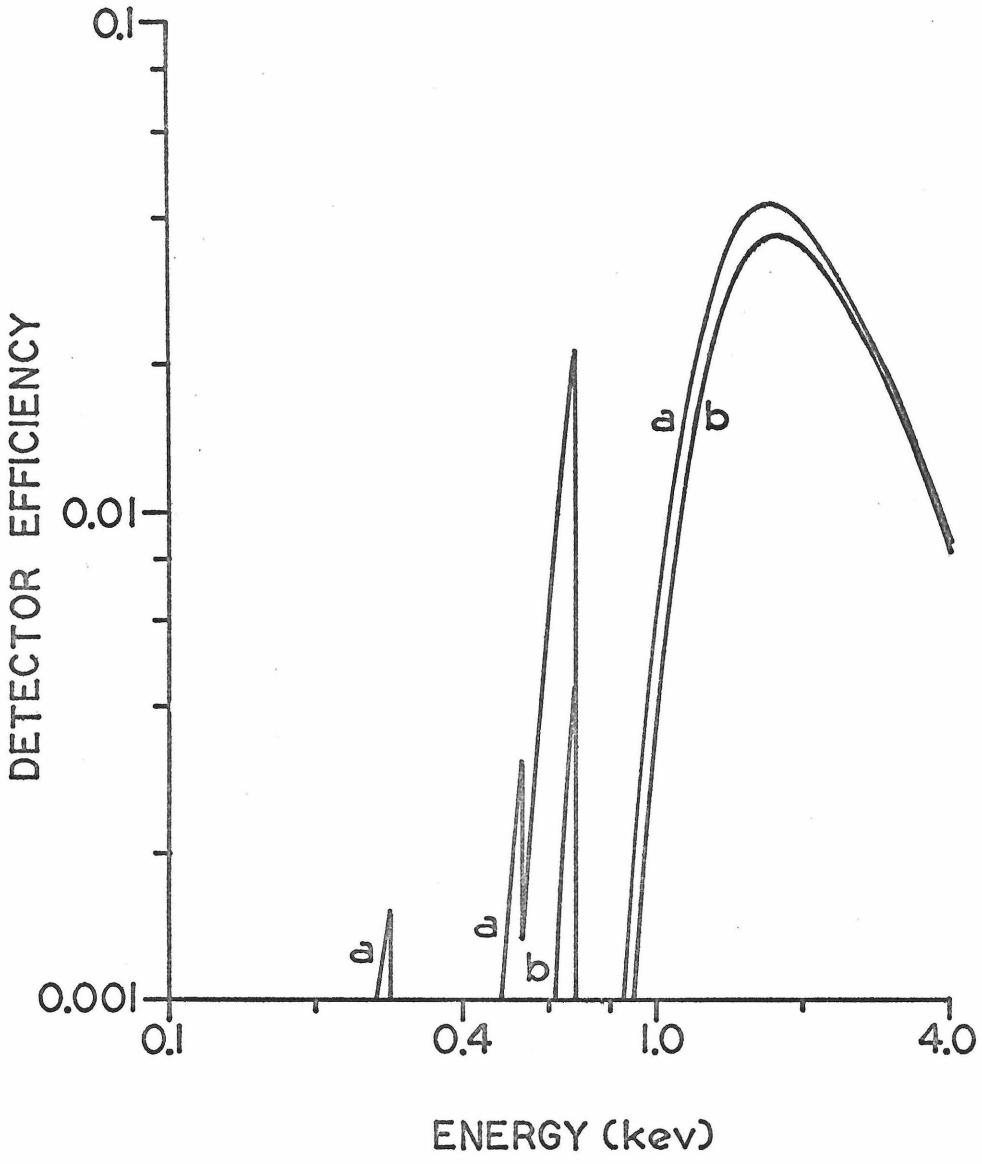

Figure 34

efficiency intervals. Thus this relatively poor detector resolution when coupled with the low statistical accuracy of the data made it very difficult to directly determine the contribution of each energy interval to the observed spectrum. A similar situation prevailed for the detector with the teflon filter. So the x-ray flux between 0.53 and 0.69 kev, for example, was not directly obtainable from the spectrum observed by the detector with the teflon filter. Only for the combined middle and side detectors using the oxygen filter (see figure 33 curve b) was the separation in energy of the bands sufficient to allow relatively unambiguous determination of the contributions of each detector band (see below). For the other three filtered measurements it was necessary to use the usual procedure of reducing spectra (Gorenstein et al, 1968). This process consists of assuming a trial spectrum and folding this spectrum through the detector's efficiency curve. The resultant spectrum is then modified according to the detector's resolution function. This final spectrum is compared to the observed spectrum. The comparison is used to suggest modifications to the trial spectrum and the process is repeated until agreement between the predicted and observed spectrum is achieved. In its usual form the comparison is between spectra rather than between integrated counting rates. This procedure was

tried using the observed spectra but the poor statistics did not permit a valid comparison. It was found that the trial spectrum which gave the best agreement with the observed spectrum was rather strongly dependent on the energy intervals used in the spectrum determination. This unphysical result was attributed to the low statistical accuracy of each of the spectral points. Hence it was decided to compare the integrated fluxes from 0.25 to 2.5 kev rather than the detailed spectra. The lower end of this energy range was determined by the threshold for signal acceptance of the detector electronics. The upper end was determined from the observed spectrum to be the largest energy for which the signal level was still above the noise level. Comparison of the spectra obtained by the combined middle and side detectors and the window detector for each filter permitted a differential measurement of the contributions of each of the regions of increased detector efficiency. In this way the amount of x-ray emission in each energy band could be unambiguously determined. This is done below. The trial input spectra were chosen on the basis of the continuum spectra which best satisfied the unfiltered measurements of detectors C and D discussed in Appendix F. The unfiltered measurements indicate that the trial spectra should be thermal bremsstrahlung spectra with the functional form:

$$\frac{dN}{dE} = \frac{A}{E} e^{-E/kT} e^{-\sigma_{BG} N_H} \quad \text{photons/cm}^2\text{-sec-kev}$$

where the term involving σ_{BG} represents the effects of interstellar absorption for a columnar density of N_H hydrogen atoms per cm^2. σ_{BG} is the absorption coefficient of the interstellar medium given by Brown and Gould (1970). Based on the results of the unfiltered measurements the values of kT and N_H given in Table 17 were assumed as trial spectra.

The value of A was initially assumed to be 10.0 for each trial spectrum. For this value of A an expected detector counting rate was obtained by folding each trial spectrum through the detector's efficiency curve and multiplying by the effective area of detector D,

TABLE 17

SPECTRAL PARAMETERS OF TRIAL SPECTRA

Spectra#	kT(kev)	$N_H \times 10^{-20}$
1	.23	5.8
2	.24	5.2
3	.26	4.5
4	.28	3.9

395 cm^2. The convolved spectrum was then summed over observed energies from 0.25 to 2.5 kev taking the detector's

resolution into account. This predicted detection rate was then compared with the actual observed rate and the value of A was adjusted to bring the expected and observed results into agreement. The values of the continuum level, A, obtained in this way are given in Table 18.

TABLE 18.

CONTINUUM LEVELS CONSISTENT WITH FILTERED MEASUREMENTS

Detector	Filter Material	Continuum level (A) for trial spectra # 1	2	3	4
Window	Oxygen	185 ± 17	157 ± 14	119 ± 11	93 ± 8.5
M + S*	Oxygen	184 ± 28	147 ± 22	105 ± 16	77 ± 12
Window	Teflon	350 ± 60	290 ± 50	210 ± 40	165 ± 30
M + S	Teflon	270 ± 90	210 ± 80	150 ± 50	106 ± 37

*M + S = Middle + Side

The values given in Table 18 clearly indicate an excess counting rate for the teflon filtered measurements over that expected from a simple thermal bremsstrahlung spectral form. This excess can be shown to be limited to the region of enhanced detector efficiency below 0.69 kev by the following chain of logic. The oxygen filtered detector samples essentially three energy bands, 0.25 to 0.28 kev, 0.44 to 0.53 kev and 0.80 to 3.0 kev. The window and middle + side layers of the oxygen filtered detector allow a differential measure of

the flux in the oxygen band-pass region from 0.44 to 0.53 kev and to a lesser extent a differential measure of the relative contributions of the other two energy bands sampled. The agreement between the continuum levels obtained for the window and middle + side detectors using the oxygen filter implies that the flux obtained in the energy range 0.44 to 0.53 kev is also consistent with this continuum level. The consistency of the continuum levels in the other two energy ranges sampled is assured partially by the observed spectral distribution of the counts received and also by the results of the measurements made by the unfiltered detectors. Any large discrepancy in the continuum levels of these two energy intervals would have been visible in the spectral distribution of the counts received, either in the filtered measurements or, in the unfiltered measurements, and no such discrepancy was observed. For the oxygen filtered combined middle and side detectors it is possible to make a separation of the observed counts into two energy ranges, 0.25 to 0.6 kev and 0.6 to 2.5 kev and from this split show that the continuum levels in the two energy ranges 0.25 to 0.28 kev and 0.8 to 3.0 kev are consistent. The results obtained are not particularly sensitive to the energy, 0.6 kev, chosen for this division. Varying this energy as much as 100 ev in either direction does

not make a statistically significant change in the results. These results are shown in Table 19 for the same spectral models as previously assumed.

TABLE 19

MEASUREMENTS OF CONTINUUM LEVEL BY OXYGEN FILTERED MIDDLE + SIDE DETECTOR

Energy Range (kev)	Continuum Level A for Trial Spectra# 1	2	3	4
0.25 to 0.6	147±54	116±42	87±32	68±25
0.6 to 2.5	204±32	165±26	114±18	82±13

As advertised the results show that the continuum level is the same for the two energy intervals 0.25 to 0.28 kev and 0.8 to 3.0 kev. Since the teflon filtered detector samples essentially only two energy intervals 0.5 to 0.69 kev and 0.9 to 2.5 kev and since the latter energy range is included in the ranges sampled by the oxygen filtered detector, it becomes apparent that the excess flux causing the higher continuum level value for the teflon filtered measurement must come in the energy range 0.53 to 0.69 kev.

Assuming that the continuum level is as determined by the oxygen filtered detector the excess flux observed in the fluorine band-pass below 0.69 kev can be determined by folding this continuum level through the detector

response to obtain an expected rate. This expected rate is then subtracted from the observed rate to give the excess flux observed. For this reduction the continuum levels obtained for the window, middle and side oxygen filtered detectors were combined to give a single value. This value is given in column 3 of Table 20. Also given in this Table is the excess flux observed and the line intensities derived from this excess flux. The excess flux is the difference between the observed rate of .066 ± .012 cnts/sec-cm^2 and the expected rate. These line intensities are the intensities which would be required to give the observed excess flux assuming only one of the two lines is present. The values for the line intensities were obtained by dividing the observed excess flux by the detector efficiency at the line's energy. The detector efficiencies used were .0172 @ 658 ev and .0044 @ 575 ev. The expected rates and hence the excess fluxes are the same for all four spectral models because the ratio of the efficiency of the detector with oxygen filter to the efficiency of the detector with teflon filter is, to a good approximation, independent of the spectral model for the models considered here.

The line intensities given in Table 20 were calculated assuming that a single line at 575 ev (or

TABLE 20

EXCESS FLUX OBSERVED (0.5 to 0.69 kev) DURING FILTERED MEASUREMENTS

SPECTRAL PARAMETERS		CONTINUUM LEVEL	EXPECTED RATE*	EXCESS FLUX OBSERVED AT EARTH	LINE INTENSITY† (photons/sec-cm^2)	
kT(kev)	$N_H \times 10^{-20}$	A	(cnt/sec-cm^2)	(cnts/sec-cm^2)	@658ev	@575ev
.23	.58	185 ± 15	.035 ± .003	.031 ± .012	1.8±0.7	7.0±2.8
.24	.52	154 ± 12	.035 ± .003	.031 ± .012	1.8±0.7	7.0±2.8
.26	.45	114 ± 9	.035 ± .003	.031 ± .012	1.8±0.7	7.0±2.8
.28	.39	88 ± 7	.035 ± .003	.031 ± .012	1.8±0.7	7.0±2.8

*Expected rate for window layer teflon filtered detector

†Assumes entire excess flux is in either 658 line or 575 line

alternately at 658 ev) accounted for the entirety of the excess flux. There is no reason not to suspect that both lines are present at levels lower than those given in Table 20 and that these lines combine to give the observed excess. That is, the line intensities obtained are linear in the sense that if they are labeled I(575) and I(658) and if p is the fractional value of I(575) present with $0 \leqslant p \leqslant 1$ then any combination of the two lines given by the expression

$$I(575) \times p + I(658) \times (1-p)$$

is also consistent with the measurements.

APPENDIX F : REDUCTIONS OF THE UNFILTERED MEASUREMENTS OF THE CYGNUS LOOP SPECTRUM

Section IV gives the procedure whereby the observed spectra were corrected for background and instrumental effects. The spectra obtained by the six detectors C window, C middle, C side, D window, D middle and D side are shown in figures 35, 36, 37 and 38. The errors in these figures represent statistical errors only.

In general it is not possible to rigorously invert such spectra and obtain a unique spectrum for the source. The standard approach (Gorenstein et al, 1968) is to assume an input spectrum attenuated by a certain depth of interstellar gas and fold this through the detector efficiency and resolution to obtain a predicted spectrum. This predicted spectrum is then compared with the observed spectra using the χ^2 criterion to test for significance of agreement.

The trial source spectra were functionally:

1) Thermal Bremsstrahlung Spectrum with Line Emission -

$$\frac{dN}{dE} = \left[\frac{A}{E}\exp\left(\frac{-E}{kT}\right) + I(658)\delta(E-.658) + I(575)\delta(E-.575)\right] \cdot \exp(-\sigma_{BG} N_H) \quad \text{photons/cm}^2\text{-sec-kev}$$

Figure 35. The Cygnus Loop spectrum observed by detector C window. The extent of the vertical bars gives $\pm 1\,\sigma$, where σ is the statistical error in the measured value. The horizontal bars give the extent of the measured point in energy. The data are plotted with the vertical scale split in order to show the small errors more clearly.

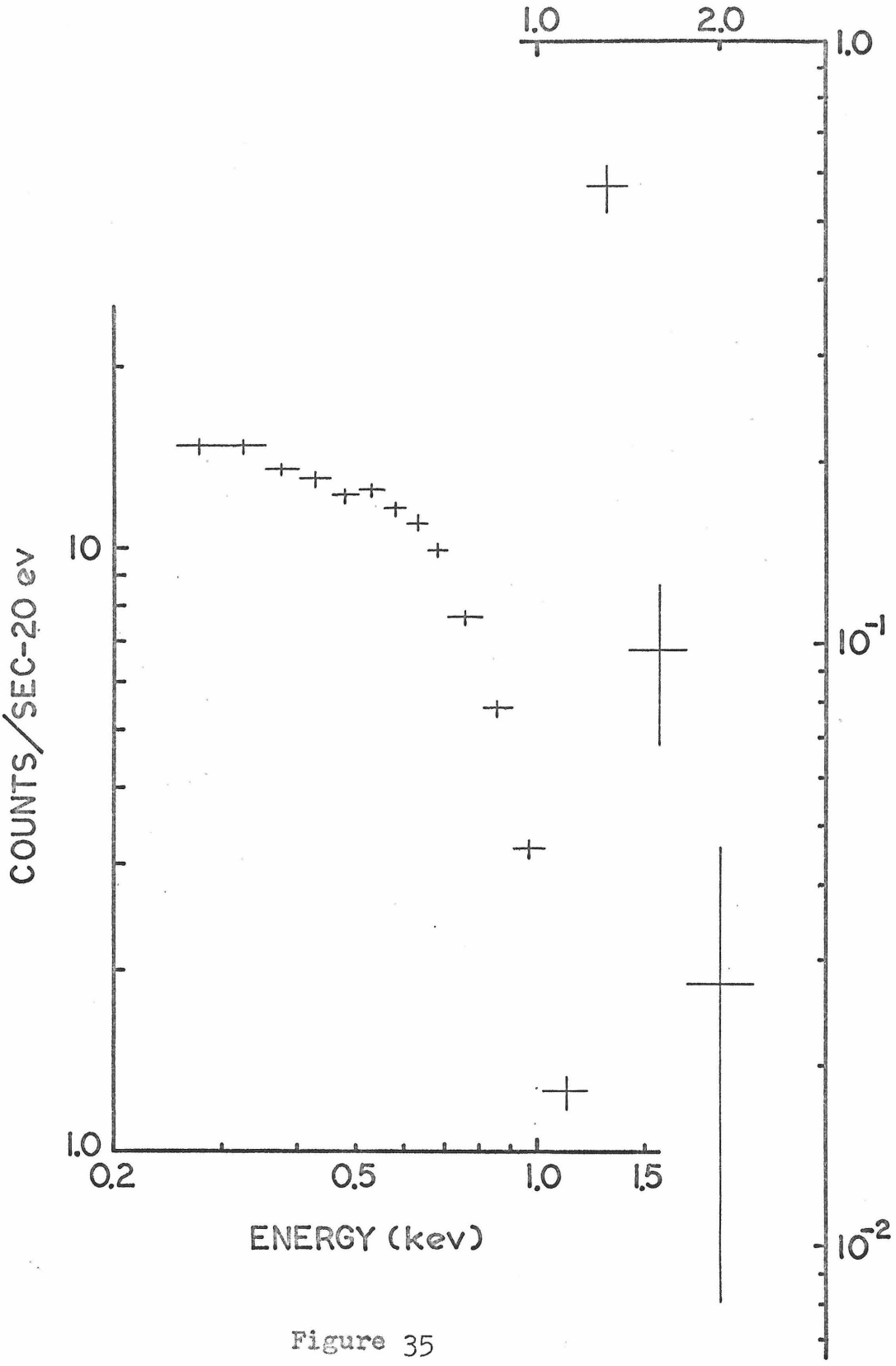

Figure 35

Figure 36. The Cygnus Loop spectra observed by detectors C middle (CM) and C side (CS).

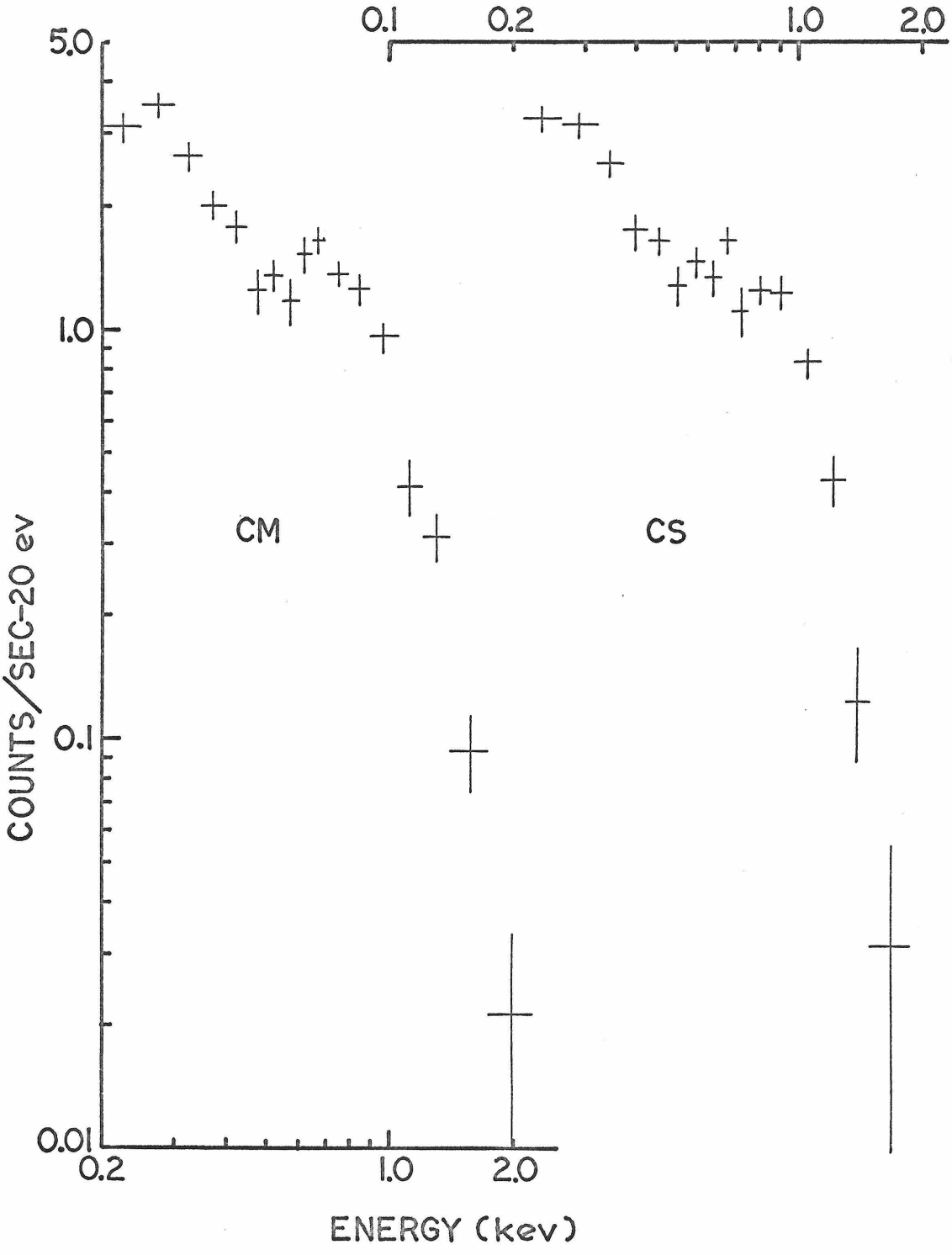

Figure 36

Figure 37. The Cygnus Loop spectrum observed by detector D window. The data are plotted with the vertical scale split in order to show the small errors more clearly.

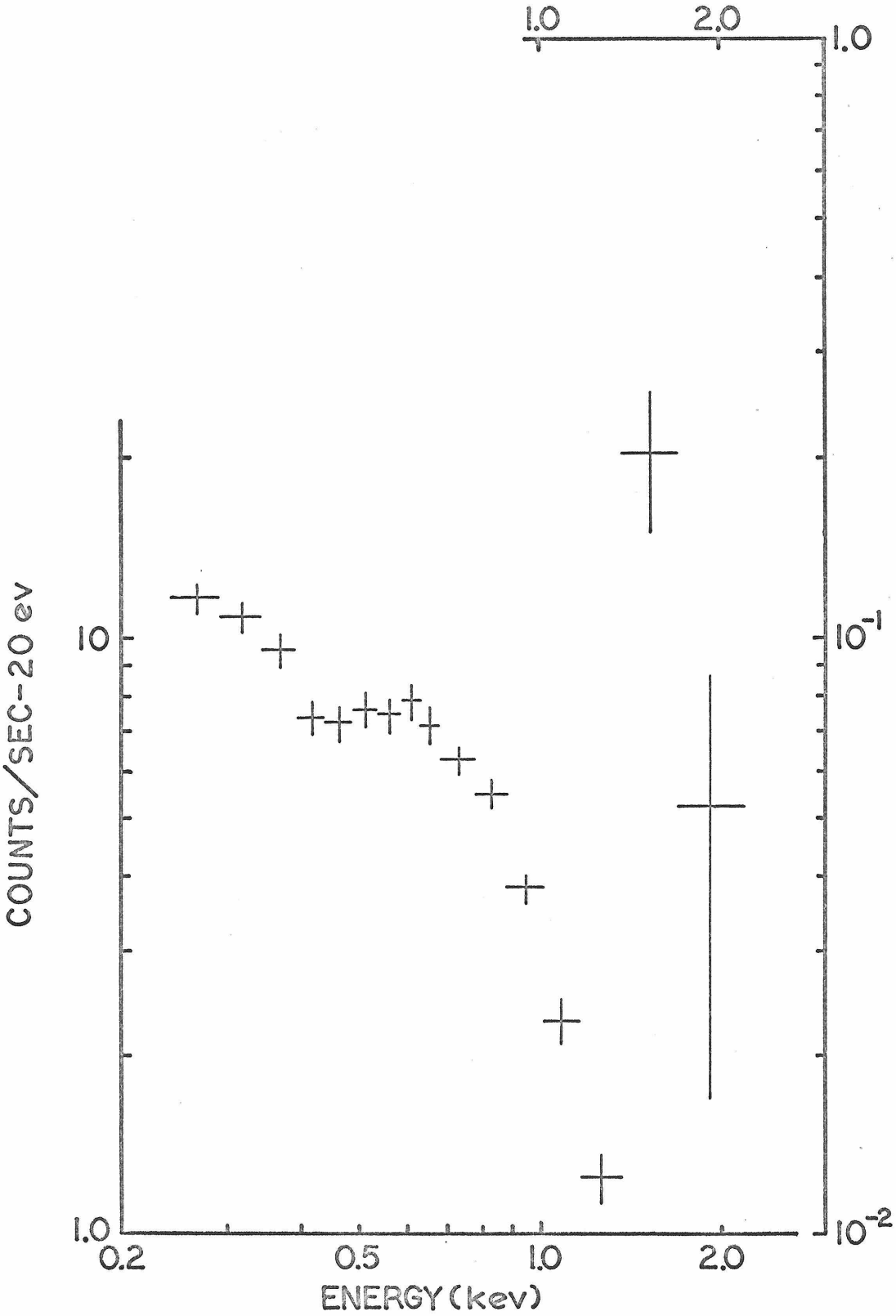

Figure 37

Figure 38. The Cygnus Loop spectrum observed by detectors D middle (DM) and D side (DS).

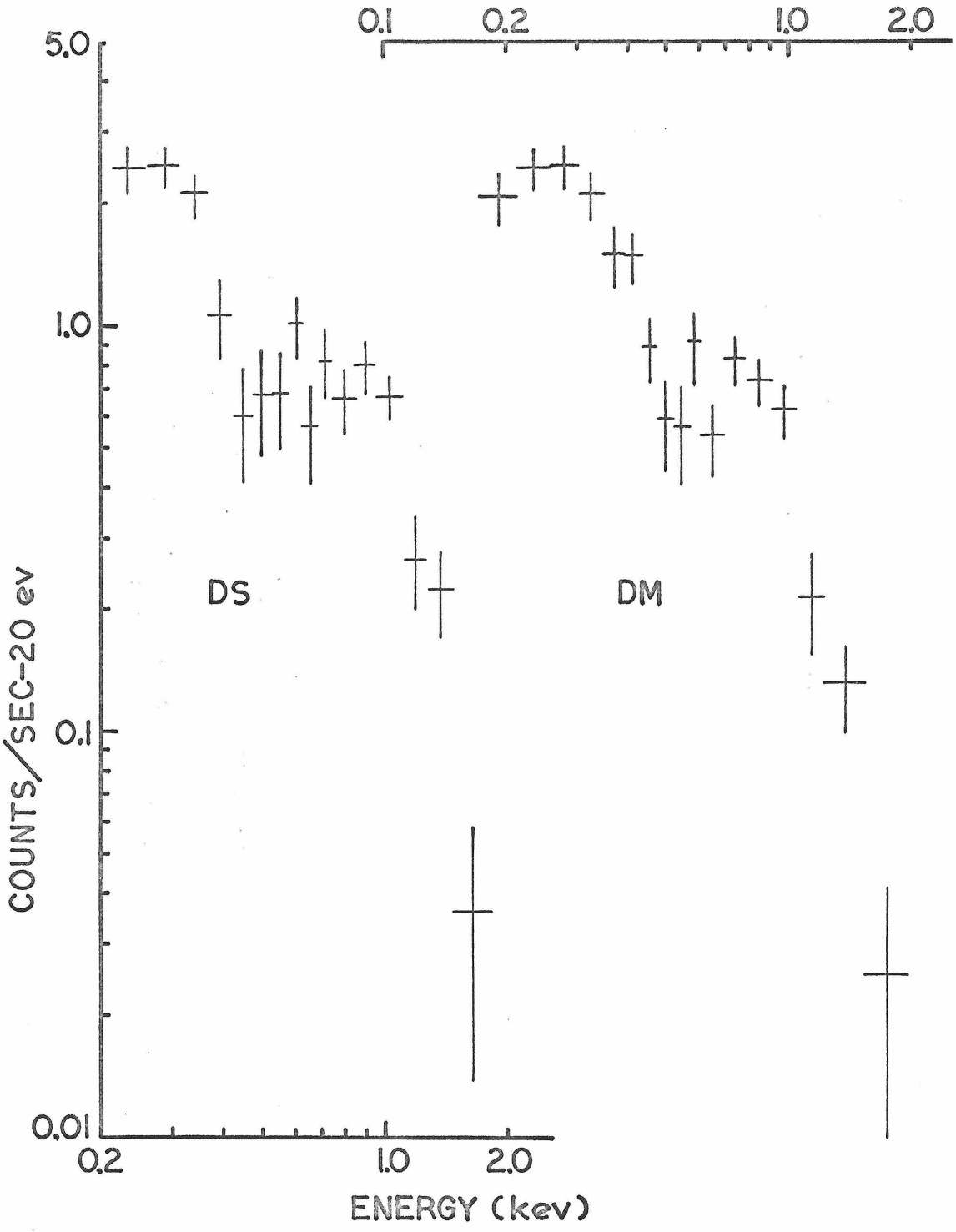

Figure 38

2) Thermal Bremsstrahlung Spectrum -

$$\frac{dN}{dE} = \frac{A}{E} \exp\left(-\frac{E}{kT} - \sigma_{BG}\, N_H\right) \qquad \text{photons/cm}^2\text{-sec-kev}$$

3) Power Law Spectrum with Line Emission -

$$\frac{dN}{dE} = \left[AE^{-\alpha} + I(658)\delta(E - .658) + I(575)\delta(E - .575)\right] \exp(-\sigma_{BG} N_H) \qquad \text{photons/cm}^2\text{-sec-kev}$$

4) Power Law Spectrum -

$$\frac{dN}{dE} = AE^{-\alpha} \exp(-\sigma_{BG}\, N_H) \qquad \text{photons/cm}^2\text{-sec-kev}$$

where σ_{BG} and N_H are as defined above

kT is the temperature in kev

A is the continuum intensity

I(658) & I(575) are the line intensities @658 and 575 ev respectively

α is the power law index

The thermal bremsstrahlung model represents a simple approximation to the free-free continuum emission expected from a hot plasma. The power law model can represent a variety of theoretical models; inverse compton emission, synchrotron emission, or even a combination of the free-free emission from several

plasmas of different temperatures (see section VI).

These trial source spectra involve free parameters which are varied until the best fit to the observed spectra is achieved. The χ^2 test is used as the criterion for judging accuracy of fit and also as a means of estimating the statistical accuracy of the spectral parameters obtained. If χ^2_{min} is the minimum χ^2 obtained when the parameter p assumes the value p_o then the standard deviation of p_o is σ such that the values $p_o \pm \sigma$ give a χ^2 of $\chi^2_{min} + 1$. So for each spectral parameter a statistical error is also obtained by the fitting process.

The best fit values of the spectral parameters involved in these models and their statistical errors are given in Tables 21, 22, 23 and 24 for each of the six detectors. In these Tables a shorthand notation for the detectors has been adopted; W, M and S stand for window , middle and side respectively. So detector C window becomes CW and so forth.

The electronics which sampled the energies of the x-rays had a finite sampling rate. This resulted in a reduction in the observed counting rate or equivalently in the introduction of a characteristic deadtime to be associated with each recorded x-ray energy. In addition the angular response of the collimators also reduced the

TABLE 21

BEST CYGNUS LOOP SPECTRUM FOR EACH DETECTOR

THERMAL BREMSSTRAHLUNG SPECTRUM + LINE EMISSION

Detector	A	kT (kev)	$N_H \times 10^{-21}$ (atoms/cm^2)	I(658) (photons/cm^2-sec)	I(575) (photons/cm^2-sec)	χ^2	DOF*
CW	190	.240±.003	.49±.01	0.5±0.2	.02± .03	9.3	9
CM	120	.253±.006	.47±.02	0.6±0.3	3.0 ±0.9	16.9	10
CS	130	.251±.005	.49±.02	0.0±0.1	4.1 ±0.9	21.1	10
DW	150	.271±.006	.46±.01	0.0±0.1	2.4 ±0.8	13.7	9
DM	130	.225±.009	.45±.03	1.7±0.6	0.0 ±1.8	12.5	10
DS	120	.251±.010	.47±.03	0.6±0.7	0.9 ±2.1	14.4	9

*DOF: degrees of freedom in χ^2 test

TABLE 22

BEST CYGNUS LOOP SPECTRUM FOR EACH DETECTOR

THERMAL BREMSSTRAHLUNG SPECTRUM

Detector	A	kT (kev)	$N_H \times 10^{-21}$ (atoms/cm^2)	χ^2	DOF
CW	220	.234±.003	.53±.01	15.3	11
CM	200	.232±.004	.58±.02	33.9	12
CS	240	.222±.004	.61±.02	30.2	12
DW	290	.233±.004	.59±.02	16.7	11
DM	200	.214±.006	.55±.03	16.3	12
DS	160	.237±.008	.53±.03	14.9	11

TABLE 23

BEST CYGNUS LOOP SPECTRUM FOR EACH DETECTOR

POWER LAW SPECTRUM + LINE EMISSION

Detector	A	α	$N_H \times 10^{-21}$ (atoms/cm^2)	I(658) (photons/cm^2-sec)	I(575) (photons/cm^2-sec)	χ^2	DOF
CW	2.7	4.37±.03	.88±.01	2.3±0.2	0.0±0.4	27.5	9
CM	2.3	4.42±.04	.96±.02	2.1±0.4	2.6±1.3	17.4	10
CS	2.3	4.43±.04	.96±.02	1.9±0.4	2.7±1.4	30.9	10
DW	4.2	4.67±.04	1.13±.02	0.4±0.5	1.7±1.3	20.9	9
DM	1.6	4.96±.07	1.07±.03	3.0±0.8	0.0±1.7	14.4	10
DS	2.2	4.65±.08	1.06±.03	1.4±1.0	1.2±2.7	16.4	9

TABLE 24

BEST CYGNUS LOOP SPECTRUM FOR EACH DETECTOR

POWER LAW SPECTRUM

Detector	A	α	$N_H \times 10^{-21}$ (atoms/cm^2)	χ^2	DOF
CW	3.6	4.46±.03	1.05±.01	98.4	11
CM	3.0	4.72±.04	1.14±.02	48.7	12
CS	3.0	4.76±.07	1.16±.02	50.2	12
DW	4.6	4.66±.04	1.15±.02	25.2	11
DM	2.0	4.85±.07	1.08±.03	27.1	12
DS	2.5	4.62±.07	1.07±.03	19.5	11

intensity of the observed x-rays. To obtain the intensity of the source these effects must be taken into account. The values of the continuum intensities and of the line intensities given in Tables 21 to 24 have been corrected for these two effects.

A perusal of the results given in Tables 21 through 24 for a particular parameter of a particular model will demonstrate that the values obtained from the various detectors differ by more than is consistent with the statistical errors given. This can be explained in two ways. The first is that there exist systematic effects which have not been correctly accounted for in arriving at the results given. Indeed a careful study of the detector systematics was necessary to reduce the discrepancies between the results given by the various detectors to the level seen in Tables 21 to 24. So it would not be too surprising to discover that additional systematic effects are still present.

The second explanation is that the source spectrum is more complicated than the trial spectra assumed here and that the non-statistical differences seen are a result of the different responses of the various detectors to this complex spectrum. The results presented in section III along with the model proposed in section VI provide support for the inherently complex nature of the

overall spectrum of the Cygnus Loop. Undoubtedly both hypotheses are in part responsible for the differences apparent in these Tables.

Most of the information contained in Tables 21-24 will not be discussed. The discussion below concentrates on those spectral features which seem capable of providing theoretical constraints; the overall shape of the continuum emission and the presence or absence of line emission.

In the discussion following, a spectral model is said to give an acceptable description of the observed data if the obtained χ^2 is within the 90% confidence interval for the appropriate number of degrees of freedom.

Comparing the obtained χ^2 of Tables 21 & 23 and Tables 22 & 24, it is readily apparent that the thermal bremsstrahlung spectrum gives a much better fit to the observed data than does the power law spectrum, both with and without line emission.

Comparison of Tables 21 and 22 shows that the addition of line emission significantly improves the thermal bremsstrahlung model's spectral fit for detectors CW, CM, CS and DM. For DW the fit is uninfluenced and for DS the addition of line emission reduces the significance of the spectral fit. Similarly comparison of Tables 23 and 24 shows that all of the detectors

except DS show a significant improvement in their explanation of the observed spectra when line emission is included in the power law spectral model.

Of the 24 cases given in Tables 21-24 only 10 of these were acceptable fits to the observed spectra provided by the spectral models. For both the thermal bremsstrahlung plus line emission model and the thermal bremsstrahlung model, detectors CW, DW, DM, and DS were well fit while the fit was unacceptable for detectors CM and CS. The power law plus line emission model gave an acceptable fit only to the data of detectors CM and DS, while the power law spectrum alone did not give an acceptable fit for any detector.

The six different detectors gave six independent determinations of each spectral parameter for each model. These independent values were combined to give the best estimate of each spectral parameter. Since the values did not all have the same accuracy the combination was a weighted average. From statistics (Beers, 1957) the weight, w_i, given to the parameter p_i should be inversely proportional to the square of the expected error in this parameter. This expected error should represent the combination of the statistical and systematic errors. If p_o is the weighted average of the parameters p_i, then

$$p_o = \frac{\Sigma w_i p_i}{\Sigma w_i}$$

For the intensity-independent spectral parameters the errors were primarily statistical so $w_i = N_i$ where N_i is the total number of x-rays used to obtain the observed spectra of the $i^{\underline{th}}$ detector. These N_i were given above in Table 6.

For the continuum intensity (A) the corrections due to deadtime and collimator response (see above) dominated the statistical accuracies. Hence the errors are expected to be proportional to these corrections. Therefore the weight was taken to be the inverse square of this correction factor. The weights assigned to each detector's continuum intensity for the averaging are given in Table 25.

TABLE 25

WEIGHTING FACTORS FOR COMBINING INTENSITIES

Anode Wire Group	Detector C	Detector D
Window	.073	.160
Middle	.264	.359
Side	.272	.364

The combination of the separate values of the line intensities was done in two steps. First the two

lines for each detector were combined into a single line and then these single lines were combined into the final value.

Two lines were used in the spectral models in the hope that some indication of the energy distribution of the excess emission found by the filtered measurements could be obtained in this way. Although the detectors' resolution does not allow independent resolution of two lines, one at 575 ev and the other at 658 ev, it is theoretically possible to deconvolve the response due to the two lines and arrive at the initial energy distribution between these lines. In practice however, as Table 11 indicates, the systematics do not appear well enough understood to allow this unique deconvolution. Hence the use of two lines is here no more enlightening than it was for the filtered measurements. So the same procedure is adopted here as there, i.e. to give the intensity of only a single line at 658 ev. This is done with the caution that this single line intensity is merely a convenient way of expressing the excess emission seen from 0.53 to 0.69 kev and does not represent a unique experimental determination of the energy of this excess emission.

The conversion of the line at 575 ev into another at 658 ev was done so as to preserve the number of photons

observed in the detector. Since I(575) is here the line intensity at the source this intensity must be multiplied by the ratio of the detector efficiencies at 575 ev and 659 ev in order to obtain the correct line intensity at 658 ev which will give the same observed number of photons as the line intensity I(575). This intensity was then added to the intensity already determined to be at 658 ev, I(658), to arrive at the combined intensity I_o . That is:

$$I_o = I(658) + I(575)\exp[-N_H(\sigma_{BG}(.575) - \sigma_{BG}(.658))]\frac{Eff(575)}{Eff(658)}$$

These single line intensities were then combined in a weighted average to give the best estimate of the single line intensity. The expected errors were difficult to estimate for these line intensities. The systematic errors were comparable to the already large statistical errors, but distributed in an almost complementary manner. Comparison of Tables 6 and 25 shows that the statistical errors are expected to be large for the detectors whose systematic errors are small and vice versa. Hence, and in lieu of any better scheme, the weights were all taken to be 1.0, turning the weighted average into the normal arithmetic mean. These weighted averages lead to the combined results given above in

Table 7. The errors given in Table 7 were obtained from the formula:

$$\sigma^2 = \frac{1}{5} \sum_i (p_i - p_o)^2$$

REFERENCES

Beers, Y. 1957, Introduction to the Theory of Error (Palo Alto: Addison-Wesley Publishing Co.)

Bleach, R.D., Boldt, E.A., Holt, S.S., Schwartz,D.A., and Serlemitsos, P.J. 1972, Ap. J., 171, 51.

Brown, R. and Gould, R. 1970, Phys. Rev. D, 1, 2252.

Cox, D.P. unpublished paper submitted to Ap. J.

Doroshenko, V.T. 1971, Sov. Astron.-AJ, 14, 237.

Giacconi, R., Gursky, H., and Van Speybroeck, L.P 1968, Ann. Rev. Astron. Ap., 6, 373.

Gorenstein, P., Gursky, H. and Garmire, G. 1968, Ap. J., 153, 885.

Gorenstein, P., Harris, B., Gursky, H., Giacconi, R., Novick, R., and Van den Bout, P., 1971, Science, 172, 369.

Grader, R.J., Hill, R.W., and Stoering, J.P., 1970, Ap. J. (Letters), 161, 145.

Heiles, C. 1964, Ap. J., 140, 470.

Henke, B.L., Elgin, R.L., Lent, R.E., and Ledingham, R.B. 1967, Norelco Reporter, 14, 112.

Hubble, E.P. 1937, Carnegie Institution Yearbook, 36, 189.

Kundu, M.R. 1969, Ap. J. (Letters), 158, L103.

Lequeux, J. 1969, Structure and Evolution of Galaxies (New York : Gordon and Breach Science Publishers).

Minkowski, R. 1958, Rev. Mod. Phys., 30, 1048.

Minkowski, R. 1968, "Nonthermal Galactic Radio Sources", in Nebulae and Interstellar Matter, VII, Stars and Stellar Systems, ed. Middlehurst and Aller (Chicago : University of Chicago Press).

Oort, J.H. 1946, M.N.R.A.S., 106, 159.

Parker, R.A.R. 1964, Ap. J., 139, 493.

Sedov, L.I. 1959, Similarity and Dimensional Methods in Mechanics (New York : Academic Press).

Shklovskii, I.S. 1968, Supernovae (New York: Interscience Pub.)

Spitzer, L. 1968, Diffuse Matter in Space (New York : Interscience Pub.)

Tucker, W.H. 1971, Science, 172, 372.

Tucker, W.H., and Koren, M. 1971, Ap. J., 168, 283.

van der Laan, H. 1962, M.N.R.A.S., 124, 125.

Zwicky, F. 1940, Rev. Mod. Phys., 12, 66.